

NORTHWESTERN UNIVERSITY

Nanofabrication of Active Nanophotonic Materials and Architectures

A DISSERTATION

SUBMITTED TO THE GRADUATE SCHOOL
IN PARTIAL FULFILLMENT OF THE REQUIREMENTS

for the degree

DOCTOR OF PHILOSOPHY

Field of Materials Science and Engineering

By

Thaddeus Reese

EVANSTON, ILLINOIS

March 2021

© Copyright by Thaddeus Reese 2021

All Rights Reserved

ABSTRACT

Nanofabrication of Active Nanophotonic Materials and Architectures

Thaddeus Reese

Ordered arrays of metallic nanoparticles (NPs) are a promising platform for technological applications and fundamental investigations due to their ability to excite surface lattice resonances (SLRs). SLRs can support extremely high local electric fields that have been used to realize exotic physical phenomena. The open cavity architecture lends itself to the design of active devices that can achieve different responses based on environment and stimuli. However, the desire to expand to new plasmonic materials and multi-functional nanostructures while maintaining mass-production optionality requires the development of precise, yet flexible, parallel nanofabrication techniques.

This thesis describes new methods to fabricate active nanostructures and the characterization of their properties. First, I demonstrate a parallel nanofabrication technique for generating partially filled and multi-metallic NP arrays. By integrating the arrays with gain media, I found that partially filled arrays (as low as 10%) could act as cavities to achieve active lasing action. The flexible process flow was then used to generate bi-metallic arrays that could support bi-modal lasing simultaneously, as well as tri-metallic arrays that could support three SLRs with wavelengths separated by hundreds of nanometers.

In a separate project, I produced titanium nitride NP arrays that could support dipolar or quadrupolar SLRs at near-infrared wavelengths. By characterizing their ultrafast optical properties, I found SLRs had distinct photoinduced transmission from localized surface plasmons. These

trends persisted under extremely high fluence conditions.

Finally, I developed a procedure to fabricate protein hydrogel structures that spontaneously formed nanoscale patterns over large areas from microscale masks. By tuning the concentration of the initial protein solution, I could decrease line features to length scales relevant to photonic applications. This work lays the foundation for ordered plasmonic structures that can dynamically modulate their SLR wavelength by introduction of different ionic species.

The scalable techniques described in this thesis can be easily adapted to new materials of interest, and future developments in the field of active plasmonics. I expect these methods to be useful for applied optical technologies, as well as fundamental studies of nanophotonics.

ACKNOWLEDGEMENTS

First and foremost, I would like to thank my PhD advisor, Prof. Teri Odom for her support and mentorship over the past 5 years. Teri is a better advisor than I ever dreamt of having, and I am eternally grateful for the opportunity to have studied under her guidance. Ever since Teri virtually interviewed me from what looked like a beautiful day in Hawaii, she has advocated for and attempted to improve me as a researcher and an individual. I feel extremely lucky to have learned from a scientist as brilliant, inspiring and creative as Teri, and I will take the lessons and principles I learned in graduate school with me for the rest of my life.

I would also like to thank the members of my PhD committee, Prof. Lincoln Lauhon, Prof. Wei Chen and Prof. Robert Chang, for their constructive feedback throughout grad school. I am very glad that Prof. Lincoln Lauhon pointed me in Teri's direction in the first place – he was also generous with allowing me to use his graduate students and lab space. I would like to thank Prof. Wei Chen for her instruction during the Predictive Science and Engineering Design fellowship program. Prof. Robert Chang has recommended excellent restaurants in the Evanston area since my visit weekend.

This work would not have been possible without the help of my many collaborators. The research in Chapter 2 was assisted by Dr. Dongjoon Rhee, Dr. Ran Li, Jun Guan and used Prof. Rich Schaller's lab. For the work in Chapter 3, I would like to thank Dr. Augustine Urbas for initiating our work with TiN and Dr. Amber Reed for responding to my many requests for more materials. I would also like to thank Dr. Francisco Freire Fernandez, Alexander Sample, Prof. Schaller and Prof. Manuel Ferdinandus for their helpful discussions regarding transient absorption

spectroscopy. Dr. Chelsea Buck, Kristi Singh and Patrick Dennis were fantastic collaborators regarding the protein hydrogel studies in Chapter 4, and I sincerely enjoyed spending time in their lab space at WPAFB over the summers. I appreciate Tucker Kearney for providing insight into the stretchable metalens project and exposing me to predicative science and engineering design principles. I also want to thank Dr. David Tomich for letting me play with the Nanofrazor, although I'm sure that he was more than happy to get out of meetings and hideout in the lab. I appreciate the NUFAB and NUANCE user facilities and staff at Northwestern as well as PNF at UChicago and CNM at ANL. I thank every member of the Odom group for many helpful research discussions in the office and during subgroups. I was fond of the environment our office fostered, and I enjoyed talking to all of you about the latest movies, basketball highlights and current political events.

Of course, I would not have made it through graduate school without my friends outside of lab – I am grateful for all of you. I would like to thank all of my intramural teammates, especially the basketball b-team (Mat-Fly), for all of the great games and practices. James Passarelli and Dr. Megan Hill were great roommates and I appreciate them improving my life instead of making it more difficult. My best friend from undergrad, Waasae Hussain, has always known how to make me laugh like no other, regardless of how bad my day was. To my partner Dr. Jennifer DiStefano, thank you for your endless support throughout grad school but especially this horrible Covid-filled year. I can't imagine making it through this time in my life without you (and more recently, Ithaca the cat).

Finally, I would like to thank my parents Symm and Susan Reese, and my sister Millie. I would not be the human I am today without all of your encouragement and support. I thank my dad for inspiring my endless curiosity, my mom for teaching me how to be an effective communicator and my sister for making sure I'm a good person. I hope I made y'all proud.

LIST OF ABBREVIATIONS

AFM	Atomic force microscopy
Ag	Silver
Al	Aluminum
Al ₂ O ₃	Aluminum oxide (alumina). Also sapphire.
AlN	Aluminum nitride
Ar	Argon (gas)
Au	Gold
BCl ₃	Boron chloride (gas)
C540	Coumarin-540 dye
Cl	Chlorine (gas)
CMOS	Complementary metal-oxide-semiconductor
Cr	Chromium
Cu	Copper
DCM	4-(Dicyanomethylene)-2-methyl-6-(4-dimethylaminostyryl)-4 <i>H</i> -pyran
DL	Dipolar SLR or dipolar LP
DMSO	Dimethyl sulfoxide
EBL	Electron beam lithography
EDS	Energy Dispersive X-Ray Spectroscopy
FDTD	Finite-difference time-domain
FIB	Focused ion beam lithography

ICP-RIE	Inductively coupled plasma reactive ion etching
IR792	IR-792 percholate dye
LP	Lattice plasmon (alternate name for SLR)
LSP	Localized surface plasmon resonance (alternative name for LSPR)
Na	Sodium
NIR	Near-infrared
NP	Nanoparticle
NVJP-1	<i>Nereis virens</i> jaw protein
OAc	Acetate ion
PDMS	Polydimethylsiloxane
PEEL	Patterning, evaporation, etching, liftoff
PMMA	Polymethyl methacrylate
PPA	Polyphthalamide
PR	Photoresist
QL	Quadrupole SLR or quadrupole LP
RA	Rayleigh Anomaly (also known as Woods Anomaly)
RIE	Reactive ion etching
S12	Suckerin-12 protein isoform
SANE	Solvent assisted nanoembossing
SEM	Scanning electron microscopy
Si	Silicon
SiO ₂	Silicon dioxide (silica)
SLR	Surface lattice resonance (alternative name for LP)

t-SPL	Thermal scanning probe lithography
TA	Transient Absorption Spectroscopy
TiN	Titanium Nitride
UV	Ultraviolet
Zn	Zinc
ZrN	Zirconium nitride

TABLE OF CONTENTS

ABSTRACT.....	3
ACKNOWLEDGEMENTS.....	5
LIST OF ABBREVIATIONS.....	7
TABLE OF CONTENTS.....	10
LIST OF FIGURES	14
Chapter 1 Introduction to Nanofabrication for Active Plasmonics	20
1.1. Plasmonic Nanostructures.....	21
1.1.1. Introduction to the Field of Plasmonics	21
1.1.2. Ordered Plasmonic Nanostructures.....	21
1.2. Fabrication of Plasmonic Nanostructures	23
1.2.1. Diffraction Limit of Light.....	23
1.2.2. Forming Patterns by Direct-Write Techniques	23
1.2.3. Scalable Pattern Formation	24
1.2.4. Transferring Patterns into Materials	26
1.3. Active and Dynamic Optical Devices	28
1.3.1. Introduction to Stimulated Plasmonic Systems	28
1.3.2. Light-responsive Plasmonics	29
1.3.3. Plasmonic Structures as Nanolasers.....	29
1.3.4. Mechanical Deformation of Plasmonic Lattices.....	31
1.3.5. Environment-Sensitive Materials.....	32
1.4. Outline of Thesis.....	33
Chapter 2 Multi-Color Lattice Plasmons from Multi-Metal Nanoparticle Arrays	35
2.1. Introduction.....	36
2.2. Process Flow for Fabricating Partially Filled or Multi-metal NP Arrays.....	37
2.3. Controlling Photoresist Coverage and Nanoparticle Array Filling.....	38
2.3.1. Quasi-Random Photoresist Wrinkles	38
2.3.2. Partially Filled NP Arrays.....	40
2.4. Optical Properties of Partially Filled Al NP Arrays	41
2.4.1. Static Transmission Measurements.....	41

2.4.2. Lasing Performance of Partially Filled NP Arrays	44
2.5. Bi-Metallic NP Arrays	46
2.5.1. Bi-metallic NP Array Fabrication	46
2.5.2. Optical Properties of Bi-metallic NP Arrays	48
2.5.3. Aluminum and Silver Bi-metallic NP Arrays	49
2.6. Tri-Metallic NP Arrays	50
2.6.1. Fabrication of Tri-metallic NP Arrays	50
2.6.2. Optical Properties of Tri-metallic NP Arrays	52
2.6.3. Tri-metallic NP Arrays with 3 SLRs in the Visible Regime	54
2.7. Conclusions	55
2.8. Methods	56
2.8.1. Fabrication of NP Arrays	56
2.8.2. Finite-Difference Time-Domain Simulations	57
2.8.3. Transmission Measurements	57
2.8.4. Lasing Measurements	57
Chapter 3 Ultrafast Spectroscopy of Plasmonic Titanium Nitride Nanoparticle Lattices ..	58
3.1. Introduction	59
3.2. Fabrication of High-Quality TiN NP Arrays	60
3.3. Optical Properties of Index-matched and Index-mismatched TiN NP Arrays	62
3.3.1. Steady-State Transmission Measurements	62
3.3.2. Nearfield Finite-Difference Time-Domain Simulations	64
3.4. Transient Absorption Spectroscopy of TiN LSPs and SLRs	65
3.4.1. Index-Matched and Index-Mismatched TiN NPs at Ultrafast Timescales	65
3.4.2. Transient Absorption of TiN Thin Films	68
3.4.3. Transient Response at High Pump Fluences	69
3.5. Probing Effect of Environment and Pump Energy on Ultrafast Properties of TiN NP Arrays	70
3.5.1. Tuning Environment to Determine Solvation	70
3.5.2. Sweeping Pump Energy	73
3.6. Introduction to Multi-layer Plasmonics	74
3.7. Fabrication of Metal-Insulator NPs from High-Quality TiN/AlN Thin Films	75
3.8. Optical Properties of TiN/AlN NP Arrays	77
3.8.1. Steady-State Transmission Measurements	77

	12
3.8.2. Transient Absorption of TiN/AlN NP Arrays.....	78
3.9. Future Works: Transition-Metal Nitrides for Visible Regime.....	80
3.9.1. Introduction to Zirconium Nitride	80
3.9.2. Optical Simulations of ZrN NP Arrays.....	80
3.9.3. ZrN NP Array Fabrication	82
3.10. Conclusions.....	83
3.11. Methods.....	83
3.11.1. TiN NP Array Fabrication	83
3.11.2. TiN Film Growth	84
3.11.3. Steady-State Optical Measurement.....	84
3.11.4. Finite-Difference Time-Domain Simulations.....	84
3.11.5. Transient Absorption (TA) Measurements	85
Chapter 4 Scalable Fabrication of Ion-Tunable Protein Hydrogel Nanostructures	86
4.1. Introduction.....	87
4.2. Fabricating Nanoscale Protein Hydrogel Architectures	88
4.2.1. Process Flow for Generating Nanoscale Features from Microscale Masks	88
4.3. Contracted Suckerin-12 Hydrogel Microstructures	90
4.3.1. 1D and 2D Contraction	90
4.3.2. Effect of S12 Solution Concentration on Microscale Features.....	92
4.4. Nanoscale Suckerin-12 Architectures from Microscale Masks.....	93
4.5. Anisotropic S12 Replication of Mask Through Surface Modification.....	95
4.6. Summary of S12 Contraction Experiments	97
4.7. Expanding Process Flow to NVJP-1.....	98
4.8. Conclusions.....	99
4.9. Methods.....	100
4.9.1. PDMS Mask Fabrication.....	100
4.9.2. Expression of NVJP-1.....	100
4.9.3. NVJP-1 Hydrogel Formation	101
4.9.4. Expression and Purification of Recombinant Suckerin-12 in Escherichia coli	101
of NVJP-1	101
4.9.5. Suckerin-12 Hydrogel Formation	102
Chapter 5 Summary & Outlook	104
Appendix A Optimization and Fabrication of Stretchable Metalenses	108

	13
A.1. Introduction to Metalenses.....	109
A.2. Predictive Results of Stretchable Metalenses	110
A.1. Fabrication of Stretchable Metalenses	117
Appendix B Nanofrazor for Multi-Material Overlay.....	122
B.1. Aligned Multi-metallic Metasurfaces.....	123
B.2. Fabrication of Aligned Multi-metallic Metasurfaces	124
REFERENCES	129
CURRICULUM VITAE.....	141

LIST OF FIGURES

- Figure 1.1. LSP and SLRs** (a) Transmission spectra of a single plasmonic NP which supports a localized surface plasmon. (b) Transmission spectra of a periodic array of plasmonic NPs which supports a surface lattice resonance. Figure reproduced with permission from reference³⁷ (<https://pubs.acs.org/doi/10.1021/acs.chemrev.8b00243>) 22
- Figure 1.2. Serial nanopatterning techniques** (a) Scheme depicting process of e-beam lithography to generate resist masks from positive tone or negative tone films. (b) Scheme depicting the operating principle of thermal scanning probe lithography. 24
- Figure 1.3. Solvent-assisted Nanoembossing** (a) Patterned PR posts over wafer scale area. (b) Process flow for reproducing arrays of PR posts from a single master. Figure adapted with permission from ref.⁵⁹ Copyright (2011) American Chemical Society 25
- Figure 1.4. Transferring mask patterns into desired material.** Schemes depicting the process of transferring a patterned mask through (left) an isotropic chemical wet etch, (middle) directional reactive ion etch or (right) a highly anisotropic dry etch. 26
- Figure 1.5. Induced transparency in plasmonic systems.** Plasmonic device that could actively modulate transmission through intense laser pump. Figure adapted with permission from Springer-Nature, Nature Photonics, reference⁷⁵ Copyright 2009, Nature Publishing Group. 28
- Figure 1.6. SLR-based Nanolasers** (a) Threshold lasing behavior of SLR with gain media. (b) Low angular divergence of SLR nanolaser. (c) Tunable lasing wavelength by changing local refractive index. Panels (a) and (b) adapted with permission from Springer-Nature, Nature Nanotechnology, reference⁴⁷. Copyright 2013, Nature Publishing group. Panel (c) adapted with permission from reference⁴⁸. Copyright 2015, Ankun Yang, et. al. 31
- Figure 1.7. Stretchable NP arrays** (a) Tunable dipolar and quadrupolar SLRs based on lattice strain of a Al NP array embedded in PDMS. (b) Tunable lasing wavelength by a strained Al NP array embedded in PDMS with a liquid gain solution. Panel (a) adapted with permission from ref.¹⁰⁴ Panel (b) adapted with permission from ref.⁸⁵ Copyright (2018) American Chemical Society..... 31
- Figure 2.1. Scalable process flow for partially filled and bimetallic NP arrays with controllable filling factor.** (a) Molding PDMS SANE masks from quasi-random Cr microwrinkles. (b) Partially filled NP arrays or bimetallic NP arrays with RIE-tunable filling factor 38
- Figure 2.2. Scalability and fidelity of the pattern transfer process for quasi-random stamp fabrication.** Chromium wrinkles under (a) optical and (b) AFM topography images. PDMS replica under (c) optical and (d) AFM topography images. Insets in panels b and d shows 2D FFT of the AFM images. 39

- Figure 2.3. Relationship between RIE time and photoresist filling factor.** (a) AFM images showing PR wrinkles on Si wafers after given RIE time. (b) Graph showing the linear function of decreased filling factor with increased RIE time ($R^2 = 0.9932$)..... 40
- Figure 2.4. Partially filled NP arrays.** AFM images showing quasi-random patches of Al NPs with filling factors ranging from 99%-10% by changing RIE time before Al wet etch. Arrays have $a = 400$ nm and are 60 nm thick with an approximate diameter of 90 nm..... 40
- Figure 2.5. Transmission spectra of partially filled NP arrays.** Steady-state spectra taken for the partially filled NP arrays shown in figure 2.4. Samples were index-matched with fluid $n = 1.45$. Arrays have $a = 400$ nm and are 60 nm thick with an approximate diameter of 90 nm..... 41
- Figure 2.6. Transmission spectra of fully filled NP arrays.** Steady-state spectra taken for the NP arrays shown in figure 2.5. The color of each trace corresponds to the sample used before etching..... 42
- Figure 2.7. FDTD calculated transmission spectra of partially filled NP arrays.** Simulations used $30 \times 30 \mu\text{m}^2$ regions with perfectly matched layers in $\pm x$, $\pm y$ and $\pm z$ directions. Quasi-period was introduced by binarizing an AFM image of the micro wrinkle mask used in fabrication with a threshold set to achieve the given filling factor. The binarized Al NPs had $a = 400$ nm, thickness of 60 nm and diameter of 90 nm..... 43
- Figure 2.8. Dispersion diagrams of partially filled NP arrays.** Energy-momentum dispersion diagrams for partially filled Al NP arrays with $f_{\text{NP}} \approx$ (a) 80%, (b) 60%, (c) 20% and (d) 10%. White light probe was set to TE polarization with respect to the samples. 44
- Figure 2.9. Lasing action from partially filled Al NP arrays.** (a) Scheme showing a partially filled NP array with gain material being pumped by a femtosecond pulse laser. (b) Lasing spectra for partially filled NP arrays and (c) their corresponding light in-light out plots. 50 mM C540 dye was dissolved in DMSO for all experiments and samples were pumped by a $\lambda = 400$ nm laser. 45
- Figure 2.10. Linear relation of lasing threshold to NP filling factor** 46
- Figure 2.11. Au hole masks fabricated by PEEL floated onto PR microwrinkles.** Au hole masks have (a) $a = 400$ nm floated onto PR wrinkles and (b) $a = 500$ nm floated onto PR wrinkle-protected Al NPs 47
- Figure 2.12. Imaged Al and Au bi-metallic NP arrays.** (a) Scheme depicting Al and Au bi-metallic NP array with $a_{\text{Al}} = 400$ nm and $a_{\text{Au}} = 500$ nm. (b) SEM and EDS images taken of an Al-Au bi-metallic NP array..... 47
- Figure 2.13. Optical properties of Al and Au bi-metallic NP arrays.** (a) Transmission spectra of a bimetallic NP array. Lasing spectra for a bi-metallic array integrated with (b) 50 mM C540 and pumped at 1.21 mJ/cm^2 , (c) 10 mM LD700 and pumped at 1.61 mJ/cm^2 and (d) mixture of 40 mM C540 and 2.5 mM LD700 and pumped at 2.13 mJ/cm^2 . Bi-metallic array consisted of Al NPs with $a = 400$ nm and thickness of 60 nm and Au NPs with $a = 500$ nm and thickness of 60 nm. All dyes were dissolved in DMSO. Samples were irradiated with a femtosecond laser at $\lambda = 400$ nm for lasing experiments..... 48

Figure 2.14. Light-light curves for bi-metallic NP arrays. Lasing intensity as a function of pump fluence at the (a) Al SLR with C540 dye and (b) Au SLR with LD700. $a = 400$ nm floated onto PR wrinkles and (b) $a = 500$ nm floated onto PR wrinkle-protected Al NPs..... 49

Figure 2.15. Al-Ag bi-metallic NP arrays. (a) SEM image of an Al-Ag bi-metallic NP array and EDS signal of the (b) Al and (c) Ag NPs..... 50

Figure 2.16. Tri-metallic NP array fabrication. (a) Scheme depicting the process flow for producing tri-metallic NP arrays after starting with bi-metallic NP arrays. (b) AFM image of Al-Ag-Au NPs array with $a_{Al} = 300$ nm, $a_{Ag} = 450$ nm and $a_{Au} = 600$ nm..... 51

Figure 2.17. Normal incidence transmission spectra of tri-metallic NP arrays and their constituent NP arrays. (a) Fully filled NP arrays for Al ($a = 300$ nm), Ag ($a = 450$ nm) and Au ($a = 600$ nm). (b) Bi-metallic array consisting of approximately half Al ($a = 300$ nm) and half Au ($a = 600$ nm). (c) Tri-metallic array after integrating approximately 33% Ag ($a = 450$ nm)..... 53

Figure 2.18. Optical properties of tri-metallic NP arrays. (a) $E-k$ dispersion diagram for a tri-metallic NP array. Lasing spectra of the tri-metallic array when integrated with (b) 5 mM DCM dissolved in DMSO and pumped at $\lambda = 400$ nm and (c) 10 mM IR792 dissolved in DMSO and pumped at $\lambda = 800$ nm. 54

Figure 2.19. Visible-regime tri-metallic NP arrays. (a) SEM and EDS images and (b) transmission spectra of a trimetallic NP array with $a_{Al} = 300$ nm, $a_{Ag} = 400$ nm and $a_{Au} = 500$ nm. 55

Figure 3.1. Single-crystalline TiN NP lattices by top-down patterning. (a) Scheme of the process flow to generate TiN NP arrays. (b) SEM image of fabricated TiN NP array. 61

Figure 3.2. NIR plasmonic resonances of TiN NP Arrays. (a) Experimental and simulated transmission spectra of TiN NP arrays in index (a) mismatched and (b) matched environments. Experimental spectra are vertically offset by 0.75. For index mismatched simulations and experiments the substrate (sapphire) had $n = 1.75$ and superstrate (air) had $n = 1.0$ 62

Figure 3.3. Evolution of QL with increased TiN film height. (a) Experimental and (b) simulated transmission spectra for index matched TiN arrays. All samples were fabricated from the same photoresist thickness and PDMS SANE mask. Simulations used $a = 600$ nm and $r = 100$ nm. 62

Figure 3.4. Fabrication procedure can generate sharp TiN SLRs in NIR. (a) SEM image showing TiN NP array with $a = 720$ nm and $t = 90$ nm. (b) Transmission spectra measured by UV-vis spectrophotometer. (c) Transmission spectra calculated by FDTD for a TiN NP array with $t = 90$ nm, $a = 720$ nm and $r = 75$ nm. 63

Figure 3.5. Fabrication procedure can generate sharp TiN SLRs in NIR. Simulated nearfield and charge density for (a) $\lambda_{DL} = 1202$ nm with $t = 50$ nm and (b) $\lambda_{QL} = 1052$ nm and (c) $\lambda_{DL} = 1180$ nm with $t = 100$ nm. Dimensions for all near-field calculations are $a_0 = 600$ nm, $r = 100$ nm. For index mismatched simulations and experiments the substrate (sapphire) had $n = 1.75$ and superstrate (air) had $n = 1.0$ 65

- Figure 3.6. Plasmon mode alters ultrafast absorption line shape.** TA spectral maps (a, c) and time slices of TA data (b, d) for a TiN NP arrays with (a-b) $t = 50$ nm in air and (c-d) $t = 100$ nm in index oil. Samples were pumped with 800 nm light at 1.5 mJ/cm^2 fluence. 66
- Figure 3.7. TA of index-matched TiN NP array with $t = 50$ nm.** TA spectral map and time slices of TA data for a TiN NP arrays with $t = 50$ nm in index oil. Sample was pumped with 800 nm light at 1.5 mJ/cm^2 fluence. 67
- Figure 3.8. Transmission Absorption Spectra of TiN films.** TiN thin film with thickness of approximately 15 nm in (a) air and (b) index fluid $n = 1.8$. (c) TA spectra of only index oil on sapphire. 68
- Figure 3.9. TiN NP arrays under extreme pump irradiation.** (a) TA spectra taken at 542 fs for irradiance with high pump powers for index-matched $t = 100$ nm TiN NP arrays. (b) TA spectral maps for pump at 21 mJ/cm^2 . (c) TA spectra taken at 250 fs for irradiance with high pump powers for $t = 50$ nm TiN NP arrays in air. (d) TA spectral maps for pump at 53 mJ/cm^2 69
- Figure 3.10. TiN NP arrays in low-index solvents.** TA spectra taken TiN NP arrays in water ($n = 1.333$), IPA ($n = 1.376$), acetone ($n = 1.395$) and DMSO ($n = 1.479$). Samples were pumped at 2.8 mJ/cm^2 with $\lambda = 800$ nm. 71
- Figure 3.11. TiN NP arrays in gas, solid and liquid.** (a) Transmission spectra comparing a TiN NP array in air, 300 nm of Al_2O_3 and $n = 1.8$ index oil. Accompanying TA spectra for the TiN NP array in (b) air, (c) 300 nm of Al_2O_3 and (d) $n = 1.8$ index oil. 72
- Figure 3.12. TiN NP array pumped by different energies.** TA spectra for a TiN NP array with $a = 600$ nm, $t = 90$ nm pumped at $\lambda = 325$ nm, 400 nm, 800 nm, 1050 nm, 1200 nm and 1500 nm. All spectra have had background subtracted. 74
- Figure 3.13. Process flow for fabricating TiN/AlN NP arrays.** Scheme depicting the use of a Cu nanodiscs to mask the TiN/AlN films during a two-step ICP-RIE etch. 76
- Figure 3.14. Fabrication of TiN/AlN NP arrays.** (a) SEM image of Cu NPs deposited through hole mask on TiN/AlN films. (b) AFM and (c) SEM image of sample after ICP-RIE but before Cu removal. (d) AFM image of sample after Cu removal. 77
- Figure 3.15. Transmission spectra of TiN/AlN NP array.** 78
- Figure 3.16. Transient absorption spectra comparing TiN and TiN/AlN NP arrays.** (a) TA spectral surface (b) delay spectra for a TiN NP array with $a = 600$ nm. (a) TA spectral surface (b) delay spectra for a TiN/AlN NP array with $a = 600$ nm. Both samples pumped by $\lambda = 800$ nm with air superstrate. 79
- Figure 3.17. Measured Optical Properties of Transition-metal Nitrides.** (a) Real and Imaginary permittivity values for Zirconium nitride. Stars indicate transition from metallic to dielectric. 80

Figure 3.18. FDTD simulated radii sweep of ZrN NP arrays. Transmission spectra for index match ZrN NP arrays with period (a) 450 nm and (b) 500 nm. Radius was swept from 20-50 nm. All NPs used $t = 50$ nm..... 81

Figure 3.19. Fabricating ZrN nanostructures. (a) Process flow for transferring NP array into ZrN thin films. (b) SEM image of fabricated ZrN array 82

Figure 4.1. Scalable process flow for fabricating protein polymer nanostructures. S12 nanostructures can be formed from microscale PDMS molds by taking advantage of S12 contraction in buffer solution..... 89

Figure 4.2. Processing for protein hydrogel nanostructures. Photographs depicting the process of contracting large areas of nanopatterned hydrogels 90

Figure 4.3. SEM Images of Si masters and their resulting contracted S12 microfeatures. SEM images of Si masters with (a) $a' = 50$ μm lines, (c) $a' = 10$ μm lines and (e) $a' = 25$ μm squares. AFM images of contracted S12 microfeatures with (b) $a'' = 26$ μm , (b) $a'' = 4.5$ μm and (b) $a'' = 13$ μm . All samples used 6 wt% S12 solution and contracted in 100 mM NaOAc buffer. 91

Figure 4.4. Effect of S12 solution concentration on contracted microfeatures. (a) SEM images of Si masters with $a' = 25$ μm squares. AFM images and height line traces of contracted S12 microfeatures from (b) 6 wt% and (c) 3 wt%. All samples were contracted in 100 mM NaOAc buffer..... 93

Figure 4.5. S12 nanofeatures from microscale masks. SEM images of Si masters used for PDMS masks with $a' =$ (a) 2 μm and (d) 1 μm lines. AFM images and height line traces of contracted S12 nanofeatures from $a' = 2$ μm masks from (b) 6 wt% and (c) 3 wt% solution and $a' = 1$ μm masks from (e) 6 wt% and (f) 3 wt% solution. All samples were contracted in 100 mM NaOAc buffer..... 94

Figure 4.6. Anisotropic contraction of S12 nanofeatures through PDMS surface functionalization. (a) Process flow depicting anisotropic contraction by treating PDMS mask with O_2 plasma. (b) SEM of Si master with $a' = 1$ μm masks that was used to mold PDMS mask. (c) S12 nanostructure (6 wt% solution) after several hours immersed in buffer solution while in negatively charged PDMS mask. (d) Bar graph showing contraction percentage of S12 nanostructure period, line diameter and line height relative to initial PDMS mask. Samples was contracted in 100 mM NaOAc buffer. 95

Figure 4.7. Contraction percentage of grating width, trough gap, periodicity and height for S12 hydrogels using different masks and procedures. 97

Figure 4.8. NVJP-1 nanofeatures with buffer progression (a) AFM image of PDMS mask used in NVJP-1 molding and contraction with $a' = 2$ μm . AFM images of NVJP-1 nanofeatures after in contraction in (b) NaOAc, then (c) $\text{Zn}(\text{OAc})_2$ and finally (d) NaCl 200 mM buffer solutions. Hydrogels were imaged in their respective buffer solution..... 98

Figure A.1. Schematic showing how the fields for a single NP are saved assuming an infinite, perfectly periodic array and are superimposed to determine the response in the GA. 110

- Figure A.2.** (Top) x-z windows calculated by the superposition of fields from each lattice unit taken assuming an infinite array. (Bottom) x-z windows calculated by simulating the entire lattice optimized by GA in FDTD 113
- Figure A.3.** Two of the compatible responses from the DoE. Red boxes indicate the $1 \mu\text{m}^2$ window that is calculated and optimized by the GA. Yellow arrows indicate the variables that were varied in the DoE. Lattices were optimized for $\lambda = 475 \text{ nm}$, with Al NP diameter of 100 nm and thickness of 50 nm. 40 x 40 lattice units. 114
- Figure A.4.** 3D scatter plot of the (left) compatible responses and (right) incompatible results of the 200 trial DoE..... 116
- Figure A.5.** Process flow for fabricating Al NPs and embedding them in PDMS..... 118
- Figure A.6.** Post patterns of negative tone e beam resists. Over dosed PMMA developed in (left) MIBK or (right) developed in acetone. (Center) Microchem ma-N 2401 developed in microchem ma-D 331. 119
- Figure A.7.** (Top left) SEM showing partial transfer of Al posts on Si after backfilling with PDMS and stripping. (Right) Optical microscope image of cracked Al film on PDMS after stripping. (Bottom left) AFM of a successful pattern transfer off of the Si substrate and into PDMS..... 120
- Figure B.1. Al + Au Metalens.** (a) Au and Al lattice optimized by OLEA. (b) FDTD simulated electric far field intensities at $\lambda = 475 \text{ nm}$ and (c) 650 nm . Lens parameters: $a = 300 \text{ nm}$, $t = 50 \text{ nm}$, $r_{\text{Au}} = r_{\text{Al}} = 80 \text{ nm}$ 123
- Figure B.2. Multi-metallic Metasurface Process Flow.** Alignment marker-free fabrication procedure for patterning bi-metal ultrathin optical devices by Nanofrazor (t-SPL)..... 124
- Figure B.3. Nanofrazor Overlay Patterning on Au Superlattice Arrays.** (a) Scan by Nanofrazor read tip of Au structure coated in Al and PPA resist. (b) Hole array pattern overlay by Nanofrazor. (c) AFM image of grid of hole arrays patterned by Nanofrazor..... 125
- Figure B.4. PPA Etch.** (a) Plot of the thickness of PPA etched versus O_2 RIE time. 126
- Figure B.5. Fabricating Al-Au Nanostructures.** SEM images of (a) a PPA hole array patch patterned by Nanofrazor on a Au NP superlattice substrate coated in Al and PPA. The patch consists of 50×50 holes with $d = 80 \text{ nm}$ and $a = 300 \text{ nm}$. (b) The same sample after 15 nm of Cu deposition and liftoff in acetone. (c) The same sample after ICP-RIE etch of Al and Cu removal. 127
- Figure B.6. Nanofrazor Metalens Overlay.** (a) Nanofrazor scan of Au metalens coated in Al and PPA resist. (b) Nanofrazor scan after writing hole pattern that will become Al NPs in final metalens. 128

Chapter 1

Introduction to Nanofabrication for Active Plasmonics

1.1. Plasmonic Nanostructures

1.1.1. Introduction to the Field of Plasmonics

Plasmonic resonances have a range of exciting properties, primarily because their strong light interaction can increase optical scattering and absorption and generate intense local electric fields. These phenomena have led to fundamental advances in many areas of research, including nanobiology, physical chemistry and materials science. In addition, the field of plasmonics promises enhanced performance in applications ranging from photovoltaics,¹⁻⁶ chemical sensors,^{7, 8} medical diagnostics⁹⁻¹² and miniaturized optical components.¹³⁻¹⁸

Localized surface plasmons (LSP), which are collective electron oscillations at the surface of nanoscale metallic structures, are excited when an incident electromagnetic wave matches their resonant frequency.¹⁹⁻²¹ To be considered an efficient plasmonic material, the real part of the dielectric function must be negative and large while the imaginary component is small but positive.²²⁻²⁵ The resonant wavelength of a plasmonic system depends on multiple properties, such as material, size, shape and local dielectric environment.²⁶ By tuning these parameters, LSPs can realize an incredible number of responses in wavelength regimes from the ultraviolet to the infrared. Usually, LSPs are dipolar in nature (one positively charged and one negatively charged region), but depending on the geometry of the nanoparticle they may support higher-order modes.²⁷⁻³⁰

1.1.2. Ordered Plasmonic Nanostructures

Nanoparticles that support LSPs have become commonplace in research labs across the world due to robust and varied synthesis procedures³¹⁻³⁵ and commercial availability. However, radiative losses cause LSPs to be relatively broad (**Figure 1.1a**), which limits their ability to target specific wavelengths or be used in situations that require high quality factors ($Q = \Delta\lambda/\lambda$). One solution to

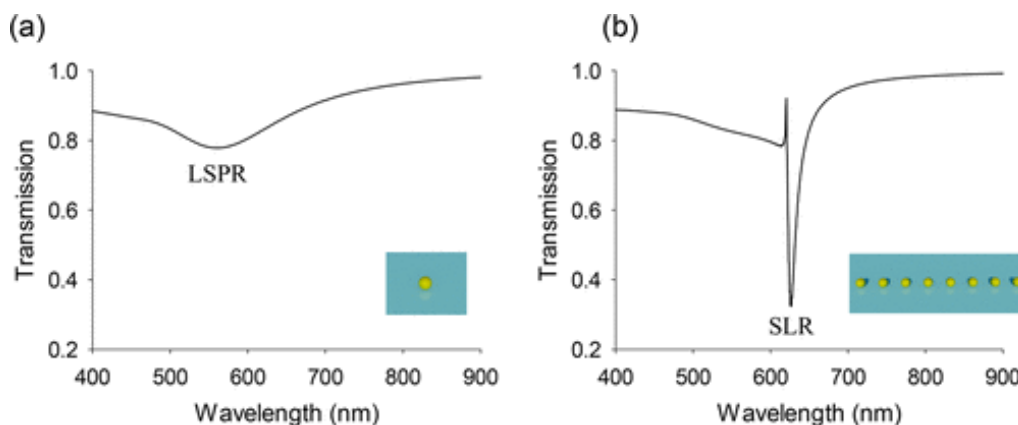


Figure 1.1. LSPs and SLRs (a) Transmission spectra of a single plasmonic NP which supports a localized surface plasmon. (b) Transmission spectra of a periodic array of plasmonic NPs which supports a surface lattice resonance. Figure reproduced with permission from reference³⁷ (<https://pubs.acs.org/doi/10.1021/acs.chemrev.8b00243>)

overcome these high losses is by placing plasmonic units (such as nanoparticles or nanoposts) into a regularly spaced array inside a uniform index environment (**Figure 1.1b**).³⁶⁻⁴¹ In this manner, the LSPs scatter light in-plane, and collectively couple to the Bragg diffraction orders to mitigate losses. These hybrid modes are known as lattice plasmons or surface lattice resonances (SLR). SLRs are dispersive modes, but at momentum $k = 0$, a band edge exists which indicates a group velocity $dw/dk_{\parallel} = 0$. When the group velocity is 0, the mode is non-propagating, so a standing wave pattern is formed.

The resonant wavelength of SLRs can be precisely tuned through the refractive index environment, lattice geometry and LSP of the constituent NPs. By optimizing these parameters, SLRs can achieve significantly narrower resonances and higher electric fields than LSPs.³⁶⁻⁴¹ These sharp resonances enable SLRs to be used for ultrasensitive bio-detection^{42, 43} and efficient catalysis.⁴⁴ SLRs have also attracted attention for their ability to access exotic properties such as bose-einstein condensation,⁴⁵ strong-coupling⁴⁶ and lasing action⁴⁷⁻⁴⁹ when integrated with gain materials. However, due to the precision needed to produce uniform NP and array dimensions, the

process of achieving high-quality SLRs requires sophisticated nanofabrication techniques.

1.2. Fabrication of Plasmonic Nanostructures

1.2.1. Diffraction Limit of Light

Nanofabrication refers to the process of generating structures with at least one dimension confined to approximately 1-100 nm. These length scales have become critical for a variety of fundamental studies and technological applications in fields such as photonics, microelectronics and nanobiology. Perhaps most prominently, the Si-based electronics industry has continued to push minimum feature sizes well below hundreds of nanometers according to Moore's Law. However, as the critical dimensions have become approached the wavelength of light, researchers have had to develop new techniques to beat the diffraction limit of light. The diffraction limit of light is generally given as:

$$d = \frac{\lambda}{2n\sin(\theta)} \quad (1.1)$$

Where d is the minimum resolvable distance, λ is the wavelength of light used, n is the index of refraction of the material the light travels through and θ is the half-angle of the light spot.

Assuming visible light ($\lambda = 400-700$ nm) propagating through air ($n = 1.0$), the diffraction limit can be thought of as approximately 200 nm. This value is larger than what is usually required to fabricate nanostructures with plasmonic resonances in the visible and NIR regimes.

1.2.2. Forming Patterns by Direct-Write Techniques

One of the most effective ways to produce patterns below the diffraction limit is by using beams composed of electrons instead of light, which can form features on the order of several nanometers.⁵⁰⁻⁵² **Figure 1.2a** depicts the operation of electron-beam lithography (EBL) which

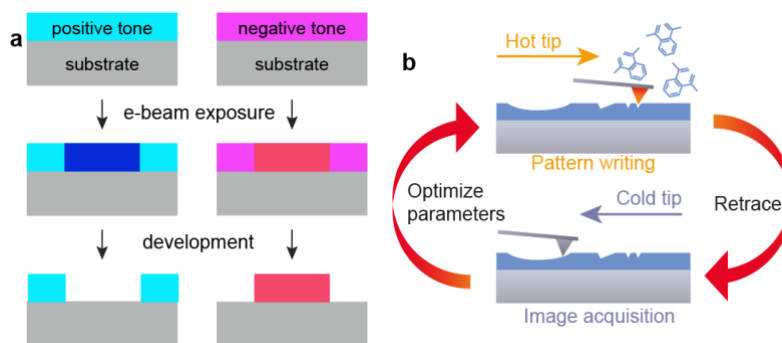


Figure 1.2. Serial nanopatterning techniques (a) Scheme depicting process of e-beam lithography to generate resist masks from positive tone or negative tone films. (b) Scheme depicting the operating principle of thermal scanning probe lithography. Panel b image courtesy: Heidelberg Instruments Nano.

scans a focused beam of electrons in a pre-determined pattern onto an electron-sensitive resist film (positive tone if the electrons increase the solubility or negative tone if the electrons decrease the solubility of the exposed area).^{39, 50-52} After developing the sample in a solvent, the exposed area (or surrounding area for negative tone resist) will dissolve, and the remaining resist can be used as a mask to transfer the pattern into a separate material.

Another serial writing method, known as thermal scanning probe lithography (t-SPL) has emerged as a nanopatterning technique in recent years;⁵³⁻⁵⁵ this method forms resist structures by ablating a thermally active polymer (**Figure 1.2b**). Because t-SPL is usually integrated into a scanning probe imaging system, t-SPL can achieve pattern overlay or stitching errors on the order of several nanometers while EBL registration errors are at least on the order of tens of nanometers. However, all direct write techniques suffer from long patterning times, which limit the area over which a structure can be written in a reasonable amount of time or cost.

1.2.3. Scalable Pattern Formation

Scalable manufacturing refers to the practice of using processing techniques that can produce

large patterned areas simultaneously, or in parallel. Scalable nanofabrication methods are highly desired because they are often significantly less time and cost intensive than direct writing. Photolithography tools remain the most common scalable process for achieving nanoscale features in the semiconductor industry, but these tools have become increasingly complex and need immersion liquids^{56, 57} and multiple patterning steps⁵⁸ to create a single masking layer. Hence, there is significant interest in developing high-throughput benchtop methods that can reliably

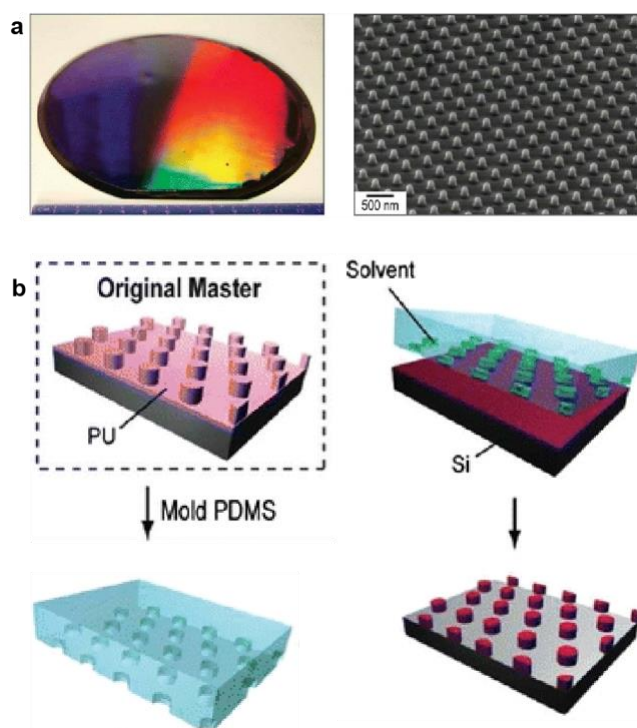


Figure 1.3. Solvent-assisted nanoembossing (SANE) (a) Patterned PR posts over wafer scale area. (b) Process flow for reproducing arrays of PR posts from a single master. Figure adapted with permission from ref.⁵⁹ Copyright (2011) American Chemical Society

fabricate features below the diffraction limit.

Nanoimprint lithography has become a prominent strategy for producing ordered photonic nanostructures.⁶⁰⁻⁶⁴ Generally, nanoimprint lithography involves a patterned mask or mold that is pressed into a resist film to form nanoscale features. Depending on the material used for the mask,

the minimum feature sizes can be on the order of tens of nanometers. A single mask can be reused numerous times so the process is highly reproducible. Therefore, only one direct write process is needed to fabricate the original master. This thesis will make use of a variation on nanoimprint lithography, known as solvent-assisted nanoembossing (SANE).⁵⁹ SANE uses elastomer masks (usually PDMS) molded from a structured master (usually Si) to form polymer photoresist (PR) patterns (**Figure 1.3**). In order to manipulate the resist, the PDMS mask is soaked in a solvent that can dissolve the PR, placed onto a substrate coated in PR, and allowed to dry for approximately 30 min. These PDMS masks can be used many times (dozens to hundreds), and the dimensions of the features can be tuned by using solvents with different swelling ratios in PDMS.

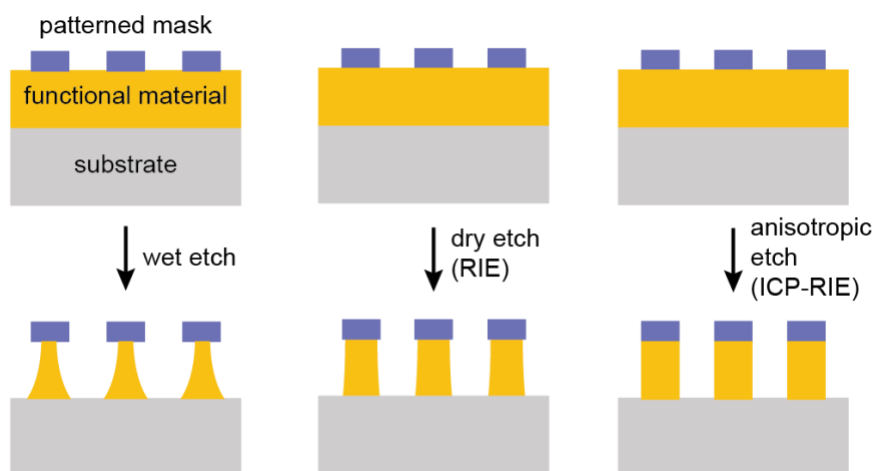


Figure 1.4. Transferring mask patterns into desired material. Schemes depicting the process of transferring a patterned mask through **(left)** an isotropic chemical wet etch, **(middle)** directional reactive ion etch or **(right)** a highly anisotropic dry etch.

1.2.4. Transferring Patterns into Materials

After forming a masking layer, either through a direct write process like EBL or a parallel process like SANE, the PR is usually transferred into a more functional material. There are two primary ways that this is achieved: (1) lift-off or (2) etching.

Lift-off refers to the process of depositing a material (such as a metal) through e-beam or thermal evaporation, then “lifting-off” the initial masking layer (usually PR). Because the PR must be dissolved to achieve lift-off, the deposited material must not conformally coat the PR; otherwise, the solvent cannot access the PR. Sonication is often used to ensure that lift-off is complete, so the deposited material needs to have sufficient adhesion to the underlying substrate.

To transfer a mask into a material underneath the mask, we then use an etching process. While lift-off is often simpler than etching, there may be system constraints, such as epitaxial or conformal material deposition, that cannot use an underlying masking layer. Etching covers a broad range of techniques, but three specific types will be discussed throughout this thesis. Wet etching consists of a liquid chemical that can dissolve a specific material selectively.⁶⁵⁻⁶⁷ These etches are usually non-directional, so the material exposed or under the PR mask will be etched isotropically (**Figure 1.4, left**). Since wet etches are purely chemical (no physical component) we must consider compatibility with the masking layer so only the desired materials are removed.

In contrast, dry etching uses a plasma to remove material. The most common dry etching tool, known as reactive ion etching (RIE),⁶⁸⁻⁷⁰ operates by flowing gas (or mixture of gases) into a chamber at a specified pressure and igniting a plasma by applying an RF field. The ionized plasma is more directional than wet etches, but in a typical RIE configuration the etch is still partially isotropic (**Figure 1.4, middle**).

Variations of RIE, including cyclic Bosch etches⁷¹ or inductively coupled plasma reactive ion etches (ICP-RIE)⁷²⁻⁷⁴ can achieve more anisotropic profiles and higher aspect ratio features (**Figure 1.4, right**). In an ICP-RIE chamber, a second set of electrodes are used so the density of the plasma can be independently modified of a substrate bias. By tuning parameters like plasma density, gas mixture and pressure of the system, the physical (directional) vs chemical (non-

directional) components can be finely controlled. After optimizing a process to achieve an anisotropic etch profile, the lateral dimensions of a mask can be more directly transferred into an underlying material.

1.3. Active and Dynamic Optical Devices

1.3.1. Introduction to Stimulated Plasmonic Systems

In addition to the intriguing static optical properties of plasmonic structures, plasmonic systems have also been used to induce dynamic responses. The modified interaction with light may manifest in a variety of ways, including tunable resonances and light emission. In order to achieve these expanded capabilities, the system may integrate functional materials (e.g., metal-organic

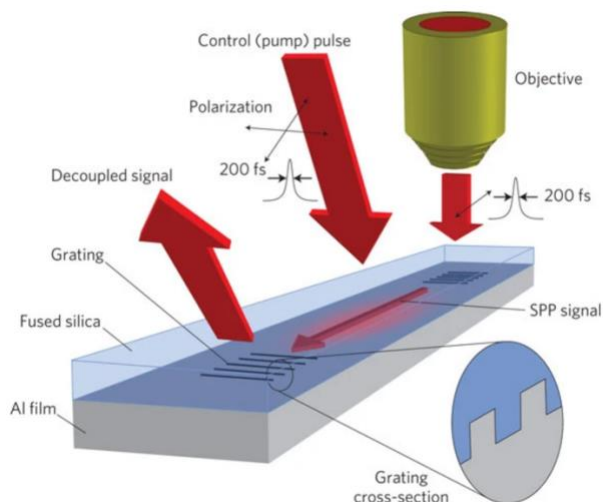


Figure 1.5. Induced transparency in plasmonic systems. Plasmonic device that could actively modulate transmission through intense laser pump. Figure adapted with permission from Springer-Nature, Nature Photonics, reference⁷⁵ Copyright 2009, Nature Publishing Group.

frameworks,^{76, 77} 2D materials,^{78, 79} photochromic molecules^{80, 81} and gain media^{47, 48}) or be externally stimulated (e.g., electrical bias,^{82, 83} mechanical deformation,^{84, 85} ion introduction^{86, 87}

and electromagnetic pulse^{18, 28, 75, 88, 89}). This thesis will explore strategies to fabricate and measure active nanostructures.

1.3.2. Light-responsive Plasmonics

Plasmonic materials have modified transmission and absorption properties when pumped by an optical source. At ultrafast timescales, an electromagnetic pulse can disrupt the electron-gas into a non-thermalized state, which causes a series of scattering events.^{28, 75, 90-95} Before the system recovers to the steady state (usually on the order of picoseconds), transmission is increased at the plasmonic resonance due to depleted photocarriers and therefore less interaction with light. Heating from electron-phonon and phonon-phonon scattering causes the resonance to broaden, and generally lowers transmission on the shoulders of the bleach relative to the non-perturbed system. **Figure 1.5** shows how this dynamic transmission modulation may be used as an optical switch in photonic circuits or information processing. However, most systems studied thus far have been on colloidal NPs or noble metals, which are incompatible with existing CMOS architectures. Producing solid state plasmonic nanostructures will be advantageous for further study into the effect of plasmons on ultrafast transmission modification as well as for future integration into optoelectronic devices.

1.3.3. Plasmonic Structures as Nanolasers

The capabilities of plasmonic devices can be further enhanced by combining them with functional materials. One example is nanolasers based on NP arrays that support SLRs that have been integrated with gain materials (organic dyes in solvent).^{47, 48, 89, 96, 97} Advantages of SLR-organic dye lasers include room temperature operation, narrow lasing linewidths (< 0.5 nm) and low angular divergence.⁹⁷ Due to the collective nature and high quality factor of SLRs, they can

act as cavities similar to a set of mirrors. In this system, optical feedback provides population inversion, which then releases directional and coherent light at the SLR wavelength (**Figure 1.6a-b**). The lasing threshold is characterized by a drastic non-linear increase in emitted light and can be determined by sweeping the incident pump power. In addition to showing promise for miniaturized integrated optoelectronics, lasing action can be used to diagnose optical properties of a system.^{98, 99} The proven SLR system can be used as a platform to explore additional gain media like up-converting nanoparticles,¹⁰⁰ or the standard SLR-organic dye can be used as a benchmark for testing feedback mechanisms of new plasmonic architectures. SLR-based lasers have demonstrated dynamically tuned wavelengths by flowing dyes of different refractive index (**Figure 1.6c**), polarization-dependent lasing from asymmetric units^{99, 101} and multi-modal lasers from multi-modal nanostructures.^{102, 103}

1.3.4. Mechanical Deformation of Plasmonic Lattices

The optical response of plasmonic devices can also be actively tuned through mechanical deformation.^{84, 85, 104-106} Typically, NPs will be embedded into an elastomeric substrate (PDMS) and strained. This platform has been used to generate metasurfaces with tunable focal lengths or

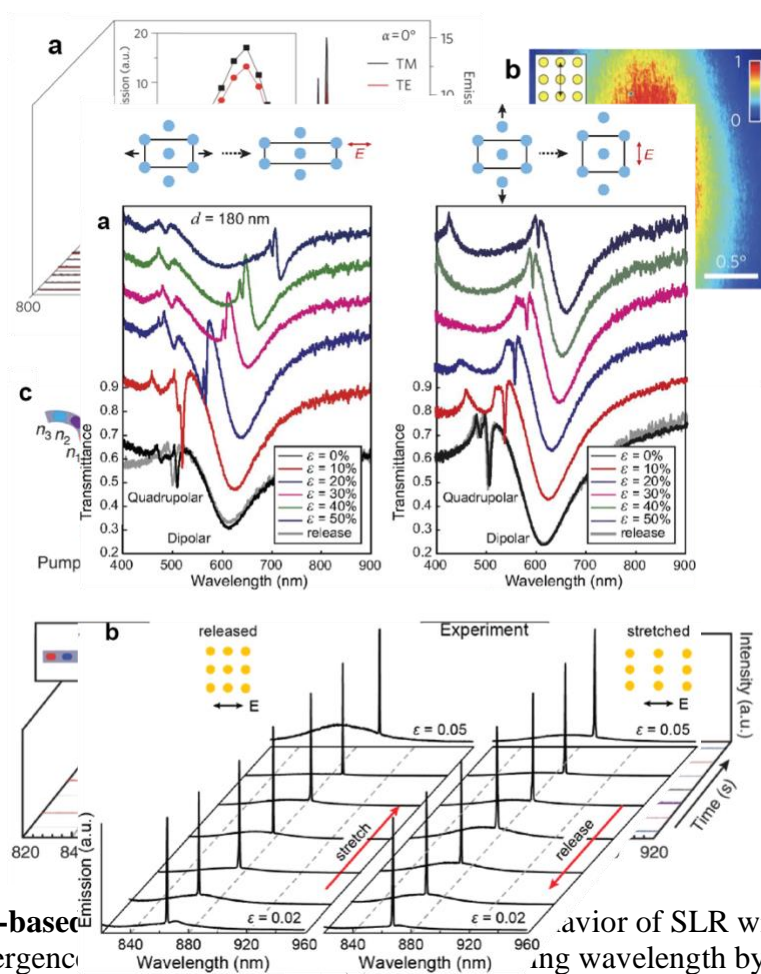


Figure 1.6. SLR-based tunable devices. (a) Schematic of a dipole SLR with lattice constant $d = 180$ nm and incident angle $\alpha = 0^\circ$. The plot shows transmission (a.u.) vs wavelength (nm) for TM (black) and TE (red) polarizations. (b) Schematic of a quadrupole SLR with incident angle $\alpha = 0.5^\circ$. The plot shows emission (a.u.) vs wavelength (nm) for TM (black) and TE (red) polarizations. (c) Transmittance vs wavelength (nm) for dipolar and quadrupolar SLRs with lattice strain $\epsilon = 0\%$, 10% , 20% , 30% , 40% , 50% , and release. (d) Experiment showing emission (a.u.) vs wavelength (nm) vs time (s) for a strained SLR with $\epsilon = 0.02$, showing a redshift during stretching and a blueshift during release.

Figure 1.7. Stretchable NP arrays. (a) Tunable dipolar and quadrupolar SLRs based on lattice strain of a Al NP array embedded in PDMS. (b) Tunable lasing wavelength by a strained Al NP array embedded in PDMS with a liquid gain solution. Panel (a) adapted with permission from ref.¹⁰⁴ Panel (b) adapted with permission from ref.⁸⁵ Copyright (2018) American Chemical Society.

holograms set at different focal planes.^{84, 106} Similarly, periodic arrays of NP that had been transferred into PDMS could dynamically tune the SLR (or lasing) wavelength by changing the lattice spacing (**Figure 1.7**)^{85, 104}. However, these systems require cumbersome setups to stretch the devices. Therefore, future studies may target deformation events which can be achieved spontaneously through a simple environmental change.

1.3.5. *Environment-Sensitive Materials*

One possible route to stimuli-responsive plasmonic architectures is through the use of smart materials. Smart materials can manipulate their mechanical or physical properties based on their surrounding environment. One class of such materials, known as hydrogels, can swell or shrink their dimensions through water absorption.¹⁰⁷⁻¹⁰⁹ As opposed to synthetic polymers, protein-based hydrogels are advantageous because they are inherently bio-compatible and degradable and can be produced at the gram scale through recombinant expression.¹¹⁰⁻¹¹⁴ A number of proteins, including silk cocoons, squid teeth and worm jaws, have displayed robust mechanical properties.^{60, 110, 115-119} In addition, some of these protein hydrogels, such as *Nereis virens* jaw protein (NVJP-1) can achieve ion-dependent responses (**Figure 1.8a**).¹¹⁹ Based on the ionic species introduced, the shrinking ratio and Young's modulus can be tuned over large range. This characteristic can be used to realize a shape memory polymer (**Figure 1.8b**) but could potentially be integrated with plasmonic arrays to generate bio-compatible devices with dynamically tunable SLRs.

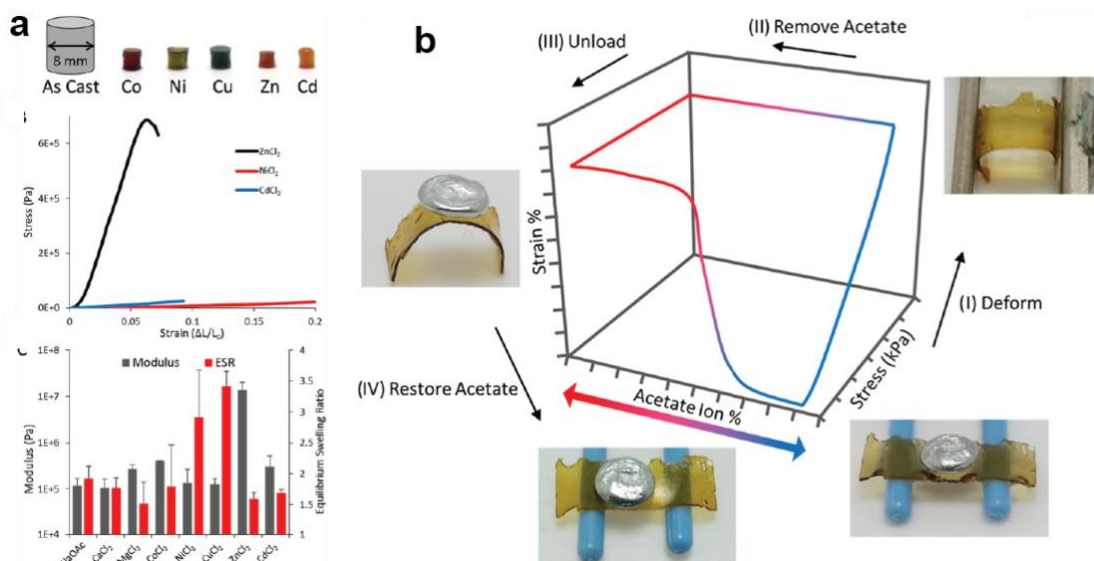


Figure 1.8. Dynamic mechanical properties of protein hydrogels (a) Modulus and swelling ratios for NVJP-1 hydrogels after introduction of various cations. (b) Reversible mechanical properties through anion exchange. Figure adapted with permission from ref.¹¹⁹ Copyright (2018) American Chemical Society.

1.4. Outline of Thesis

The remainder of this dissertation describes new methods to fabricate active nanostructures and the characterization of their properties. In Chapter 2, I show a parallel nanofabrication technique for generating partially-filled or multi-metallic NP arrays. By integrating the partially filled arrays with liquid gain media, I was able to realize active devices that could support lasing action at NP filling factors as low as 10%. Then, I modified the process flow to incorporate a second and third array of metal NPs without increasing the thickness of the device. The regions of each metal array were separated into quasi-periodic patches of NPs with little overlap. For each array, I could select the material, periodicity, NP size independently. Depending on the periodicities and materials chosen, the multi-metallic arrays could support multiple SLRs across the visible and near-infrared regimes. I found that bi-metal (Al-Au) NP arrays could act as bi-modal cavities to achieve lasing at wavelengths separated by over 130 nm simultaneously. Tri-

metallic (Al-Ag-Au) NP arrays were able to achieve lasing in the visible and near-infrared at wavelengths separated by over 200 nm.

Chapter 3 discusses the fabrication of titanium nitride nanoparticle arrays that could support different plasmonic resonances depending on the local refractive index environment. Because the ultrafast properties of TiN are distinct from previously studied noble metals, TiN nanoparticle arrays proved to be an ideal platform for determining the effect of plasmonic resonance character on ultrafast transmission modulation. In addition, the physically robust nature of TiN allowed us to probe changes in transmission at extremely high pump fluences. I extended the nanofabrication process to generate arrays of AlN on TiN NPs and found that the presence of AlN could significantly alter the broadband relaxation dynamics.

Chapter 4 explores ordered protein hydrogel nanostructures. By taking advantage of the spontaneous contraction of Suckerin-12 hydrogels that occurs during ionic crosslinking, I was able to realize nanoscale grating features from microscale masks. Further, by functionalizing the surface of the mask, I was able to directly replicate sub-micron lateral dimensions into a Suckerin-12 architecture. I also formed nanostructured *Nereis virens* jaw protein-1 hydrogels and found they had similar contraction percentage to Suckerin-12. The patterned protein hydrogels were imaged by AFM in a buffer solution environment, which distinguishes this work from reports of dry contracted protein hydrogels. Future directions of this project will pursue transferring metallic NP arrays into NVJP-1 and reversibly controlling the lattice dimensions.

Chapter 2

Multi-Color Lattice Plasmons from Multi-Metal Nanoparticle Arrays

Related publication:

T. Reese, D. Rhee, J. Guan, R. Li, R. Schaller, T.W. Odom, "Multi-Color Lattice Plasmons from Multi-Metal Nanoparticle Arrays," *In Preparation*.

2.1. Introduction

Miniaturized optical components may have future applications in a variety of fields, including on-chip optical communication,¹²⁰ biological sensing^{43, 121, 122} and low power lighting. Plasmonic structures can manipulate light below the diffraction limit and therefore constitute an attractive platform for nanoscale optics. Arrays of plasmonic nanoparticles (NPs) can support collective modes known as surface lattice resonances (SLRs), which have higher local electric fields and narrower linewidths than isolated particles that support localized surface plasmons (LSPs).³⁶⁻⁴¹ SLRs have been used as a building block of numerous nanoscale devices, such as lasers and lenses, because of their high quality factors.^{47, 48, 89, 96, 97, 123} More recently, reports have shown that single or discontinuous arrays of microscale patches could still support SLRs and achieve lasing action.^{102, 124, 125} By lowering the spatial footprint occupied by the NPs, future architectures could incorporate additional materials or components to increase the functionality in the same area. Plasmon-assisted distributed feedback devices have shown lasing with filling factors as low as 1% filling factor,^{126, 127} but these require waveguide layers that increase the thickness of the active layer beyond the diffraction limit. If SLRs can be sustained by low NP filling factors, the height of nanoscale components using NP arrays would only be dictated by the height of the NPs.

An avenue to increasing the optical throughput of a photonic device without increasing size is through multiplexing. Thus far, multiple SLRs arising from a single array have consisted of a single lattice geometry⁹⁸ or NP unit composed of one metal.^{99, 101} These dimensional and material constraints restrict SLRs to wavelengths with low metallic losses, within the LSPs of the individual units and near the diffraction modes of the lattice. Micro lenses composed of multiple metals have been used to focus visible light throughout the visible regime,¹²⁸ but these structures were hundreds

of nanometers thick and required electron-beam lithography (EBL) with alignment markers. Single layer, multi-metal NP arrays devices may expand the functionality of an optical component without increasing thickness.

In this chapter, I demonstrate a scalable fabrication process that can achieve partially-filled or multi-metallic NP arrays. I found that Al NP arrays with filling factors as low as 10% could support SLRs and lasing action with only a modest increase in threshold from uniform lattices. The robustness of SLRs in discontinuous lattices led us to fill the newly available space with NP arrays composed of different materials (Au and/or Ag), lattice spacings and NP dimensions. Bi-metallic arrays could support lasing modes from both SLRs, either individually or simultaneously. Tri-metallic arrays supported three distinct SLRs and lasing wavelengths separated by over 200 nm. Our platform is agnostic to lattice geometry and material, which allows it to be extended to a variety of photonic applications or areas of study depending on system constraints.

2.2. Process Flow for Fabricating Partially Filled or Multi-metal NP Arrays

Figure 2.1 shows the process flow for fabricating single or bi-metallic NP arrays with controllable filling factors. We create PDMS molds from 3D microwrinkles with tunable quasi-periodicity based on the thickness of Cr film deposited by thermal evaporation on PDMS (**Figure 2.1a**).¹²⁹ **Figure 2.1b** shows how to achieve either partially-filled or bi-metallic arrays from an initial metal NP array (M1) with a given periodicity (a_{M1}). M1 NPs are patterned through PEEL, then coated in a layer of etch-resistant photoresist (PR, Shipley 1805). The PDMS masks from **Figure 2.1a** are used in a process known as solvent-assisted nanoembossing (SANE)⁵⁹ to form quasi-random PR wrinkles on top of the M1 NPs. The filling factor of the PR can be tuned by the

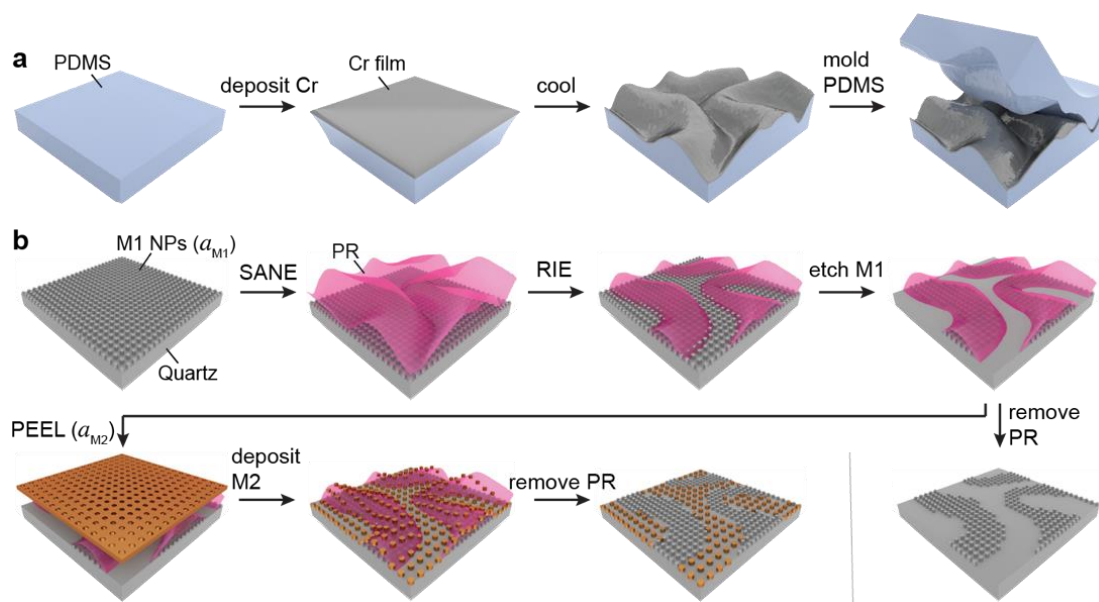


Figure 2.1. Scalable process flow for partially filled and bimetallic NP arrays with controllable filling factor. (a) Molding PDMS SANE masks from quasi-random Cr microwrinkles. **(b)** Partially filled NP arrays or bimetallic NP arrays with RIE-tunable filling factor

exposure time to an O_2 based reactive ion etch (RIE).¹³⁰ We then propose to use a wet etch to remove the exposed M1 NPs, which will completely dissolve even partially exposed NPs. If we desire a partially filled, single metal array, we also remove the residual PR. If we intend to fabricate a bimetallic array, we float a second Au hole mask formed by PEEL with a second periodicity (a_{M2}) onto the PR wrinkles and deposit a new metal (M2) through the pattern. Finally, we remove the PR to fully liftoff the M2 NPs on top of the M1 NP regions to result in bi-metallic array.

2.3. Controlling Photoresist Coverage and Nanoparticle Array Filling

2.3.1. Quasi-Random Photoresist Wrinkles

Figure 2.2 shows the scalability and fidelity of the pattern transfer process for producing soft lithography stamp with quasi-random microwrinkles. After chromium deposition (120 nm), the PDMS slab exhibited uniform wrinkles over centimeter scale areas ($\sim 4 \text{ cm}^2$) (**Figure 2.2a**). These

features were characterized by a quasi-periodicity (wrinkle wavelength, $\lambda \approx 4.5 \mu\text{m}$) without a preferred orientation (**Figure 2.2b**), which was confirmed by a radially symmetric ring in the 2D fast Fourier transform (FFT) image (Figure 2.2b, inset). We then replicated the textures into composite PDMS that could be used as a stamp to pattern PR. The patterns were uniformly replicated over the full centimeter scale area (**Figure 2.2c**) with the same quasi-periodicity with the master (**Figure 2.2d**).

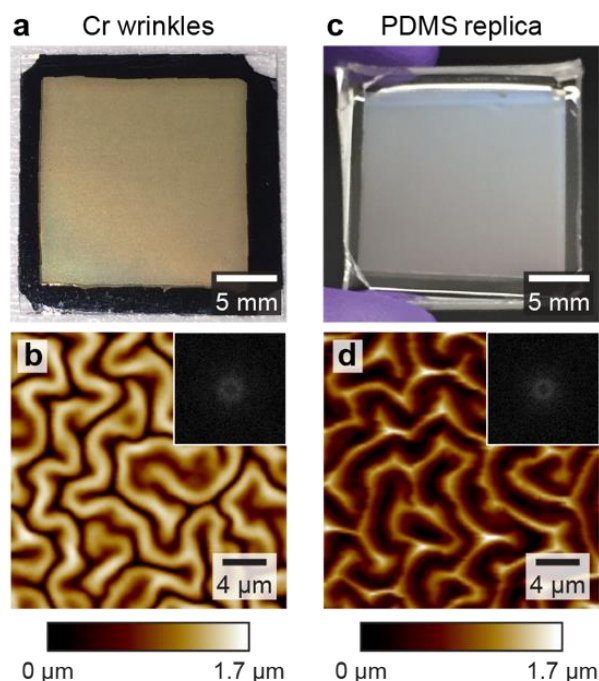


Figure 2.2. Scalability and fidelity of the pattern transfer process for quasi-random stamp fabrication. Chromium wrinkles under (a) optical and (b) AFM topography images. PDMS replica under (c) optical and (d) AFM topography images. Insets in panels b and d shows 2D FFT of the AFM images.

We then characterized the relationship between etch time (t) and PR filling factor (f_{PR}) using the PDMS mold formed in **Figure 2.2**. We spin coated PR (1:1 Shipley 1805 to PGMEA) onto Si wafers and performed SANE with the microwrinkle PDMS mask. **Figure 2.3a** shows AFM images

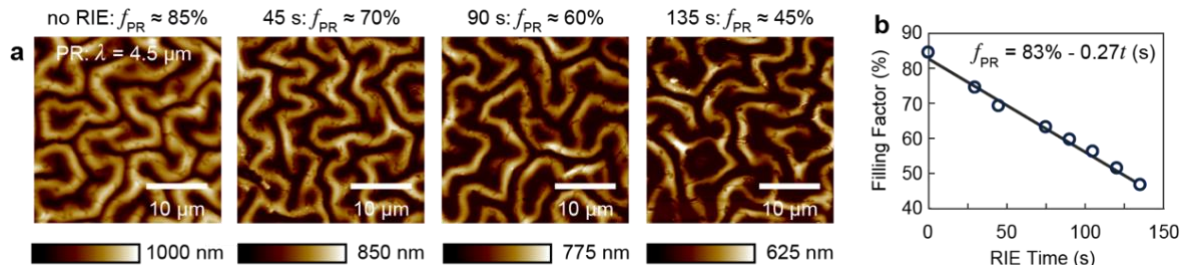


Figure 2.3. Relationship between RIE time and photoresist filling factor. (a) AFM images showing PR wrinkles on Si wafers after given RIE time. (b) Graph showing the linear function of decreased filling factor with increased RIE time ($R^2 = 0.9932$).

of PR features with different f_{PR} after given O_2 RIE times. As the height of the PR features shrinks through etching, more of the Si wafer becomes exposed. f_{PR} follows a linear relationship to etch time of $83\% - 0.27t$ (Figure 2.3b) which gives us a general trend to expect for filling factor of NPs.

2.3.2. Partially Filled NP Arrays

We studied partially filled Al NPs as our initial M1 with period $a = 400 \text{ nm}$ because Al does not require an adhesion layer to deposit on quartz or a passivation layer to eliminate oxidation, so

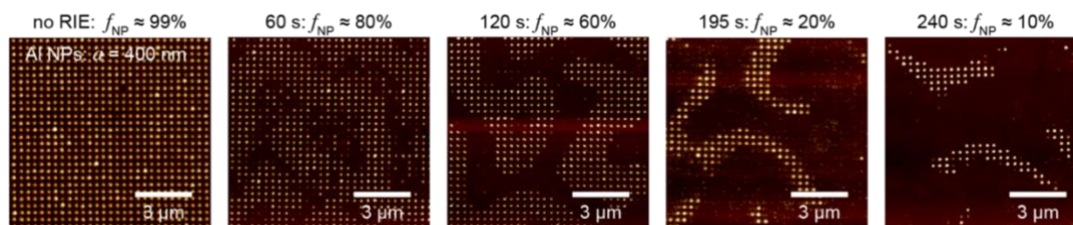


Figure 2.4. Partially filled NP arrays. AFM images showing quasi-random patches of Al NPs with filling factors ranging from 99%-10% by changing RIE time before Al wet etch. Arrays have $a = 400 \text{ nm}$ and are 60 nm thick with an approximate diameter of 90 nm.

we expect more complete removal by a wet etch. Figure 2.4 shows that we are able to tune f_{NP}

continuously from 100% to below 10% by increasing the O₂ RIE time before etching the exposed NPs. This process can achieve nanoscale variation in NP patches that is not possible through photolithography techniques. In addition, we see nearly complete removal of the unprotected NPs, which results in uniform dimensions for the remaining NPs.

2.4. Optical Properties of Partially Filled Al NP Arrays

2.4.1. Static Transmission Measurements

After fabricating partially filled Al NP arrays, we measured the static transmission spectra with a rotational stage equipped with a photospectrometer. **Figure 2.5** shows that decreased filling factor decreases the magnitude of the dip at the SLR wavelength ($\lambda = 580$ nm) but can still be distinguished from noise for $f_{\text{NP}} \approx 20\%$. SLRs appear to slightly broaden, but their peak wavelength

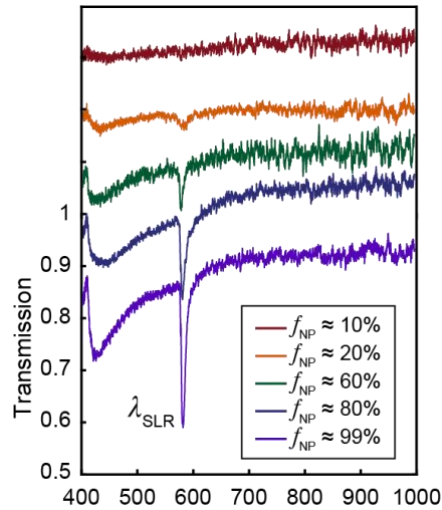


Figure 2.5. Transmission spectra of partially filled NP arrays. Steady-state spectra taken for the partially filled NP arrays shown in figure 2.4. Samples were index-matched with fluid $n = 1.45$. Arrays have $a = 400$ nm and are 60 nm thick with an approximate diameter of 90 nm.

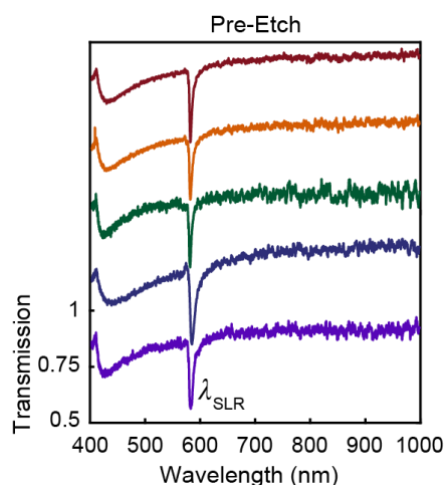


Figure 2.6. Transmission spectra of fully filled NP arrays. Steady-state spectra taken for the NP arrays shown in figure 2.5. The color of each trace corresponds to the sample used before etching.

do not shift. Despite having quasi-periodic patch-to-patch spacing, the SLRs do not show peak splitting intrinsic to superlattice coupling.^{102, 124} To ensure that the initial samples supported similar SLRs, we measured each array prior to patterning PR wrinkles, RIE and Al etch (**Figure 2.6**). We compared the experimental spectra to finite-difference time-domain simulations to determine if the trends were consistent with calculations. **Figure 2.7** shows that simulations also predict significant dip reduction and slight peak broadening while maintaining the SLR at $\lambda = 580$ nm.

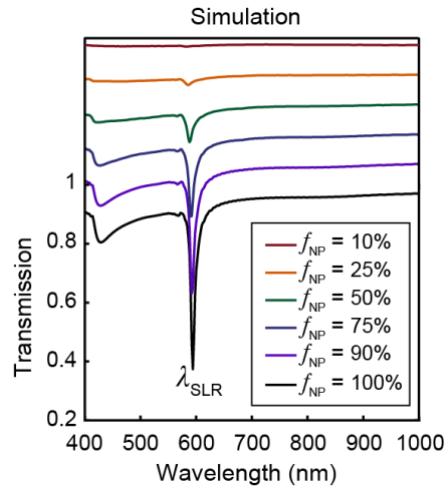


Figure 2.7. FDTD calculated transmission spectra of partially filled NP arrays.

Simulations used $30 \times 30 \mu\text{m}^2$ regions with perfectly matched layers in $\pm x$, $\pm y$ and $\pm z$ directions. Quasi-period was introduced by binarizing an AFM image of the micro wrinkle mask used in fabrication with a threshold set to achieve the given filling factor. The binarized Al NPs had $a = 400$ nm, thickness of 60 nm and diameter of 90 nm.

In order to confirm that the quasi-periodicity of the partially filled arrays did not introduce additional off-normal modes (from superlattice splitting), we measured dispersion diagrams of each sample. **Figure 2.8** shows that all samples have the expected band edge modes under TE light polarization for a square lattice. We observe no off-angle band edges, which conclusively shows that quasi-periodic patches do not introduce superlattice modes. These dispersion diagrams also allow us to resolve the SLR modes for filling factors as low as $f_{NP} \approx 10\%$.

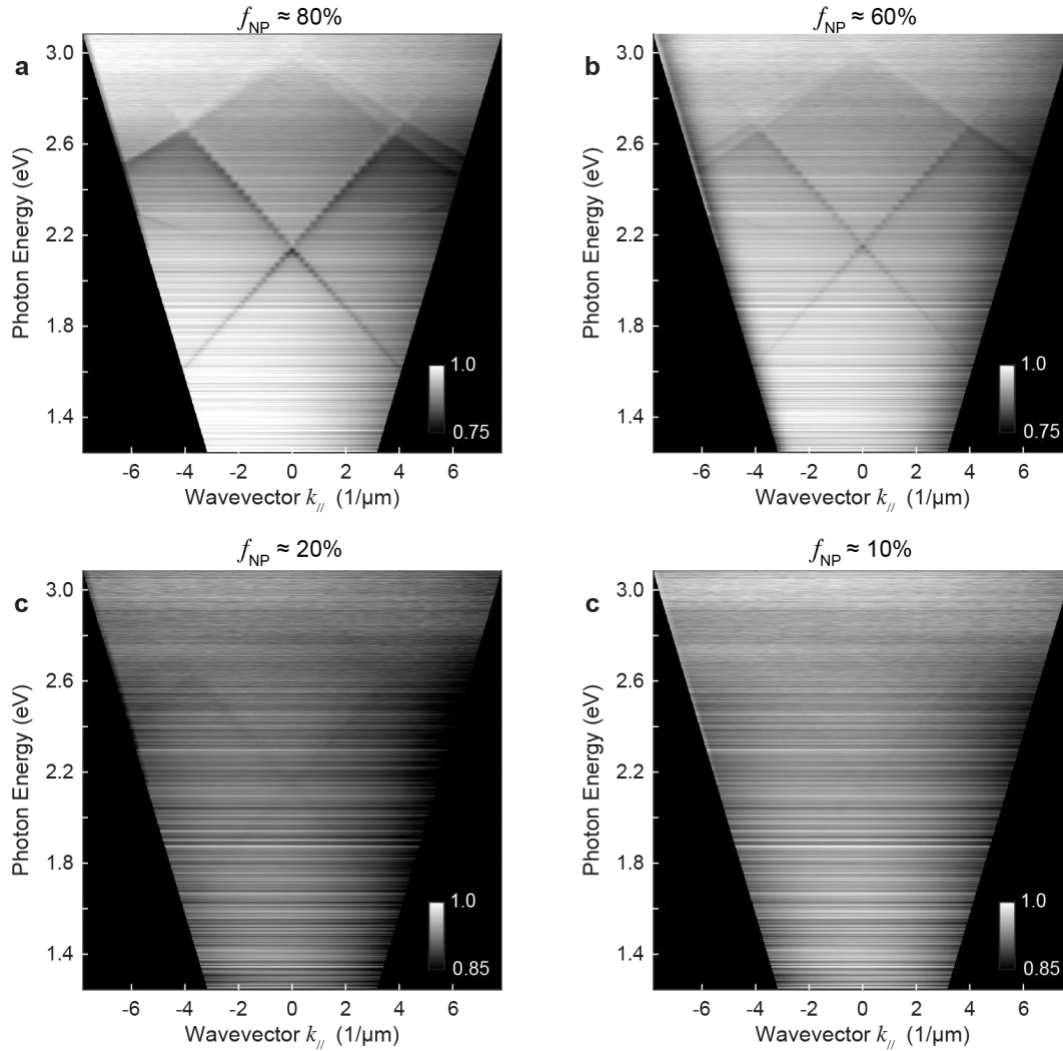


Figure 2.8. Dispersion diagrams of partially filled NP arrays. Energy-momentum dispersion diagrams for partially filled Al NP arrays with $f_{\text{NP}} \approx$ (a) 80%, (b) 60%, (c) 20% and (d) 10%. White light probe was set to TE polarization with respect to the samples.

2.4.2. Lasing Performance of Partially Filled NP Arrays

While nanoscale lasers are often viewed as an application of plasmonic nanostructures, lasing action can also be used as a diagnostic tool to determine if a plasmonic mode provides sufficient feedback for population inversion. We performed lasing experiments with our partially filled Al

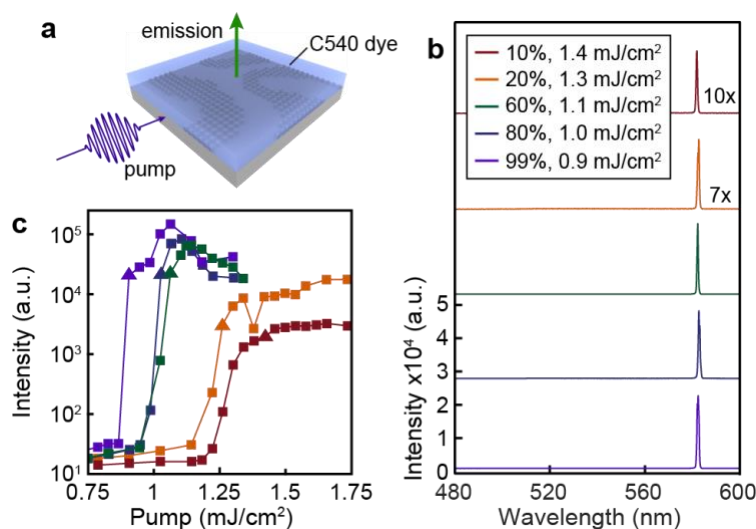


Figure 2.9. Lasing action from partially filled Al NP arrays. (a) Scheme showing a partially filled NP array with gain material being pumped by a femtosecond pulse laser. (b) Lasing spectra for partially filled NP arrays and (c) their corresponding light in-light out plots. 50 mM C540 dye was dissolved in DMSO for all experiments and samples were pumped by a $\lambda = 400$ nm laser.

NP arrays to probe the effect of filling factor on lasing behavior. **Figure 2.9a** provides a diagram for our architecture, with an incident $\lambda = 400$ nm femtosecond pulsed laser pumping the partially filled NP array integrated with a gain material (Coumarin-540) that has emission overlapping with the SLRs. **Figure 2.9b** shows that the SLRs supported by Al NP arrays with filling factors as low as $f_{\text{NP}} \approx 10\%$ can achieve lasing. We observe no additional lasing modes (from superlattice mode splitting), which is consistent with our steady-state results. In addition, lower filling factors have no discernable effect on the full-width half-maximum (FWHM) of the lasing spectra. These experiments suggest that SLR modes maintain their collective resonance even with significant discontinuities in the NP array. From light in-light out plots, (**Figure 2.9c**) we see clear threshold behavior that is associated with lasing action. However, the lasing intensity above threshold decreases with decreased filling factor, which we attribute to a lower concentration of gain

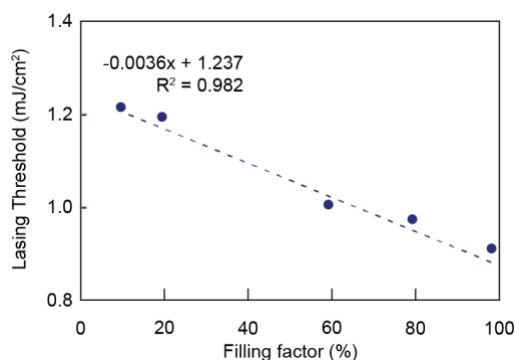


Figure 2.10. Linear relation of lasing threshold to NP filling factor

molecules that can be involved in the lasing process. The increase in threshold with decreased f_{NP} is modest; The necessary fluence to achieve lasing for $f_{NP} \approx 10\%$ is only 1.3x larger than $f_{NP} \approx 99\%$. **Figure 2.10** shows a linear relationship between f_{NP} and lasing threshold.

2.5. Bi-Metallic NP Arrays

2.5.1. Bi-metallic NP Array Fabrication

After finding that partially filled NP arrays with $f_{NP} < 50\%$ can support high quality SLRs and lasing action, we sought to determine if we could include additional metal arrays to excite multiple SLRs. We began with Al NP arrays ($M1$, $a_{M1} = 400$ nm) with $f_{NP} \approx 50\%$, but before removing the residual PR, we floated a second Au hole mask ($a_{M2} = 500$ nm) that was fabricated by PEEL onto the Al NP array and PR wrinkle structure. The PR wrinkles (**Figure 2.11a**) and Al NPs (**Figure 2.11b**) do not disturb the periodicity or introduce significant defects to the floated mask. Regions with PR increase the contrast seen in SEM images. We then

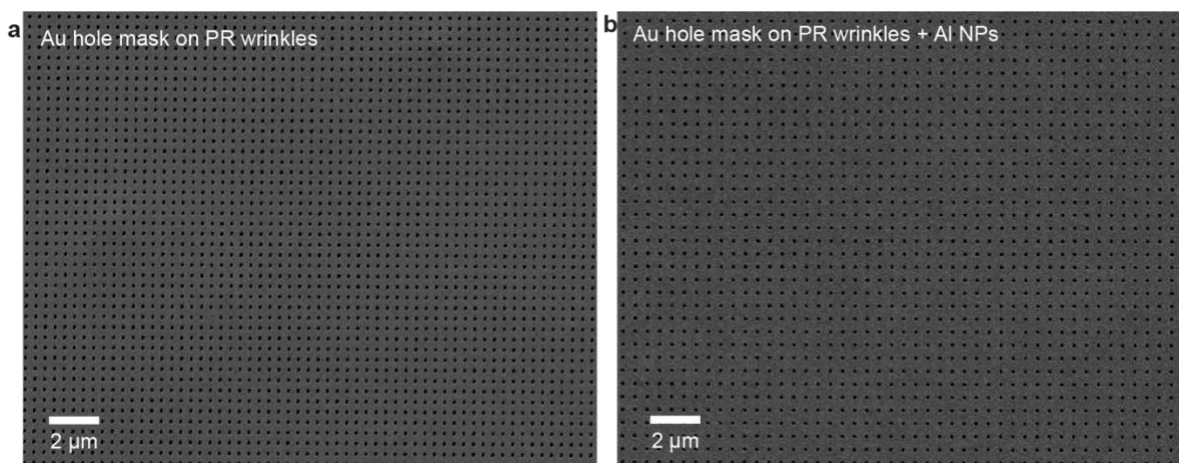


Figure 2.11. Au hole masks fabricated by PEEL floated onto PR microwrinkles. Au hole masks have (a) $a = 400$ nm floated onto PR wrinkles and (b) $a = 500$ nm floated onto PR wrinkle-protected Al NPs

deposit Au as a second metal (M2) through the hole mask. The Au hole mask is stripped by tape, then the sample is sonicated in a PR removal solvent (Microposit photoresist remover 1165) to liftoff the Au NPs above the PR-protected Al NP regions (**Figure 2.1** and **Figure 2.12a**). The samples were briefly treated with rapid thermal annealing to increase the quality of Au NPs.⁷⁹

Figure 2.12b shows that this process flow can incorporate multiple materials into the same

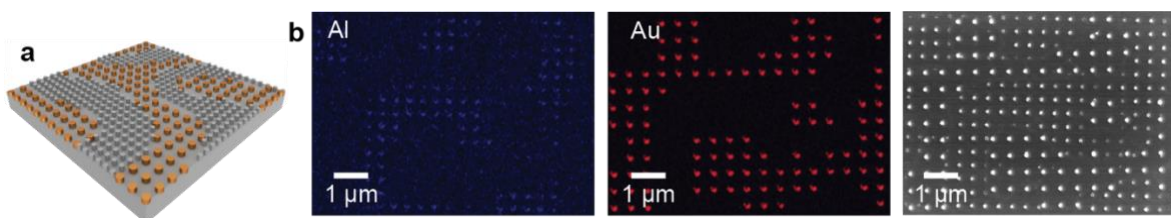


Figure 2.12. Imaged Al and Au bi-metallic NP arrays. (a) Scheme depicting Al and Au bi-metallic NP array with $a_{Al} = 400$ nm and $a_{Au} = 500$ nm. (b) SEM and EDS images taken of an Al-Au bi-metallic NP array.

footprint while maintaining distinct areas with consistent periodicity and NP diameter. The EDS SEM images show a densely packed substrate with nearly no overlap between Au and Al patches. Despite floating the Au hole mask without sophisticated tools, we were able to achieve relatively low misalignment between the two lattices.

2.5.2. Optical Properties of Bi-metallic NP Arrays

We proceeded to measure the static and non-linear properties of bi-metallic NP arrays.

Figure 2.13a shows that bi-metallic arrays are able to support two distinct SLRs corresponding to

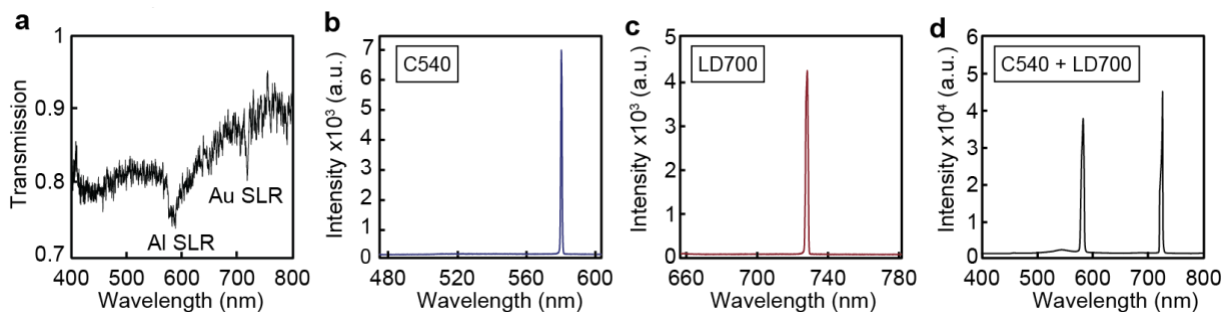


Figure 2.13. Optical properties of Al and Au bi-metallic NP arrays. (a) Transmission spectra of a bimetallic NP array. Lasing spectra for a bi-metallic array integrated with (b) 50 mM C540 and pumped at 1.21 mJ/cm², (c) 10 mM LD700 and pumped at 1.61 mJ/cm² and (d) mixture of 40 mM C540 and 2.5 mM LD700 and pumped at 2.13 mJ/cm². Bi-metallic array consisted of Al NPs with $a = 400$ nm and thickness of 60 nm and Au NPs with $a = 500$ nm and thickness of 60 nm. All dyes were dissolved in DMSO. Samples were irradiated with a femtosecond laser at $\lambda = 400$ nm for lasing experiments.

each metal and accompanying period (Al with $a = 400$ nm SLR at $\lambda = 580$ nm and Au with $a = 500$ nm SLR at $\lambda = 715$ nm). While the Al SLR is relatively broad compared to the partially filled Al NP arrays, the Au SLR is quite sharp. These results suggest that the NPs of each metal array can form SLRs across space occupied by plasmonic NPs of separate period and metal. By integrating C540 into the bi-metallic NP arrays and pumping with a pulsed laser with $\lambda = 400$ nm we could achieve lasing at the Al SLR (**Figure 2.13b**). We also observed lasing at the Au SLR by replacing the C540 with LD700 (**Figure 2.13c**). Finally, by using a mixture of C540 and LD700, we were able to achieve bimodal simultaneously (**Figure 2.13d**). We recorded light in-light out curves of the bi-metallic arrays at the Al SLR with C540 (**Figure 2.14a**) and Au SLR with LD700 (**Figure 2.14b**) and found the lasing threshold was similar to the partially filled Al arrays.

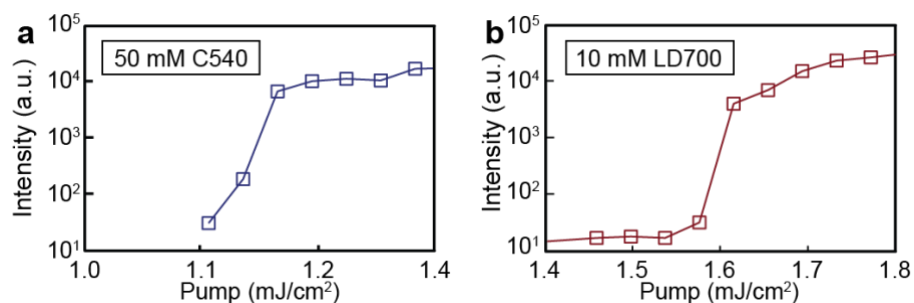


Figure 2.14. Light-light curves for bi-metallic NP arrays. Lasing intensity as a function of pump fluence at the (a) Al SLR with C540 dye and (b) Au SLR with LD700. $a = 400$ nm floated onto PR wrinkles and (b) $a = 500$ nm floated onto PR wrinkle-protected Al NPs

2.5.3. Aluminum and Silver Bi-metallic NP Arrays

To display the flexibility of our bi-metallic fabrication procedure, we also generated bi-metallic arrays consisting of Al ($a = 400$ nm) and Ag ($a = 500$ nm) NPs (**Figure 2.15**). SEM and EDS images in **Figure 2.15a-c** show that Ag also fully lifts off during PR removal, so Al and Ag NP regions remain distinct. Ag has lower metallic losses than Au in the visible regime, so we did not need to use rapid thermal annealing to realize sharp SLRs (**Figure 2.15d**), but the samples were passivated by 3 nm of ALD Al₂O₃ to reduce oxidation of the Ag NPs.

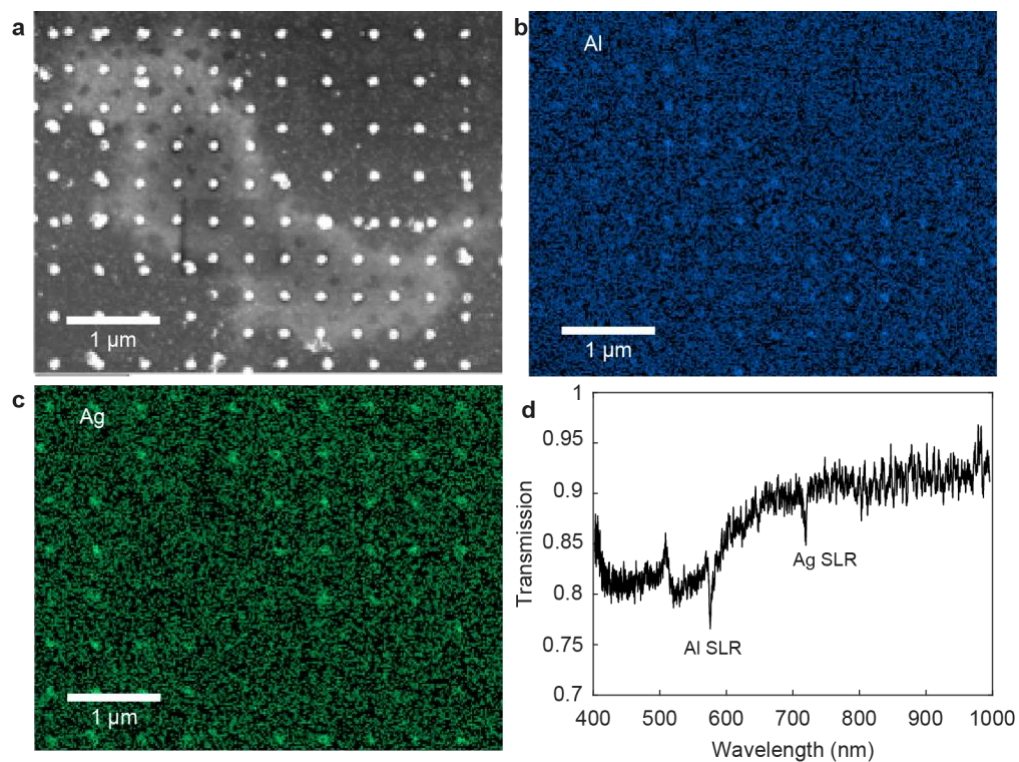


Figure 2.15. Al-Ag bi-metallic NP arrays. (a) SEM image of an Al-Ag bi-metallic NP array and EDS signal of the (b) Al and (c) Ag NPs. (d) Transmission spectra of Al-Ag bi-metallic array showing Al and Ag SLRs.

2.6. Tri-Metallic NP Arrays

2.6.1. Fabrication of Tri-metallic NP Arrays

The ability of bi-metallic NP arrays and NP arrays with $f_{\text{NP}} \approx 10\%$ to support high-quality SLRs and demonstrate lasing suggests that systems with more than two materials may still produce long-range collective resonances. We expanded our process flow to generate tri-metallic arrays from bi-metallic NP arrays (**Figure 2.16a**). After fabricating a bi-metallic array, we spincoat a layer of PR on the sample and perform SANE with a quasi-periodic microwrinkle PDMS stamp. We expose the structure to O_2 plasma and target $f_{\text{PR}} \approx 66\%$ so after chemical etching of the first two materials each component of tri-metallic NP array will consist of approximately even spatial areas. We then float an additional Au hole mask fabricated by PEEL, deposit our third material and liftoff PR. This scalable procedure remains agnostic with regards to material and lattice geometry for each set of NP arrays. **Figure 2.16b** shows we are able to successfully fabricate tri-metallic NP arrays over large areas. This array began as an Al NP array with $a = 300$ nm, transitioned to a bi-

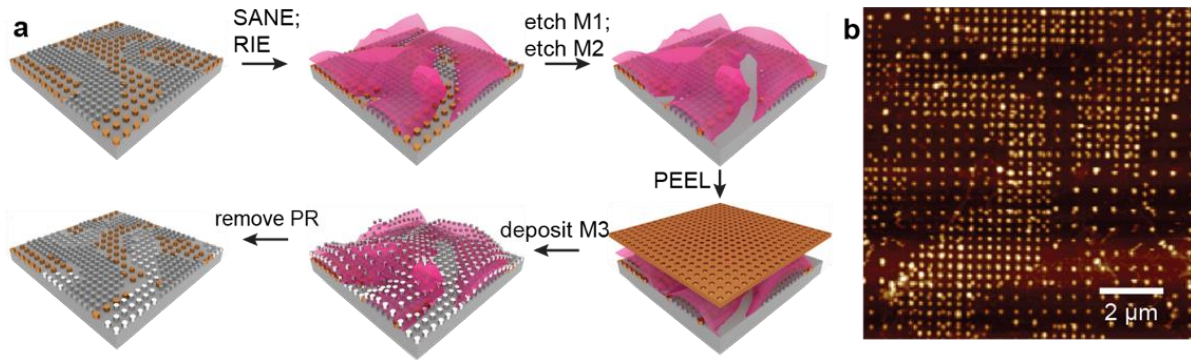


Figure 2.16. Tri-metallic NP array fabrication. (a) Scheme depicting the process flow for producing tri-metallic NP arrays after starting with bi-metallic NP arrays. (b) AFM image of Al-Ag-Au NPs array with $a_{\text{Al}} = 300$ nm, $a_{\text{Ag}} = 450$ nm and $a_{\text{Au}} = 600$ nm.

metallic array with the addition of Au NPs with $a = 600$ nm and became a tri-metallic array with the incorporation of Ag NPs with $a = 450$ nm. All three NP arrays were 60 nm thick. After fabrication was complete, the tri-metallic NP array was coated in approximately 3 nm of ALD Al_2O_3 to reduce degradation of Ag NPs. Each region remains spatially distinct from each other

with nearly complete removal by each wet etch and PR liftoff.

2.6.2. *Optical Properties of Tri-metallic NP Arrays*

Figure 2.17a shows the transmission spectra of original (fully filled) NP arrays from Figure 2.16b. The Al NP array has $a = 300$ nm with an SLR at $\lambda = 435$ nm, the Ag NP array has $a = 450$ nm with an SLR at $\lambda = 648$ nm and the Au NP array has $a = 600$ nm with an SLR at $\lambda = 860$ nm. These three resonances range from blue wavelengths in the visible regime to the near infrared. **Figure 2.17b** shows sharp Al and Au SLRs in the visible and NIR respectively can be observed after fabricating a bimetallic array according to the process described in **Figure 2.1**. Finally, **Figure 2.17c** shows the normal incidence transmission spectra of the tri-metallic array shown in **Figure 2.16b**. While the Al and Ag SLRs are distinguishable and at the same wavelength as their fully filled NP arrays, the Au SLR is difficult to observe. **Figure 2.18a** shows all three SLRs can be more clearly seen in a dispersion diagram. Each SLR follows the expected dispersive properties based on TE polarization. No band edges appear at off-normal angles, which indicates the individual SLRs do not interact with each other to form hybrid modes. These results suggest that multiple material arrays can be integrated onto a single substrate while retaining many of their

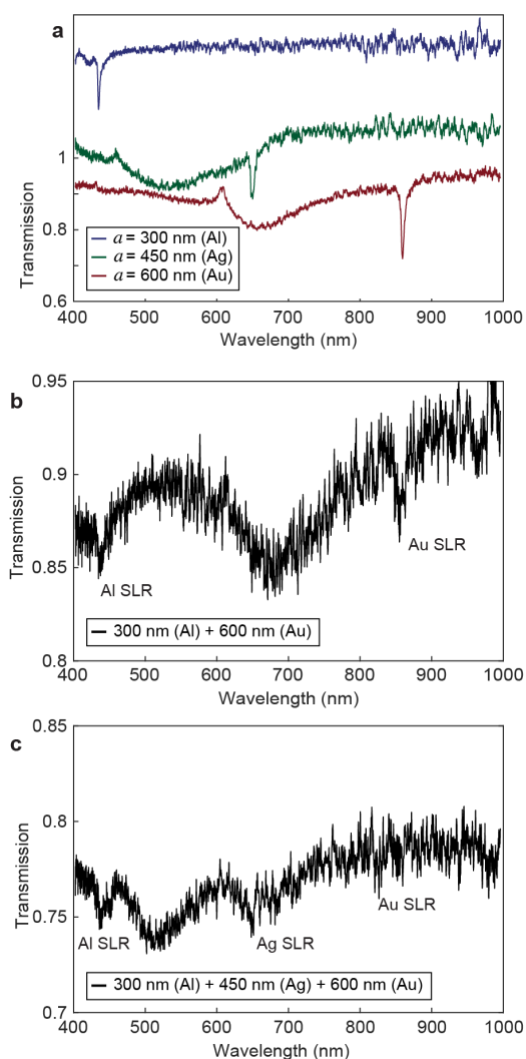


Figure 2.17. Normal incidence transmission spectra of tri-metallic NP arrays and their constituent NP arrays. (a) Fully filled NP arrays for Al ($a = 300$ nm), Ag ($a = 450$ nm) and Au ($a = 600$ nm). **(b)** Bi-metallic array consisting of approximately half Al ($a = 300$ nm) and half Au ($a = 600$ nm). **(c)** Tri-metallic array after integrating approximately 33% Ag ($a = 450$ nm).

original optical properties.

Because the SLRs for the tri-metallic NP arrays are weaker and broader than for the bi-metallic (and partially filled single metal) NP arrays, we probed their ability to support lasing action. **Figure 2.18b** shows that by incorporating an organic dye (DCM) and pumping with a $\lambda = 400$ nm femtosecond pulsed laser, the Ag SLR from the tri-metallic NP array could support lasing in the

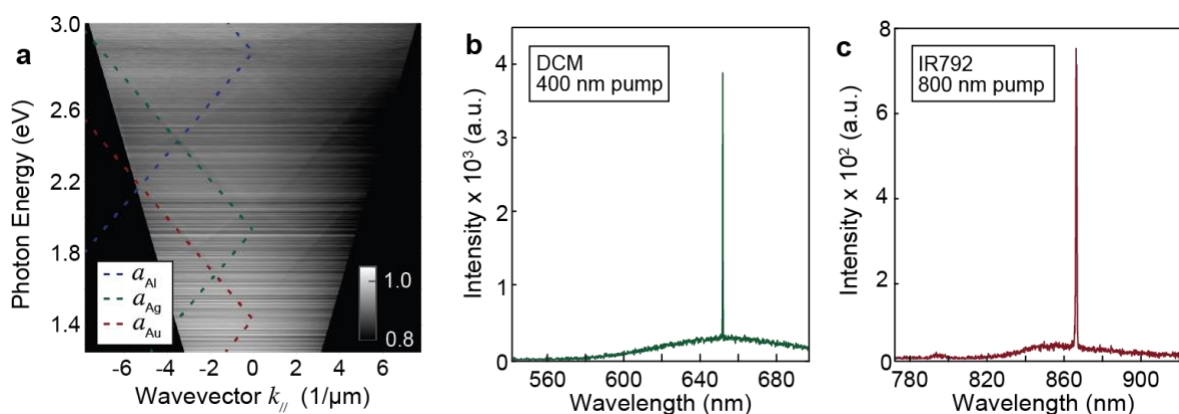


Figure 2.18. Optical properties of tri-metallic NP arrays. (a) E - k dispersion diagram for a tri-metallic NP array. Lasing spectra of the tri-metallic array when integrated with (b) 5 mM DCM dissolved in DMSO and pumped at $\lambda = 400$ nm and (c) 10 mM IR792 dissolved in DMSO and pumped at $\lambda = 800$ nm.

visible regime at $\lambda = 648$ nm. This measurement indicates SLRs provide adequate feedback to achieve lasing from samples with multiple NP arrays and $f_{NP} \approx 33\%$. To test if these tri-metallic arrays could lase in the NIR, we placed a liquid solution of IR792 on sample and pumped with $\lambda = 800$ nm femtosecond pulsed laser. **Figure 2.18c** shows the trimetallic NP array can also support a lasing mode at $\lambda = 860$ nm. These lasing experiments provide evidence that a tri-metallic array can excite multiple SLRs with high enough local field enhancements to support multiple lasing modes. The viability of the Al SLR to support lasing will be investigated in the future (a UV femtosecond pulsed laser source was unavailable due to the Covid-19 global pandemic). We attempted to measure bi-modal lasing from the Ag and Au SLRs simultaneously, but due to absorption of IR792 overlapping with emission of DCM we did not observe any lasing peaks.

2.6.3. Tri-metallic NP Arrays with 3 SLRs in the Visible Regime

To demonstrate a single tri-metallic NP array that supported three SLRs in the visible regime, we fabricated a sample with $a_{\text{Al}} = 300$ nm, $a_{\text{Ag}} = 400$ nm and $a_{\text{Au}} = 500$ nm. **Figure 2.19a** the tri-metallic process flow is flexible to periodicity changes as well as material changes. Al NPs were not completely removed due to inadequate wet etching time. **Figure 2.19b** shows that this tri-

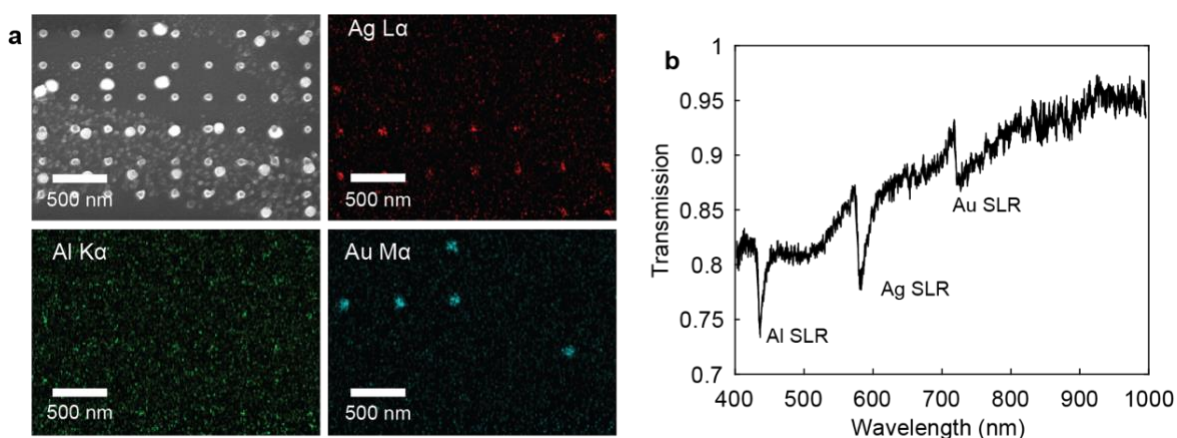


Figure 2.19. Visible-regime tri-metallic NP arrays. (a) SEM and EDS images and (b) transmission spectra of a trimetallic NP array with $a_{\text{Al}} = 300$ nm, $a_{\text{Ag}} = 400$ nm and $a_{\text{Au}} = 500$ nm.

metallic array is able to support SLRs at $\lambda = 436$ nm, $\lambda = 586$ nm and $\lambda = 730$ nm originating from the Al, Ag and Au NP array components respectively. These results highlight the flexibility of our multi-metallic nanofabrication procedure and the ability to tailor the optical properties by modifying the constituent array periodicities.

2.7. Conclusions

In summary, we demonstrated a scalable fabrication technique that could generate partially filled or multi-metallic NP arrays with controllable filling factors. Many of the parameters of these arrays could be chosen and tailored independently, including material, lattice spacing and NP dimensions. When integrated with gain media, we found that quasi-periodic patches of NP arrays

with filling factors approaching 10% could still act as nanoscale cavities to achieve lasing action with only a moderate increase in pump threshold. Bi-metallic arrays with two periodicities could support SLRs and lasing in the visible and NIR simultaneously. We extended the process to tri-metallic arrays which could also support lasing in the visible and NIR. These results highlight the long-range coupling of SLRs through free space, as well as their ability to couple across separate arrays of material. In addition, the highly tunable process flow can be used to generate devices with arbitrary SLR wavelengths and may have applications for multiplexed information transfer or white-light laser sources.

2.8. Methods

2.8.1. Fabrication of NP Arrays

All Au hole mask arrays were fabricated by the PEEL process as follows. Si wafers were treated by Microposit MCC Primer then coated in Shipley 1805 photoresist diluted in PGMEA. Arrays of PR posts were patterned by SANE with DMF and PDMS hole masks molded from periodic Si masters. The PR post arrays were briefly treated with O₂ RIE (≈ 30 s) before a 5-10 nm Cr layer was deposited by thermal evaporation and then lifted off by Microchem Remover 1165. Si holes not masked by the Cr were etched by RIE (55 sccm SF₆, 25 sccm O₂ and 25 sccm Ar at 20 Pa and 70 W). 100-200 nm Au was thermally evaporated onto the Cr/Si holes, which could then be freed from the substrate by wet etching the Cr adhesion layer (Transene Cr Etchant). After floating the Au hole masks onto a new substrate (either quartz or a pre-existing structure with NPs and PR microwrinkles), NPs could be formed by depositing Au, Ag (by thermal evaporation) or Al (by e-beam evaporation). Au and Ag NPs required a thin (2-3 nm) Cr adhesion

layer before deposition.

2.8.2. *Finite-Difference Time-Domain Simulations*

Partially-filled Al NP array simulations were calculated by using a commercially available software (Lumerical). Simulations used a background index of 1.45 (to represent index oil or DMSO on quartz) and a 2 nm mesh applied to each Al NP (material properties from Palik). Simulations used $30 \times 30 \mu\text{m}^2$ regions with perfectly matched layers in $\pm x$, $\pm y$ and $\pm z$ directions. Quasi-periodicity was introduced by binarizing an AFM image of the micro wrinkle mask used in fabrication with a threshold set to achieve the given filling factor. The Al NPs had $a = 400$ nm, thickness of 60 nm and diameter of 90 nm.

2.8.3. *Transmission Measurements*

Transmission spectra and optical band structure of the NP arrays were characterized by collecting the transmitted light ($\lambda = 400\text{-}1000$ nm) that passed through the samples by a spectrometer. For the dispersion diagrams, transmission spectra of the NP array were taken at 1° increments from $\theta = -30\text{-}30^\circ$ and converted into E - k relationship by $E = hc/\lambda$ and $k_{||} = (2\pi/\lambda)\sin\theta$.

2.8.4. *Lasing Measurements*

For each lasing experiment, dye-DMSO solution (concentration and specific dye for each experiment given in main text) was drop cast onto the sample and covered with a glass coverslip. The NP array was pumped by a mode-locked Ti:sapphire laser with regenerative amplifier (fundamental 800-nm wavelength, frequency doubled by BBO crystal for 400 nm experiments, 100 hz operation and 90 fs pulse width). Spot size of the pump was focused to a diameter of approximately 0.5 cm. Lasing signals were collected at surface normal to the sample by a CCD spectrometer.

Chapter 3

Ultrafast Spectroscopy of Plasmonic Titanium Nitride Nanoparticle Lattices

Related publication:

T. Reese, A. Reed, A. Sample, F.F. Fernandez, R. Schaller, A. Urbas, T. W. Odom, “Ultrafast Spectroscopy of Plasmonic Titanium Nitride Nanoparticle Lattices,” *Submitted to ACS Photonics*

3.1. Introduction

Plasmonic nanostructures can manipulate light below the diffraction limit and enable access to optoelectronic architectures thinner than those from dielectric materials.^{1, 6, 8, 120, 131} Surface plasmons can also stimulate photoexcited carriers to modify light absorption at timescales relevant to computer clock speeds (sub-ns), which opens prospects for low-power optical communication.^{6, 75, 91, 132, 133} Although noble metals such as Au and Ag have received the most attention as plasmonic materials, they are generally incompatible with existing semiconductor processing because they have high diffusion coefficients in Si and cause electrical short-circuits.^{134, 135} Titanium nitride (TiN) is a promising plasmonic alternative because of its CMOS compatibility and robustness to high fluences needed for efficient light modulation.^{17, 24, 136-139} Transient absorption (TA) measurements have shown that TiN films and dispersed nanoparticles (NPs) exhibit changes in absorption longer than noble metals at visible wavelengths.¹⁴⁰⁻¹⁴² However, because the plasmonic excitation of NPs partially overlapped with the interband transitions of TiN, the effect of the resonance on the TA features cannot be distinguished;¹⁴⁰⁻¹⁴² the ultrafast transient optical properties of near-infrared (NIR) TiN plasmonic resonances are unknown.

One approach to engineer the wavelength of plasmon resonances is to pattern metal NPs into a periodic array with photonic spacing.^{38, 104, 143} When the refractive index of the superstrate matches that of the substrate, the localized surface plasmons (LSPs) of individual NPs can couple to the diffractive modes of the lattice to form a delocalized plasmonic mode known as a surface lattice resonance (SLR).^{36, 144, 145} Ultrafast studies on noble metal NP arrays have shown that SLRs can trap light orders of magnitude longer than LSPs because of long-range scattering.^{47, 77, 89} Because the decay rates of TiN LSPs are much longer than noble metals, TiN NP arrays are a

model platform to characterize materials effects on the ultrafast properties of collective plasmonic resonances.

In this chapter, we show that different plasmon modes in TiN NP arrays exhibit different transient optical responses. We fabricated single-crystalline TiN NP lattices that supported either LSPs or SLRs at NIR wavelengths by changing the dielectric superstrate. Transient absorption (TA) spectroscopy measurements revealed that LSPs exhibit symmetric resonance broadening while SLRs show asymmetric photo-induced absorption. The transient features of both plasmon types had similar time scales. These trends in absorption were preserved even at high pump fluences, even above the optical damage threshold of noble metals. This work highlights how TiN nanostructures can function as compact optical components that can withstand intense light irradiation

3.2. Fabrication of High-Quality TiN NP Arrays

Figure 3.1a depicts the process flow for fabricating TiN NP lattices from single-crystalline TiN films. First, TiN was epitaxially grown by magnetron-sputtering onto sapphire substrates.¹⁴⁶ We then used solvent assisted nano-embossing (SANE)⁵⁹ to define an array of etch-resistant nanoscale photoresist posts with a desired periodicity (a_0) and radius (r) on the TiN films. The resist features were transferred into TiN films by inductively coupled plasma reactive ion etching (ICP-RIE) with Cl₂ and Ar gases.¹⁴⁷ Although wet etching can rapidly prototype TiN nanostructures of nanoholes,¹⁴⁸ the isotropic etch profiles limit geometric control over NPs and can also etch sapphire. Hence, we used an anisotropic dry etch with Cl₂ plasma that has high selectivity to sapphire in order to minimize etching of the substrate. Finally, any residual resist was

removed by sonicating the sample in photoresist remover solvent. Scanning electron microscopy (SEM) image of a TiN NP array (**Figure 3.1b**) shows that our fabrication procedure can generate NP arrays that are uniform across the 1-cm² sample (Figure 1b, inset). An index-mismatched TiN

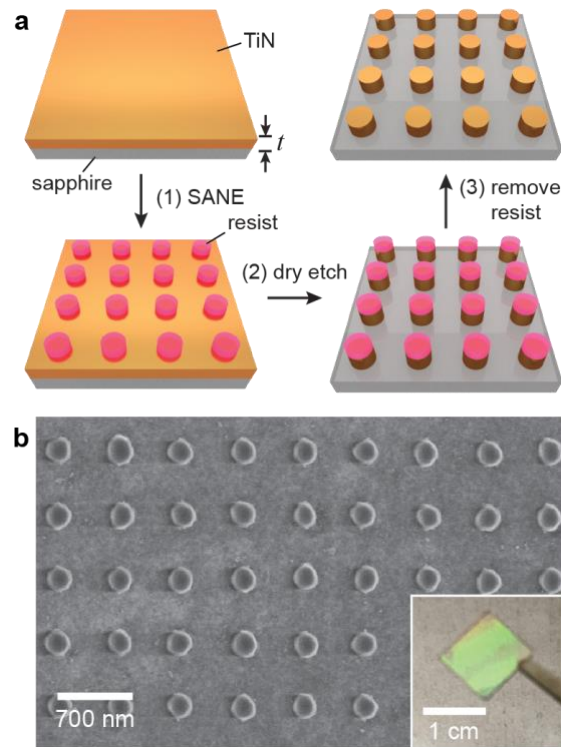


Figure 3.1. Single-crystalline TiN NP lattices by top-down patterning. (a) Scheme of the process flow to generate TiN NP arrays. (b) SEM image of fabricated TiN NP array.

NP lattice with a sapphire substrate ($n \approx 1.75$) and air superstrate ($n = 1$) only supports LSPs; an index-matched environment with a high-index oil superstrate ($n = 1.8$ at $\lambda = 590$ nm) and sapphire substrate supports both SLRs and LSPs, with the LSP at shorter wavelengths.

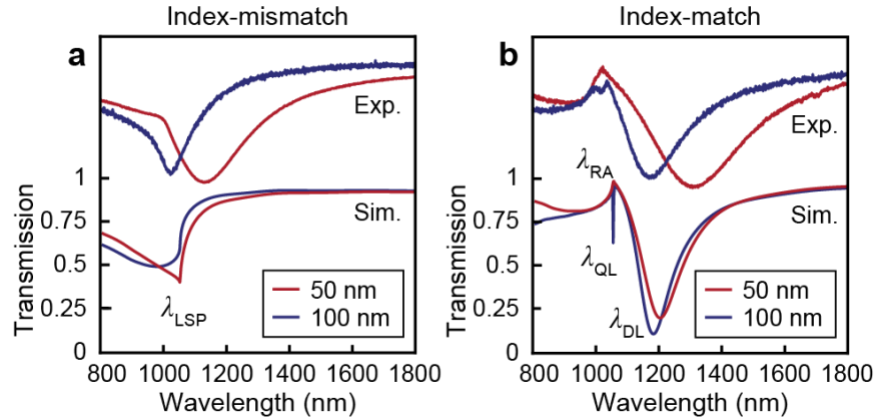


Figure 3.2. NIR plasmonic resonances of TiN NP Arrays. (a) Experimental and simulated transmission spectra of TiN NP arrays in index (a) mismatched and (b) matched environments. Experimental spectra are vertically offset by 0.75. For index mismatched simulations and experiments the substrate (sapphire) had $n = 1.75$ and superstrate (air) had $n = 1.0$.

3.3. Optical Properties of Index-matched and Index-mismatched TiN NP Arrays

3.3.1. Steady-State Transmission Measurements

We measured the steady-state transmission of TiN NP lattices with $a_0 = 600$ nm, $r \approx 100$ nm

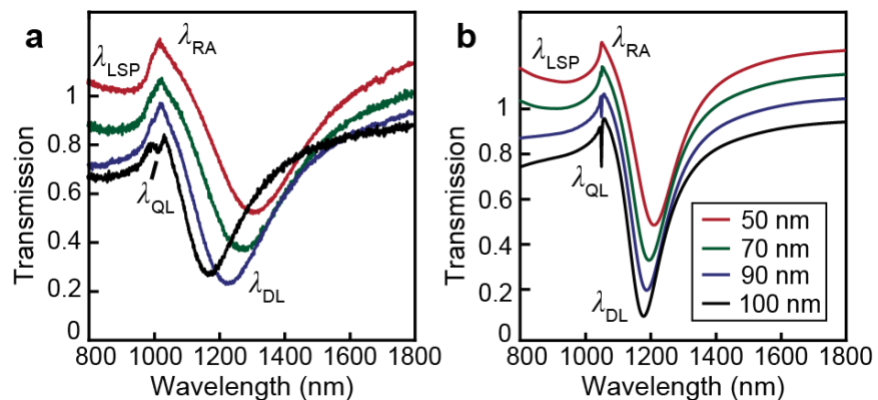


Figure 3.3. Evolution of QL with increased TiN film height. (a) Experimental and (b) simulated transmission spectra for index matched TiN arrays. All samples were fabricated from the same photoresist thickness and PDMS SANE mask. Simulations used $a = 600$ nm and $r = 100$ nm.

and $t = 50$ nm or 100 nm using a UV-vis spectrometer equipped with an integrating sphere. For index-mismatched TiN NPs (**Figure 3.2a**), both NP thicknesses only supported broad resonances. Although finite-difference time-domain (FDTD) simulations of periodic arrays of TiN NPs showed that the LSP wavelength did not change significantly as the NP thickness t increased from 50 nm to 100 nm, experiment showed a blue shift of the LSP from $\lambda = 1125$ nm to $\lambda = 1025$ nm. This blue shift is likely from the slight undercut of the TiN NPs during fabrication. **Figure 3.2b** shows that index-matching the superstrate to the substrate produced spectral features that were distinct from the index-mismatched case. Index-matched TiN arrays with NP thickness $t = 50$ nm only showed a broad SLR ($\lambda = 1310$ nm). In contrast, for $t = 100$ nm NPs, a sharp SLR mode near

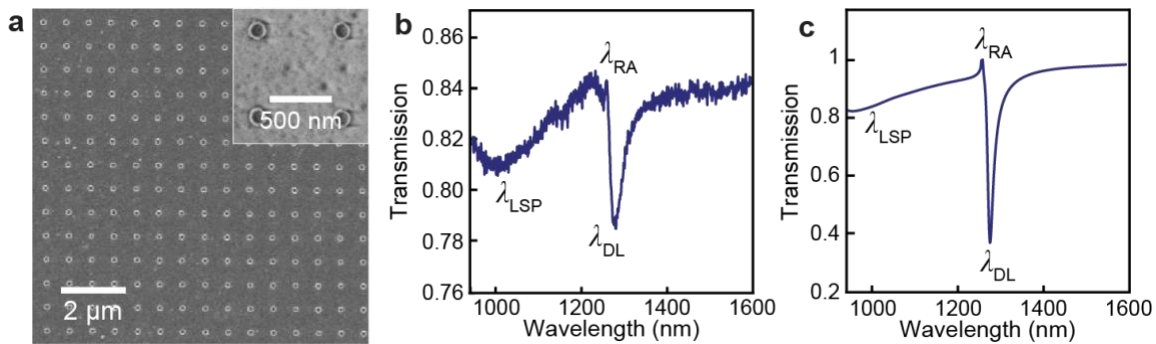


Figure 3.4. Fabrication procedure can generate sharp TiN SLRs in NIR. (a) SEM image showing TiN NP array with $a = 720$ nm and $t = 90$ nm. (b) Transmission spectra measured by UV-vis spectrophotometer. (c) Transmission spectra calculated by FDTD for a TiN NP array with $t = 90$ nm, $a = 720$ nm and $r = 75$ nm.

the Rayleigh anomaly ($\lambda = 1050$ nm) appears in addition to a broad resonance near $\lambda = 1180$ nm. This sharp SLR gradually emerges as the NPs increase in size, as shown in **Figure 3.3**. We could also generate lattices that supported only a single sharp SLR at $\lambda = 1280$ nm by increasing the lattice spacing to $a_0 = 740$ nm, but the experimental dip in transmission was weak (**Figure 3.4**). This result shows that our fabrication procedure can generate TiN NP arrays with smaller NP

dimensions than can be achieved with wet etches. The anisotropic nature of the ICP-RIE etch gives greater control over the geometry of NPs. These smaller NPs can support narrower SLRs due to lower metallic losses.

3.3.2. Nearfield Finite-Difference Time-Domain Simulations

To determine the nature of the SLRs, we calculated electromagnetic near fields and charge distributions of the index-matched TiN arrays. When $t = 50$ nm, the near-field and charge distribution show that the SLR at $\lambda = 1202$ nm is a DL (**Figure 3.5a**). For NPs with $t = 100$ nm, at $\lambda = 1052$ nm, the NPs show a quadrupolar charge distribution (**Figure 3.5b**), which indicates that the sharp feature near the Rayleigh anomaly (RA) is a quadrupolar SLR (QL). QLs can emerge when NPs in an array become sufficiently large so that quadrupolar LSPs are no longer dark modes¹⁴⁹ and can couple to the lattice. **Figure 3.5c** shows that the broad mode at $\lambda = 1180$ nm for $t = 100$ nm is a pure dipolar SLR (DL) with electromagnetic near-field intensities similar to the QL.

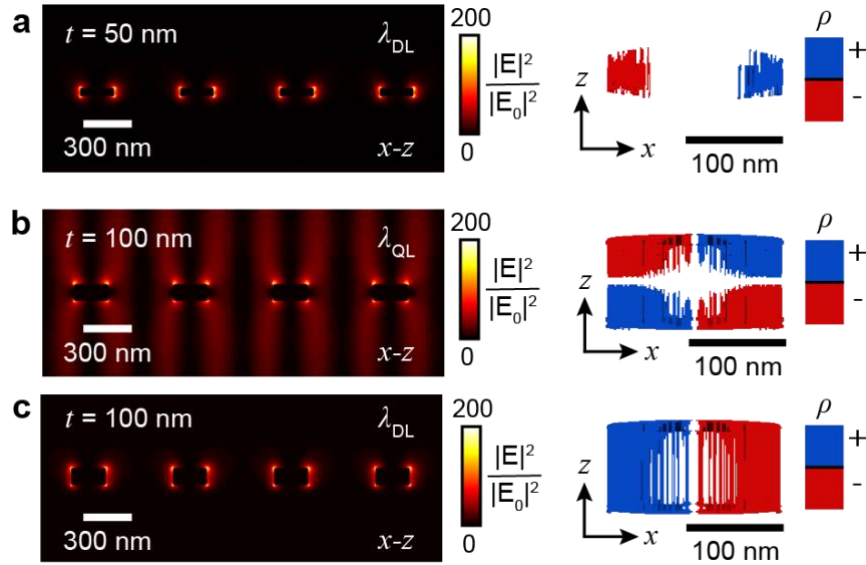


Figure 3.5. Fabrication procedure can generate sharp TiN SLRs in NIR. Simulated nearfield and charge density for (a) $\lambda_{DL} = 1202$ nm with $t = 50$ nm and (b) $\lambda_{QL} = 1052$ nm and (c) $\lambda_{DL} = 1180$ nm with $t = 100$ nm. Dimensions for all near-field calculations are $a_0 = 600$ nm, $r = 100$ nm. For index mismatched simulations and experiments the substrate (sapphire) had $n = 1.75$ and superstrate (air) had $n = 1.0$.

3.4. Transient Absorption Spectroscopy of TiN LSPs and SLRs

3.4.1. Index-Matched and Index-Mismatched TiN NPs at Ultrafast Timescales

We probed the effect of LSPs, QLs, and DLs on the ultrafast photoinduced properties of TiN NP lattices by fs-transient absorption (TA) spectroscopy. NP lattices were pumped with a pulsed Ti: sapphire laser at 800 nm and probed with broadband NIR light as a function of delay time from 0-1000 ps. We compared index-mismatched TiN arrays with $t = 50$ nm NPs and LSP wavelength at $\lambda = 1125$ nm and index-matched arrays with $t = 100$ nm NPs and DL wavelength at $\lambda = 1170$ nm because their resonance wavelengths were similar (**Figure 3.6**). **Figures 3.6a-b** show that the LSP supports a ground state bleach near $\lambda = 1125$ nm that reaches a minimum of $\Delta A \approx -20$ mOD in approximately 500 fs under a modest fluence of 1.5 mJ/cm². This decrease in absorption is from

the depletion of photoexcited carriers in the TiN NPs at the LSP. After the initial plasmon dephasing, electron-electron scattering causes changes in absorption to decrease in magnitude. The bleach persisted for over 1 ns, which is similar in time scale to lattice cooling in TiN films at visible wavelengths.¹⁴² Weak and symmetric photoinduced absorption on the shoulders around the bleach feature indicate that the LSP broadens at ultrafast timescales from NP heating.^{90, 91, 150}

To study the transient features associated with SLRs, we measured the time-resolved spectra of the index-matched $t = 100$ nm TiN NP array, which supports both DL and QL resonances under

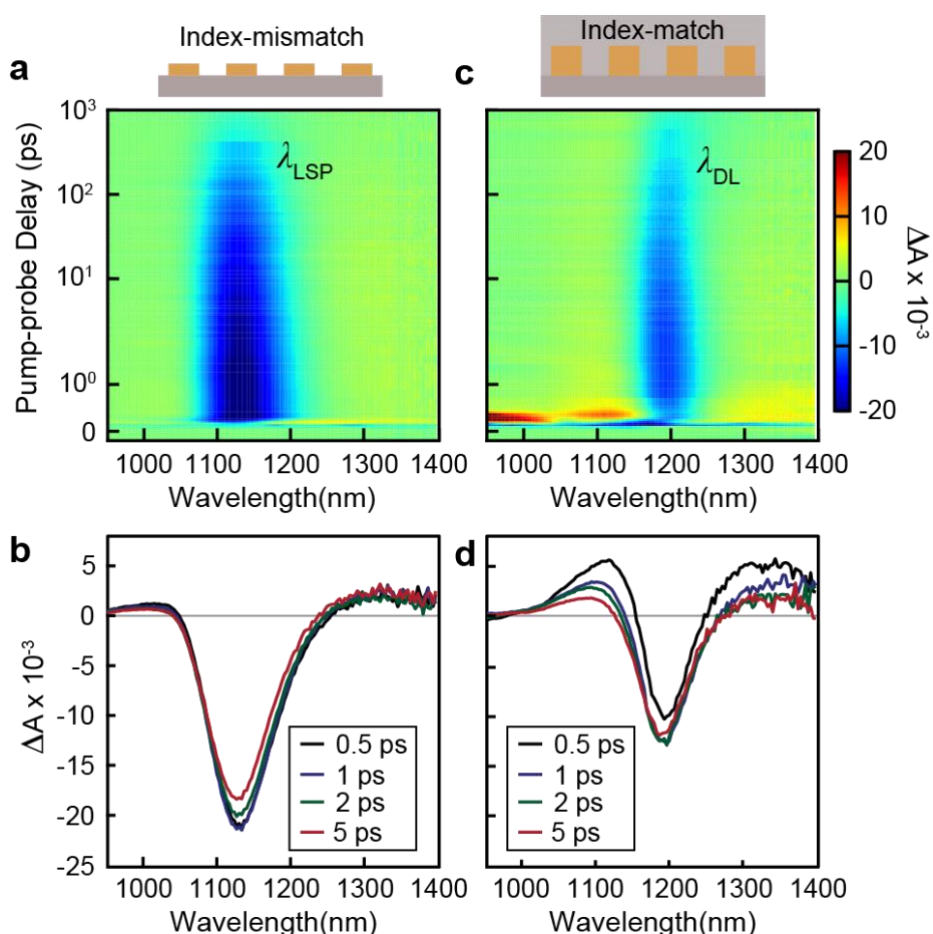


Figure 3.6. Plasmon mode alters ultrafast absorption line shape. TA spectral maps (a, c) and time slices of TA data (b, d) for a TiN NP arrays with (a-b) $t = 50$ nm in air and (c-d) $t = 100$ nm in index oil. Samples were pumped with 800 nm light at 1.5 mJ/cm² fluence.

steady-state conditions. The bleach near 1200 nm corresponds to the DL, which decayed over 1 ns, similar to the LSP response (**Figures 3.6c-d**). The TA spectra of the index-matched NP lattice displayed asymmetric absorption, with shorter broadening at wavelengths bluer than the DL. This absorption profile is due to the asymmetric Fano resonance line shape of SLRs in the steady state.

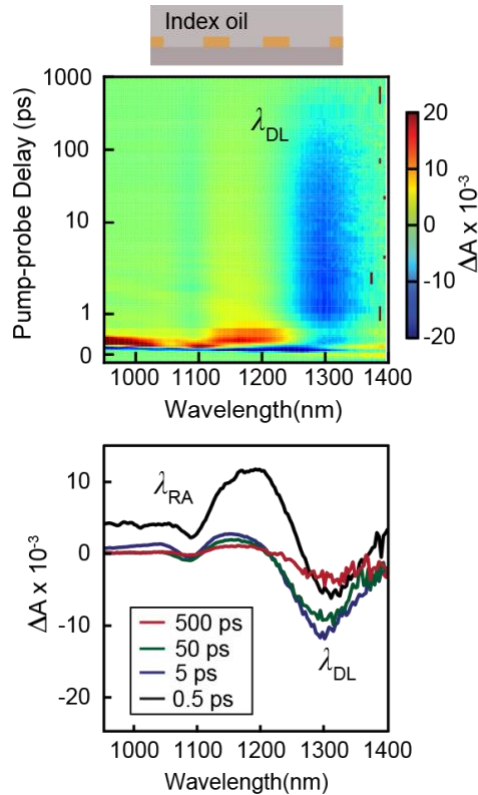


Figure 3.7. TA of index-matched TiN NP array with $t = 50$ nm. TA spectral map and time slices of TA data for a TiN NP arrays with $t = 50$ nm in index oil. Sample was pumped with 800 nm light at 1.5 mJ/cm^2 fluence.

Despite having a narrower resonance than the DL and similar calculated electric field enhancements, the QL at $\lambda = 1020$ nm showed no discernable features in the transient spectra.

To confirm that these transient features were not from the Rayleigh anomaly, we performed TA on the index-matched $t = 50$ nm TiN NP array. **Figure 3.7** shows that the large induced absorption on the blue side of the DL bleach signal ($\lambda = 1150\text{-}1200$ nm) follows the DL near $\lambda =$

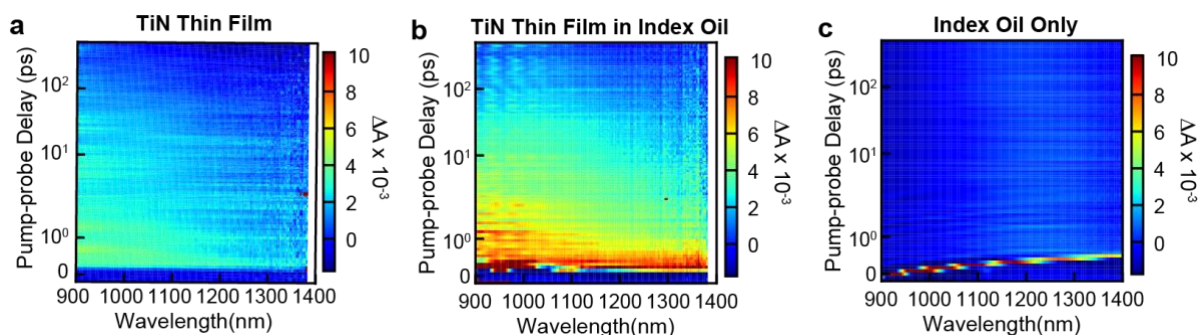


Figure 3.8. Transmission Absorption Spectra of TiN films. TiN thin film with thickness of approximately 15 nm in (a) air and (b) index fluid $n = 1.8$. (c) TA spectra of only index oil on sapphire.

1300 nm instead of the Rayleigh anomaly near $\lambda = 1050$ nm. This result indicates that the ultrafast asymmetric absorption is due to the DL resonance and not a feature related to the Rayleigh anomaly.

3.4.2. Transient Absorption of TiN Thin Films

High photo-induced absorption at early time points (< 5 ps) for the index-matched array can be partially attributed to the properties of the index oil (**Figure 3.8**). **Figure 3.8a** shows the transient absorption of TiN thin films grown on sapphire have a broadband absorption that decays over several hundred ps, which is similar in timescale to the LSP and DL bleaches. The transient profile of the TiN thin film coated in index oil (**Figure 3.8b**) looks similar to the as-grown sample, but has a large and broadband photoinduced absorption that decays within the first several hundred femtoseconds. This elevated but rapidly decaying absorption caused by the interaction of the index oil with TiN may partially account for the large induced absorption seen at early time points for the index-matched samples in figures 3.6-3.7. **Figure 3.8c** shows that the index oil has no transient features beyond 1 ps.

3.4.3. Transient Response at High Pump Fluences

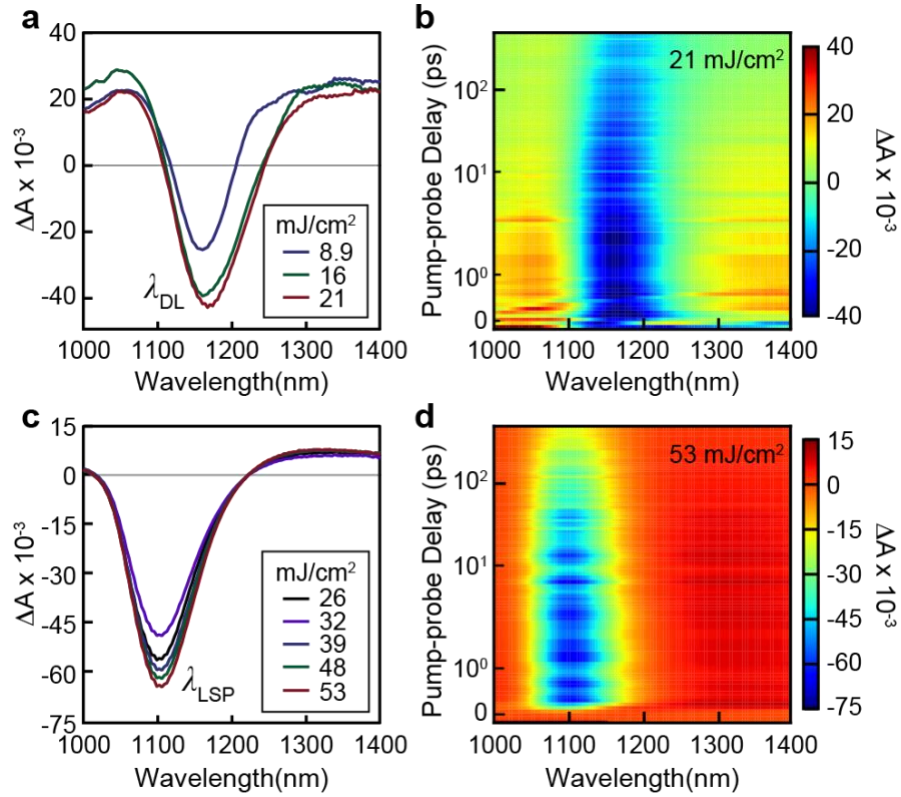


Figure 3.9. TiN NP arrays under extreme pump irradiation. (a) TA spectra taken at 542 fs for irradiance with high pump powers for index-matched $t = 100$ nm TiN NP arrays. (b) TA spectral maps for pump at 21 mJ/cm^2 . (c) TA spectra taken at 250 fs for irradiance with high pump powers for $t = 50$ nm TiN NP arrays in air. (d) TA spectral maps for pump at 53 mJ/cm^2 .

Also, we tested the robustness of TiN DLs under intense laser irradiation. Sweeping the pump fluence from 8.9 mJ/cm^2 to 21 mJ/cm^2 (Figures 3.9a-b), we found that the asymmetric absorption at wavelengths shorter than the DL persisted at elevated fluences. The transient features shifted to shorter wavelengths compared to the spectra in Figures 3c-d because the refractive index n of the oil decreases with increased temperatures from absorption at high pump powers.¹⁵¹

Furthermore, we probed the ultrafast characteristics of the index-mismatched TiN NP array at pump fluences higher than the degradation point of the index oil. Figure 3.9c shows that the bleach

and induced absorption wings of the LSP are maintained even under extremely high fluences. The TA response at 53 mJ/cm² shows a significant bleach $\Delta A \approx -65$ mOD that remains present over 500 ps (**Figure 3.9d**); notably, this decay time is similar to that measured at 1.5 mJ/cm² (Figure 3a) and suggests that TiN NPs maintain structural integrity. Although ΔA did not increase linearly with fluence at high pump powers, the bleach intensity continued to increase through 50 mJ/cm².

The pump powers used in these experiments are significantly larger than are what are capable for noble metal NPs. For example, the saturation fluence of colloidal Au NPs is 2-3 orders of magnitude lower than we observed for TiN NPs.⁹² Typically, Au NPs are measured by fluences on the order of hundreds of $\mu\text{J/pulse}$ ^{90,91,152} while Ag NPs have been shown to aggregate at pump powers of 2-5 mJ/pulse.¹⁵³ We note that these studies cannot be compared directly due to their lack of reported spot size and differences in absorbed heat because of pump wavelength and NP resonance absorption, but serve as a useful comparison. Therefore, TiN NPs may be useful for applications or fundamental studies that require extremely high pump fluences due to low gain efficiency.

3.5. Probing Effect of Environment and Pump Energy on Ultrafast Properties of TiN NP Arrays

3.5.1. Tuning Environment to Determine Solvation

Index-matched samples show a slight red shift of the bleach feature at long (> 1 ns) timescales. To determine if this change was from a characteristic of SLRs or the presence of index fluid, we measured TiN NP arrays in additional liquids. **Figure 3.10** shows that a wide variety of solvents show this red shift despite non-index matched conditions. This red shifting is likely due to

solvation.^{93, 154-156} In addition, many of these solvents show asymmetric TA profiles which are similar but less broad and pronounced than the index matched experiments.

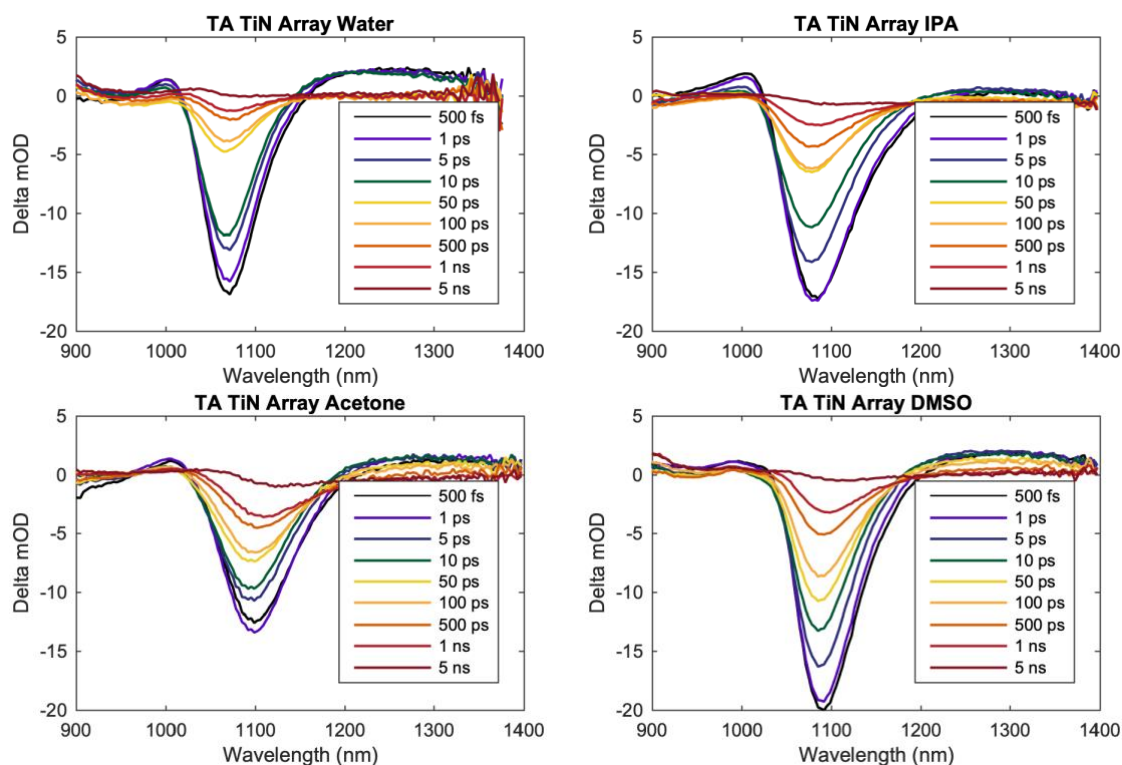


Figure 3.10. TiN NP arrays in low-index solvents. TA spectra taken TiN NP arrays in water ($n = 1.333$), IPA ($n = 1.376$), acetone ($n = 1.395$) and DMSO ($n = 1.479$). Samples were pumped at 2.8 mJ/cm^2 with $\lambda = 800 \text{ nm}$.

We attempted to generate samples that were index-matched through e-beam deposition of Al_2O_3 in order to realize a solid-state uniform dielectric environment. **Figure 3.11a** shows a transmission spectra TiN NP array with $a = 650 \text{ nm}$ in air, in $n = 1.8$ index oil and after approximately 300 nm of Al_2O_3 deposition. The lack of a Rayleigh anomaly in the Al_2O_3 spectra indicates the deposition is insufficient in establishing an index-matched superstrate. In addition, the Al_2O_3 coated sample shows a second resonance appears at shorter wavelengths, which is likely a waveguiding hybrid mode. Because the Al_2O_3 resonance near 1150 nm is blue shifted from the

SLR of the index-matched sample, the Al_2O_3 film likely has a lower refractive index than sapphire due to pockets lower density. The lower density may have been caused by air pockets during deposition. We observe only a weak bleach feature for the index matched case due to a poor LSP (Figure 3.11b). Figure 3.11c shows that the Al_2O_3 deposited sample shows bleach features at both resonances seen in the steady state transmission spectra. The bleach does not appear to shift at longer time delays (> 1 ns), which supports our previous assertion that the red shift is due to solvation. Surprisingly, the Al_2O_3 coated sample shows minimal induced absorption, which

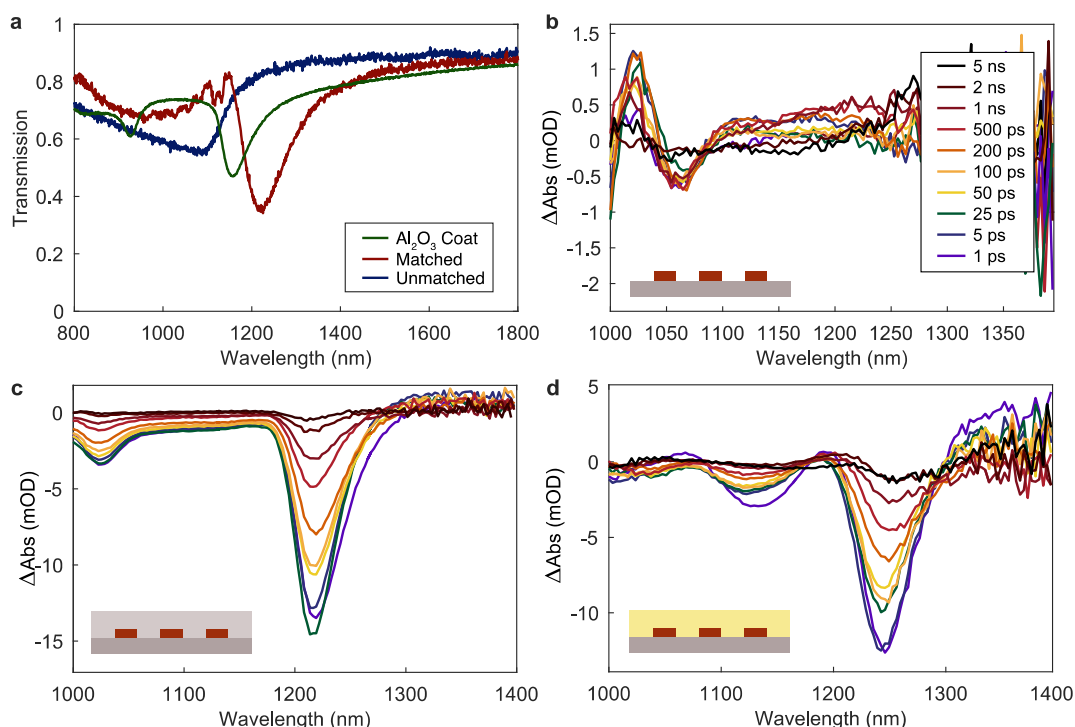


Figure 3.11. TiN NP arrays in gas, solid and liquid. (a) Transmission spectra comparing a TiN NP array in air, 300 nm of Al_2O_3 and $n = 1.8$ index oil. Accompanying TA spectra for the TiN NP array in (b) air, (c) 300 nm of Al_2O_3 and (d) $n = 1.8$ index oil.

suggests low plasmonic broadening. Figure 3.11d shows an asymmetric profile that red-shifts at long time delays, which is consistent with experiments using $a = 600$ nm TiN NP arrays.

3.5.2. Sweeping Pump Energy

To determine if the energy of the pump had a significant effect on the transient response of TiN nanostructures, we pumped the TiN NP arrays with wavelengths in the UV, visible and NIR. **Figure 3.12** shows that pump energy has minimal effect on the resonant wavelength, width and decay time. The wavelengths were chosen to probe specific material properties of TiN and optical features of this NP array. $\lambda = 325$ nm has enough energy to pump above the band gap of TiN (3.4 eV). $\lambda = 400$ nm is lower energy than the band gap, but above what has been reported as the cutoff energy.^{17, 157} $\lambda = 800$ nm is below the cutoff energy, but higher than the LSP wavelength of this sample. $\lambda = 1050$ nm is approximately the same energy as the LSP. $\lambda = 1200$ nm is lower energy than the LSP. $\lambda = 1500$ nm is lower than any transitions predicted by TiN band diagrams.¹⁵⁷ These results show that electronic excitation has little effect on the transient features of TiN NP arrays, and the relaxation is likely dominated by thermal effects.

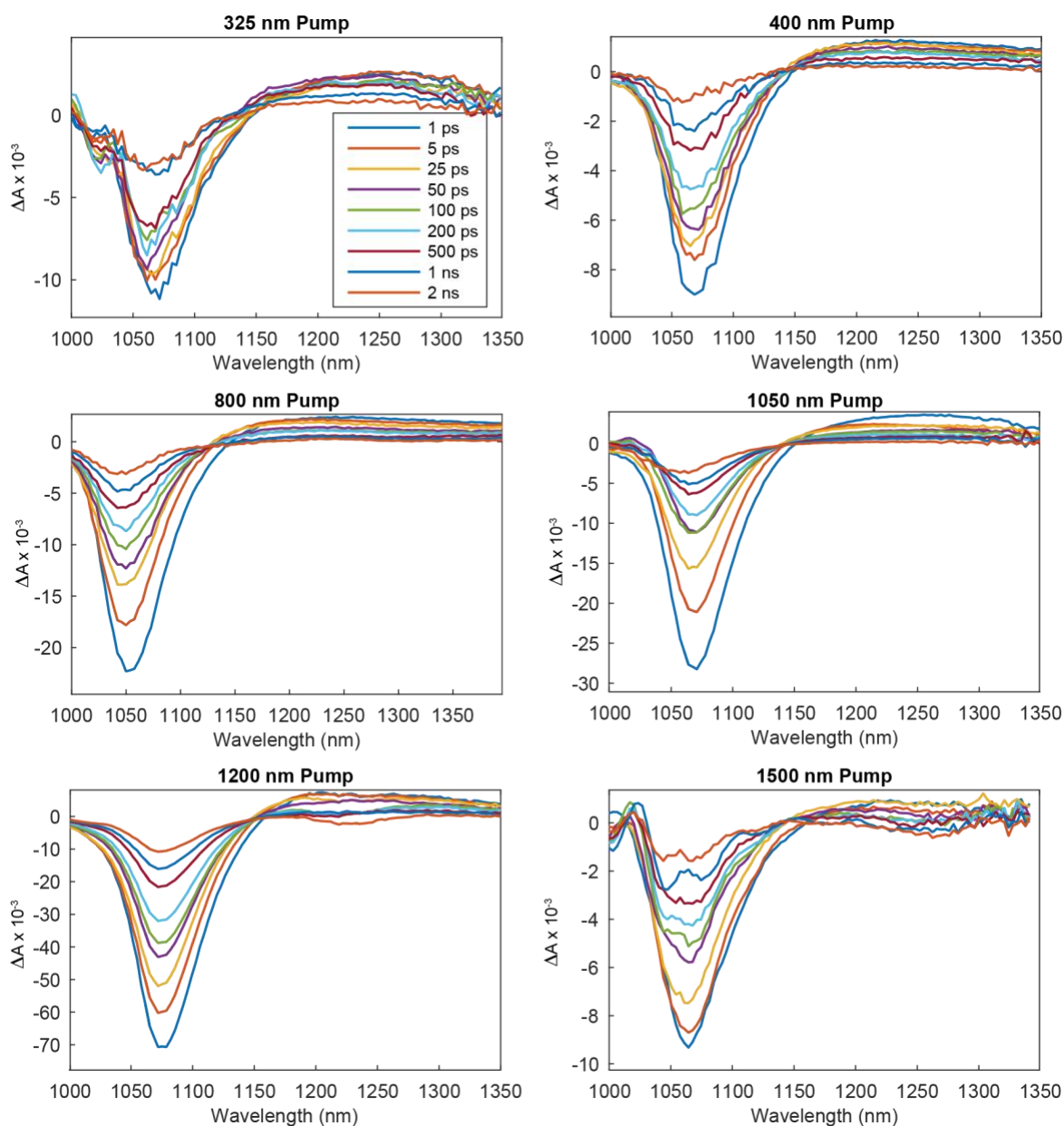


Figure 3.12. TiN NP array pumped by different energies. TA spectra for a TiN NP array with $a = 600$ nm, $t = 90$ nm pumped at $\lambda = 325$ nm, 400 nm, 800 nm, 1050 nm, 1200 nm and 1500 nm. All spectra have had background subtracted.

3.6. Introduction to Multi-layer Plasmonics

There is growing interest in stacks of alternating metallic and insulator thin film layers because

they can be used to generate hyperbolic metamaterials (HMMs).¹⁵⁸⁻¹⁶⁰ Previous examples have used alternating layers of noble metals and SiO₂ deposited by evaporation, which can have large grain sizes and high surface roughness. Materials that can be grown epitaxially, such as TiN, have the advantage of single crystallinity with low surface roughness. AlN, a wideband gap semiconductor ($E_{bg} = 6.2$ eV) with a relatively large refractive index ($n = 2.1$), can be deposited through similar methods to TiN but is a dielectric material with low losses in the UV and visible regime.^{161, 162} AlN and TiN superlattices can be formed with ultrathin (~ 2 nm) alternating layers so they represent an ideal tandem for multi-layer plasmonic nanostructures.¹⁶³ Most experimental results of multi-layer devices have focused on films, but the high electric field intensities that can be supported by SLRs through periodic arrays may further increase the exotic optical phenomena of multi-layer structures.

3.7. Fabrication of Metal-Insulator NPs from High-Quality TiN/AlN Thin Films

Before attempting to fabricate TiN/AlN stacks consisting of many layers, we began by fabricating arrays of NPs from of a single TiN layer grown on a sapphire substrate followed by AlN grown on TiN. As previously discussed, the robust properties of TiN make nanofabrication difficult to achieve through wet-etching methods. AlN has an even slower etch rate than TiN,¹⁶⁴ so thicker stacks of TiN and AlN require a hard mask instead of the PR soft mask we used to fabricate TiN NP arrays. SiO₂ is a typical material used as for etch hard masks, but the ICP-RIE recipes necessary to etch AlN have low selectivity to SiO₂ (~ 0.5 - 2 : 1 AlN:SiO₂).¹⁶⁴ Cu is not etched by this ICP-RIE process (at temperatures lower than 200°C),^{68, 165} and it can be removed by acetic acid, which does not corrode AlN, TiN or sapphire. **Figure 3.13** shows our process flow

for fabricating arrays of TiN/AlN NPs. First, we fabricate an Au hole mask through the PEEL process. This Au hole mask is floated on top of the TiN/AlN films and approximately 30 nm of Cu is deposited onto each sample. The Au hole mask is removed by tape. Then, we use an ICP-

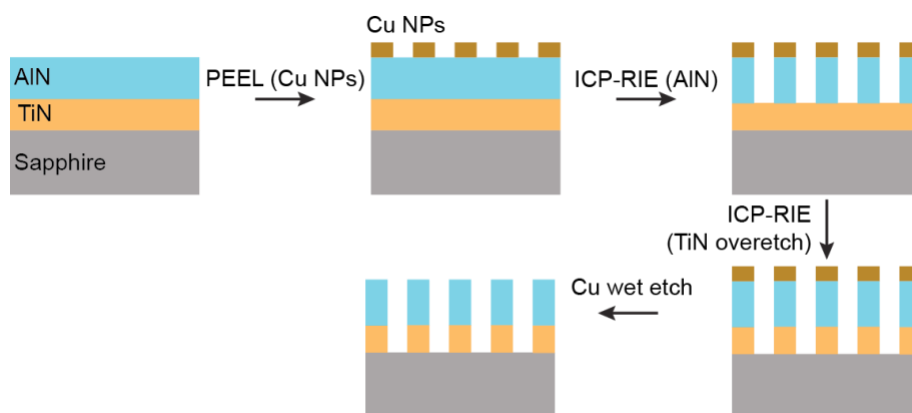


Figure 3.13. Process flow for fabricating TiN/AlN NP arrays. Scheme depicting the use of a Cu nanodisks to mask the TiN/AlN films during a two-step ICP-RIE etch.

RIE recipe using Cl_2 , BCl_3 and Ar gases. BCl_3 can etch TiN and sapphire, so we added a second etch step without BCl_3 to prevent over-etching into the substrate. We followed the ICP-RIE etches with a Cu wet etch to remove the Cu hard mask.

Figure 3.14a shows the 30 nm thick Cu NP hard mask deposited on the TiN/AlN stack. Cu disks have $a = 600$ nm and are relatively even in diameter (≈ 250 nm). **Figure 3.14b-c** show Cu NPs on TiN/AlN NPs after both ICP-RIE etch steps but before Cu wet etch. The AFM image (**Figure 3.14b**) indicates that the top of the NPs is rough, and the low height of the NPs suggests that either the TiN/AlN layers are not completely cleared or there is Cu reposition. The charging seen in the SEM image (**Figure 3.14c**) implies that no continuous conductive layer remains, so the TiN has been fully etched and the sapphire substrate is exposed. **Figure 3.14d** shows that after the Cu wet etch, much taller NPs with flat tops emerge. This result suggests there was significant Cu deposition during ICP-RIE. The imperfections in the lattice are due to defects in the Au hole mask

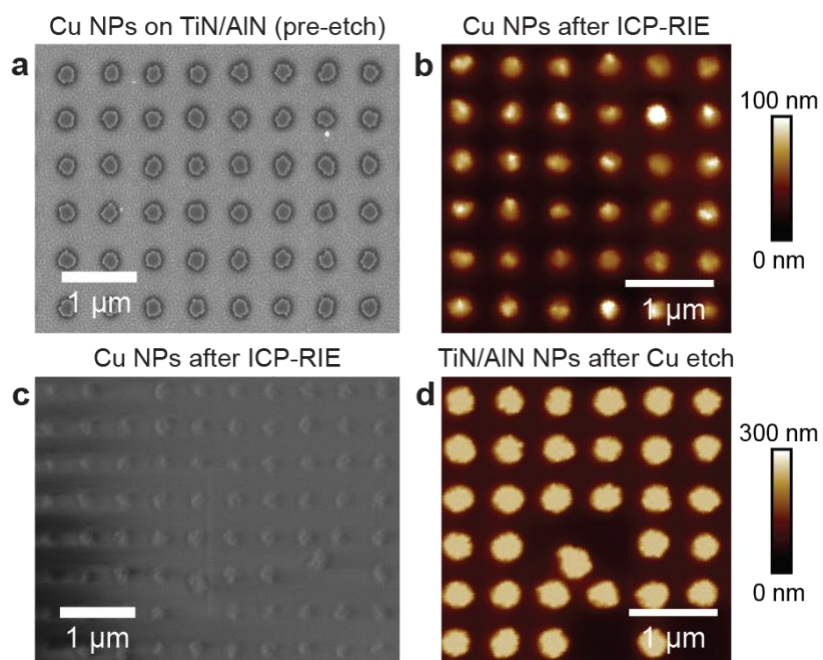


Figure 3.14. Fabrication of TiN/AlN NP arrays. (a) SEM image of Cu NPs deposited through hole mask on TiN/AlN films. (b) AFM and (c) SEM image of sample after ICP-RIE but before Cu removal. (d) AFM image of sample after Cu removal.

(from the original PDMS mold) and are unrelated to the TiN/AlN NP array fabrication procedure.

3.8. Optical Properties of TiN/AlN NP Arrays

3.8.1. Steady-State Transmission Measurements

After generating arrays of TiN/AlN NPs, we sought to characterize their optical properties. We began by using a similar measurement setup to evaluate the steady-state transmission spectra as was used for the TiN NPs in Chapter 3.2. **Figure 3.15** shows that index-matched and index-mismatched arrays of TiN NPs support similar NIR plasmonic resonances to their purely TiN counterpart. However, these resonances are redshifted due to the presence of the high-index AlN ($n = 2.1$) on top of the TiN. The resonances are strong but broad. Both index-matched and index-mismatched experimental spectra (solid lines) have good agreement with simulations (dashed lines) of their structure. Although neither Rayleigh anomaly is as sharp as the index-matched TiN NP arrays, index-matched and index-mismatched TiN/AlN NPs show a slight peak, which suggests

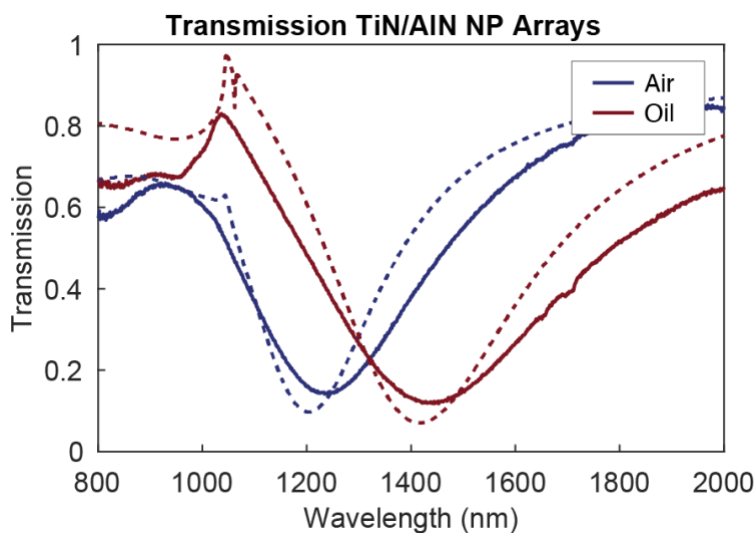


Figure 3.15. Transmission spectra of TiN/AlN NP array.

they may both support SLRs. The AlN may mediate this response by increasing the average local refractive index near the TiN NPs.

3.8.2. Transient Absorption of TiN/AlN NP Arrays

The AlN/TiN NP arrays that we fabricated shown in **Figure 3.15** have static transmission spectra that agreed well with our FDTD simulations, which treated AlN as a pure dielectric material. However, because AlN is a semiconductor with large non-linear properties, we were interested to see if the ultrafast response of AlN/TiN arrays would differ from TiN arrays with similar dimensions. To evaluate the effect of AlN on the ultrafast properties of TiN/AlN NP arrays, we measured the sample shown in **Figure 3.15** with transient absorption spectroscopy. **Figure**

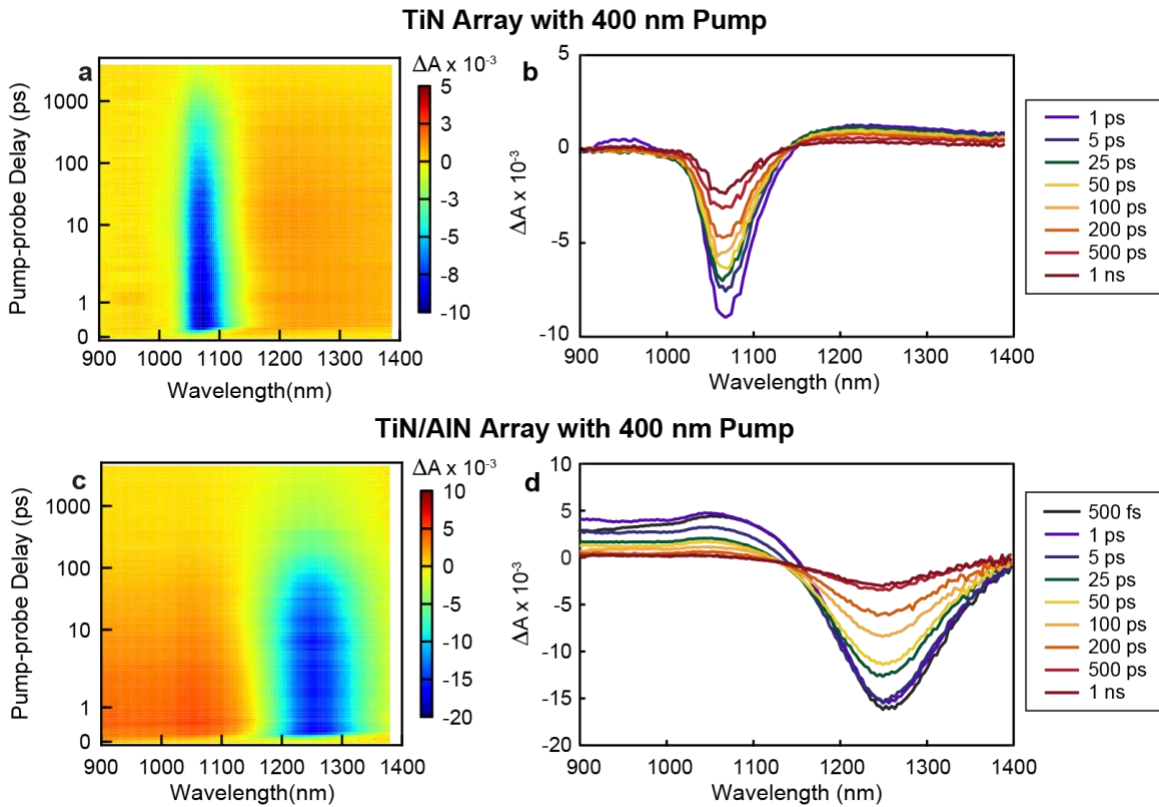


Figure 3.16. Transient absorption spectra comparing TiN and TiN/AlN NP arrays. (a) TA spectral surface **(b)** delay spectra for a TiN NP array with $a = 600$ nm. **(c)** TA spectral surface **(d)** delay spectra for a TiN/AlN NP array with $a = 600$ nm. Both samples pumped by $\lambda = 800$ nm with air superstrate.

3.16a shows TiN and TiN/AlN NP arrays (index-mismatched with air superstrate) pumped with $\lambda = 400$ nm femtosecond laser source and measured in the NIR regime. For the bare TiN array, we

observe minimal photoinduced absorption (**Figure 3.16a-b**), but **Figure 3.16c-d** shows that the AlN has a profound effect on the photoinduced absorption on the blue side of the bleach feature. The TiN/AlN array shows broadband induced absorption with approximately 50% the magnitude of the bleach. This result suggests that the photoexcited carriers in the TiN NPs are injected into the AlN.

3.9. Future Works: Transition-Metal Nitrides for Visible Regime

3.9.1. Introduction to Zirconium Nitride

ZrN has a lower dielectric-plasmonic crossover wavelength than TiN, which allows us to

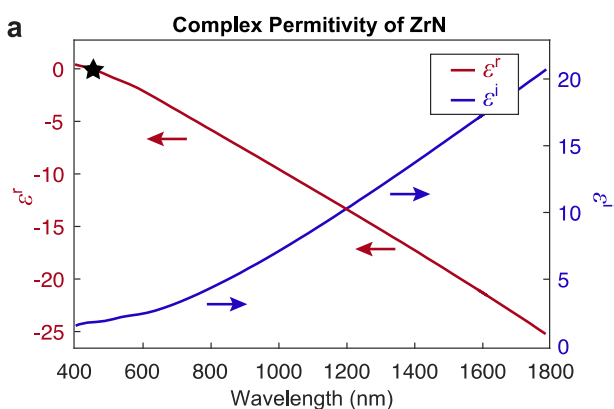


Figure 3.17. Measured Optical Properties of Transition-metal Nitrides. (a) Real and Imaginary permittivity values for Zirconium nitride. Stars indicate transition from metallic to dielectric.

access additional wavelength regimes while maintaining the same physical and chemical advantages of TiN.^{142, 166, 167} As shown by the plot in **Figure 3.17**, ZrN exhibits a dielectric-metallic transition in the optical properties at approximately $\lambda = 520$ nm, slightly bluer than TiN, which may cause ZrN nanostructures to support plasmonic resonances in the visible regime.

3.9.2. Optical Simulations of ZrN NP Arrays

We used finite-difference time-domain (FDTD) simulations to calculate the farfield

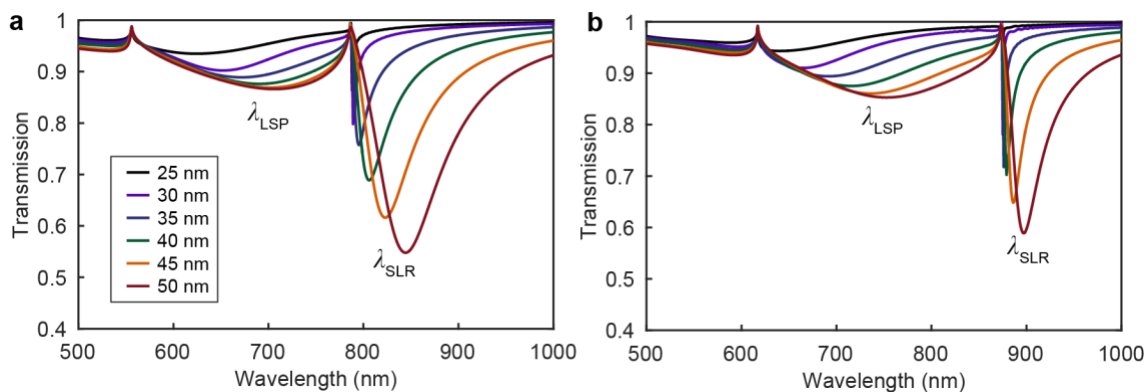


Figure 3.18. FDTD simulated radii sweep of ZrN NP arrays. Transmission spectra for index match ZrN NP arrays with period (a) 450 nm and (b) 500 nm. Radius was swept from 20-50 nm. All NPs used $t = 50$ nm

transmission spectra of an infinite array of ZrN NPs to find optimal dimensions for exciting sharp surface lattice resonances (SLRs) with high quality factors in the visible or near infrared (NIR). permittivity values for ZrN were taken from literature¹⁶⁶ and loaded into the FDTD material library. The simulation region was set to a homogenous background index $n = 1.75$ to simulate a dielectric environment with ZrN NPs on a sapphire substrate with an index matched superstrate (by index fluid). **Figure 3.18** shows that ZrN NPs are able to support LSPs in the visible, but they are broad, which indicates a low quality factor. However, at wavelengths redder than 800 nm, we can excite SLRs. In Figure 1a, sharp SLRs are observed with $r = 25$ -30 nm, which may be difficult to fabricate due to small feature sizes. Additionally, the sharp SLRs for $a = 450$ nm show weak dips that may not be discernable from the noise level of the instrument. The simulations with $a = 500$ nm shown in **Figure 3.18b** contain sharper and stronger SLRs, but at wavelengths near 870 nm. This periodicity supports sharp SLRs up to $r = 40$ nm, which will be easier to fabricate. We were unable to observe sharp SLRs for TiN NP arrays below 1000 nm, so ZrN provides a pathway to reduce the wavelength of high-quality SLRs by over 100 nm.

3.9.3. ZrN NP Array Fabrication

In order to pattern the ZrN films, we adapted the process flow from Figure 3.13 for

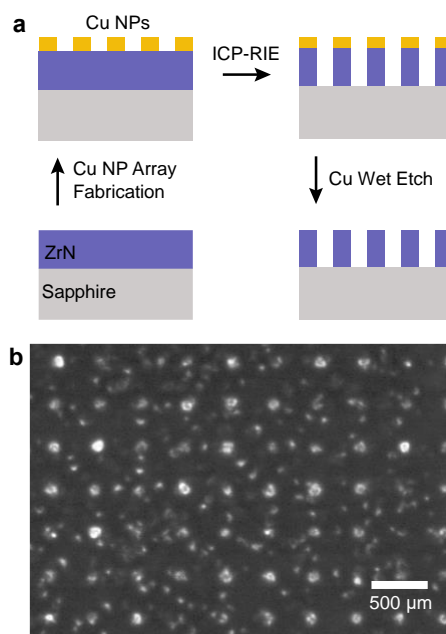


Figure 3.19. Fabricating ZrN nanostructures. (a) Process flow for transferring NP array into ZrN thin films. (b) SEM image of fabricated ZrN array

AlN/TiN film stacks (**3.19a**). Briefly, Cu discs were deposited through Au hole masks that had been floated onto ZrN films grown on sapphire. The Cu hard mask was transferred into the ZrN thin film by Cl_2 -based inductively coupled plasma reactive ion etch (ICP-RIE). Our recipe used 15 sccm Cl_2 , 5 sccm BCl_3 and 10 sccm Ar with a pressure of 10 mTorr and bias and RF powers set to 65 W and 700 W respectively. The Cu mask was then removed by a wet chemical etch. **Figure 3.19b** shows that our procedure for generating ZrN NP arrays is able to achieve distinct posts in a square array geometry. However, there are small features that we attribute to the high nano-crystallinity and surface roughness of the initial ZrN films. These films were grown during early optimization of the deposition conditions and future films will be of higher quality.

3.10. Conclusions

In summary, we measured transient optical properties of TiN NP lattices at NIR wavelengths and found photo-induced responses characteristic of different classes of plasmon modes. Single-crystalline TiN NP arrays supported either broad LSPs or sharp SLRs depending on the refractive index of the superstrate. Although both QL and DL SLRs showed high local field enhancements, these near-field intensities were not necessarily correlated with measurable ground state bleach signals. We extended production to additional transition metal nitrides and found the dielectric character could have profound effect on the induced absorption properties. Our results indicate how TiN NP arrays may function as CMOS-compatible building units for optoelectronic applications that require ultrafast light modulation and high intensity irradiation.

3.11. Methods

3.11.1. TiN NP Array Fabrication

Photoresist (Shipley 1805 1:8 ratio of photoresist to PGMEA solvent) was spun onto TiN films to a thickness of 200 nm. The photoresist was patterned into an array of polymer posts by solvent-assisted nanoembossing (SANE).⁵⁹ SANE molds polymers by dipping PDMS masks with predefined features (periodic nanohole arrays) into a solvent (DMF) that can dissolve a given polymer and placing it on the polymer thin film. The resist posts were transferred directly into the TiN film by an inductively coupled plasma reactive ion etch (Plasma-Therm ICP-RIE Chlorine Etch System). A gas mixture of 84 sccm Ar and 36 sccm Cl₂ was flowed into the chamber at a pressure of 1.1 Pa and temperature of 20 °C. The plasma was ignited at a RF coil power of 500 W and a RF bias power of 85 W. Samples were etched between 10-20 s depending on TiN film

thickness. After etching, samples were placed in solvent (Microposit photoresist remover 1165) and sonicated for several minutes to remove residual resist.

3.11.2. TiN Film Growth

The single-crystal TiN films were grown by controllably unbalanced reactive magnetron sputtering. During deposition, the chamber was pumped to a low vacuum (pressure $P = 0.02$ Torr, 1:1 $N_2:Ar$). By using a 100 W target power, the process achieved a growth rate of approximately 0.1 nm/s. The average temperature of the substrate was approximately 600 C° during epitaxial growth.

3.11.3. Steady-State Optical Measurement

Transmission spectra of TiN NP lattices were measured by a Cary 5000 UV-vis spectrophotometer with a DRA-2500 integrating sphere module (Agilent Technologies, Santa Clara, CA). We used a 1-nm slit band width and data interval for 400-2000 nm spectral range. For the index-mismatched experiments, the TiN NP arrays were taped to a glass cover slip with the NPs exposed to air. For the index-matched experiments, a drop of index fluid (Cargille Laboratories, M Series, $n = 1.8$) was sandwiched between the TiN NP arrays and a glass cover slip.

3.11.4. Finite-Difference Time-Domain Simulations

FDTD calculations based on commercial software (FDTD Solution, Lumerical Inc., Vancouver, Canada) were used to simulate the far-field and near-field properties of TiN NP lattices. Optical constants of TiN were taken from ellipsometry measurements¹⁴⁸ and imported to the materials database of Lumerical FDTD. A uniform $2 \times 2 \times 2$ nm³ mesh was placed around the NPs. Boundary conditions in $\pm x$ and y planes were set to periodic while $\pm z$ planes used a perfectly matched layer with 8 layers. Near-fields were captured by frequency domain time profile monitors.

Charge distributions were calculated by taking the curl of 3D electric near-fields and index of the TiN NPs and visualized using open-source software (Paraview, Copyright (c) 2005-2017 National Technology & Engineering Solutions of Sandia, LLC (NTESS), Kitware Inc.).

3.11.5. Transient Absorption (TA) Measurements

A Ti: sapphire laser that produced 35-fs pulses at 1 kHz was used for TA measurement. The 800 nm output was split into two beams; one beam was directed at the sample for the excitation pulse, and the other beam was focused into a sapphire crystal to generate a white-light-continuum probe pulse. All samples were excited with a beam diameter between 500 μm and 1 mm. TA absorption spectra were measured using a CMOS-spectrometer set normal to the surface of the sample. With these spectra, the absorbance difference (ΔA) was plotted as a function of pump-probe delay time from 0 to 1 ns. The pump was unpolarized by a depolarization optic, and the probe had no polarization selection. For the index-mismatched experiments, the TiN samples were taped to a cover glass so that the TiN NPs were exposed to air. For the index-matched experiments, the TiN samples were placed in a quartz cuvette and filled with index fluid (Cargille laboratories, Series M, $n = 1.8$) in order to refresh the oil in contact with the sample. The index fluid had a temperature coefficient of $-0.000711 \Delta n/\Delta T$ from 25 $^{\circ}\text{C}$ with a flash point of 110 $^{\circ}\text{C}$.

Chapter 4

Scalable Fabrication of Ion-Tunable Protein Hydrogel Nanostructures

Related publication:

T. Reese, K. Singh, C. Buck, P. Dennis, T.W. Odom, “Scalable Fabrication of Protein Hydrogel Nanostructures,” In preparation.

4.1. Introduction

The biomedical community has significant interest in developing biocompatible nanostructures for applications regarding regenerative medicine,^{111, 168} drug delivery,^{110, 169} biophotonics^{60, 115, 116} and bio-electronics.¹¹⁷ Existing biocompatible materials, such as ceramics, metals and polymers, are necessarily inert, which limits their biodegradability and potential for chemical functionalization.¹⁰ Protein based polymers are an attractive alternative to synthetic polymers due to their intrinsic biocompatibility, biodegradability and tunable functionality. The most prominent example of protein polymers is silk,^{60, 110, 111, 115-117, 170-172} but processing often requires the use of hazardous materials. In addition, production of silk solutions is difficult to scale because the protein is usually extracted from silkworm cocoons.

Suckerin, a naturally occurring protein found in squid ring teeth, has emerged as an appealing biopolymer because of robust mechanical properties.¹¹²⁻¹¹⁸ The Young's modulus of Suckerin can be tuned over multiple orders of magnitude dependent on ionic solution used in crosslinking, up to the GPA range.¹¹² Suckerin is promising for expanded functionality because the protein backbone is electrically charged, which allows it to be readily functionalized or used in redox reactions.¹⁷³ Suckerin-12 (S12), a low molecular weight isoform of the Suckerin protein, can be recombinantly expressed to generate gram quantities of solution.^{112, 114} S12 is soluble in aqueous solutions at moderate pH. Enzymes can be used for crosslinking, so robust structures can be formed without the use of UV-light.

Due to the excellent combination of mechanical, biological and chemical properties, S12 is ideally positioned for bio-optic, bio-electronic and bio-scaffold devices. Control of dimensions at sub-micron length scales for these applications is critical, as components involving photonics,

microelectronics or organ grafts require feature sizes on the order of hundreds of nanometers. Biopolymer nanostructures have been fabricated but need complicated processing techniques. Most studies have relied on electron-beam lithography (EBL), but generating patterned areas over cm scale can be prohibitively cost and time intensive.^{60, 171} In addition, the features formed by EBL were transferred to biopolymers through UV crosslinking or high temperature and pressure imprint lithography. Microscale structures can be fabricated by well-established and scalable lithography techniques but are constrained by the diffraction limit of light.

In this chapter, we show a highly scalable process to generate nanostructured protein polymers from microscale patterns using simple table-top procedures. We molded PDMS masks from Si masters that had been created by traditional photolithography and etching methods. Then, we took advantage of the controllable contraction of certain protein hydrogels, primarily S12, to realize regularly spaced nanofeatures over large (cm²) areas. Finally, we demonstrate the ability to pin in-plane features while contracting out-of-plane features by treating the surface of the PDMS masks prior to adding S12. The protein polymer micro- and nanostructures were profiled by liquid cell AFM, which allowed us to image the samples in a buffer solution similar to the environment they would experience in a living body. Our results establish a technique for rapidly producing a range of miniaturized protein polymer structures while giving insight into the means by which organisms naturally create protein components.

4.2. Fabricating Nanoscale Protein Hydrogel Architectures

4.2.1. *Process Flow for Generating Nanoscale Features from Microscale Masks*

Figure 4.1 displays the process flow we used to generate protein polymer micro-

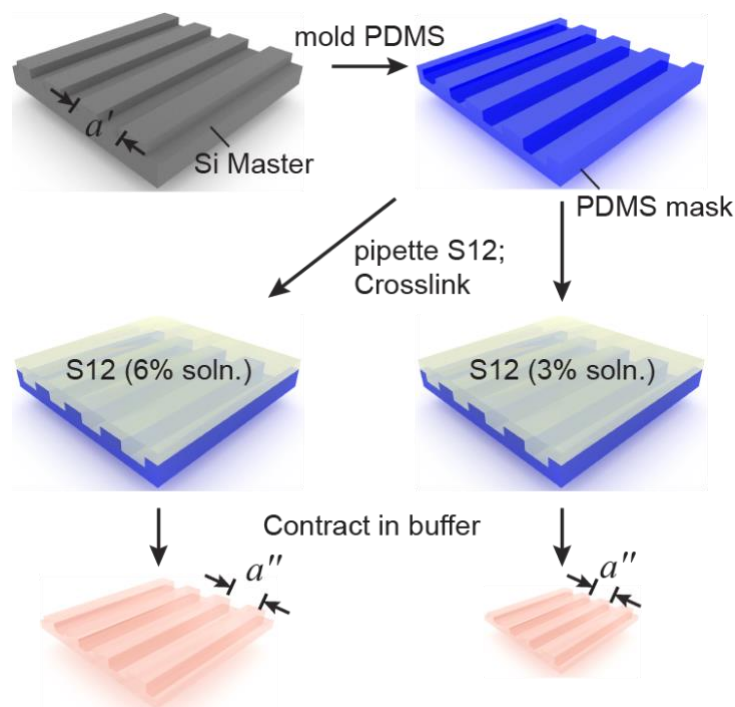


Figure 4.1. Scalable process flow for fabricating protein hydrogel nanostructures. S12 nanostructures can be formed from microscale PDMS molds by taking advantage of S12 contraction in buffer solution.

and nanostructures. Si masters were formed by spincoating photoresist (PR) onto Si wafers and exposing them through a Cr mask with periodic features (a) using a photolithography mask aligner. After developing the exposed sample to realize a PR mask, the Si substrate was etched by reactive ion etch (RIE). PDMS (Sylgard-184) masks were molded from these Si masters.

To manufacture the S12 solution, we synthesized gram scale of S12 through recombinant protein expression and dispersed it into aqueous solutions of 3% and 6% concentration. 100-300 μL of S12 solution was pipetted into the PDMS (**Figure 4.2**) and enzymatically crosslinked by horseradish peroxidase (HRP), which allowed us to avoid the use of UV-irradiation. We cross linked the S12 in the PDMS mold in a humid environment at 27 $^{\circ}\text{C}$ for approximately 15 hours. The S12 is then placed into a buffer solution (100 mM NaOAc) and lightly separated from the

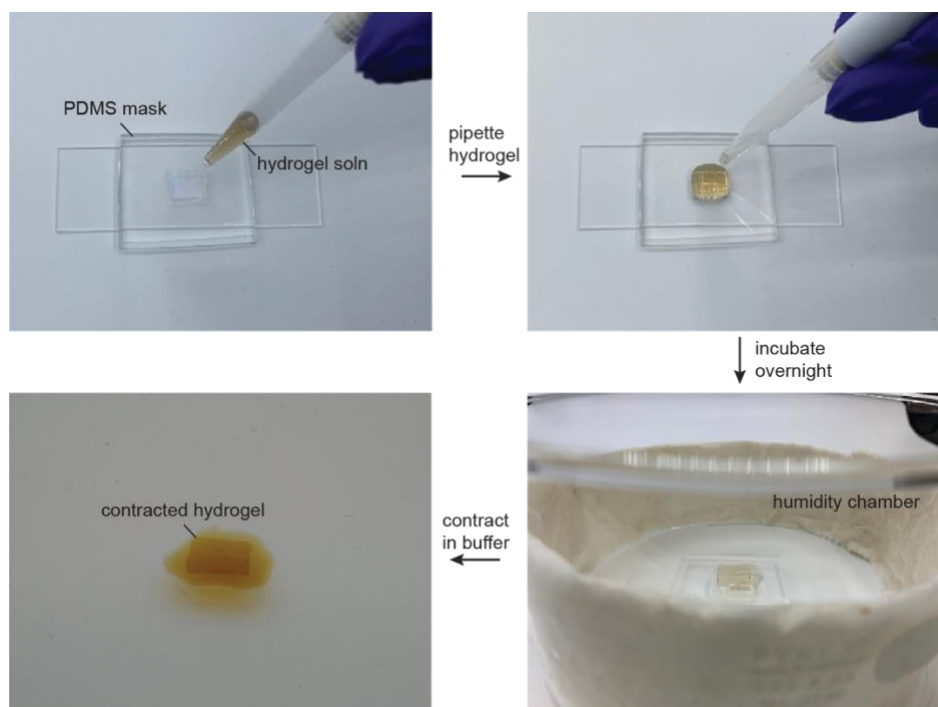


Figure 4.2. Processing for protein hydrogel nanostructures. Photographs depicting the process of contracting large areas of nanopatterned hydrogels

PDMS mold and allowed to contract for several hours. Contraction occurs due to the deprotonization of histidine residues in the protein backbone. The ionic solution causes charge screening, which forces excess water from the S12 hydrogel. The degree of contraction has shown to highly depend on the concentration of S12 solution at the macroscale,¹¹⁴ but this relationship is unknown at the micro and nanoscale.

4.3. Contracted Suckerin-12 Hydrogel Microstructures

4.3.1. 1D and 2D Contraction

To establish a baseline for S12 contraction using our process flow, we began by using PDMS masks patterned with microscale periodic features. **Figure 4.3a** shows an SEM images of a Si

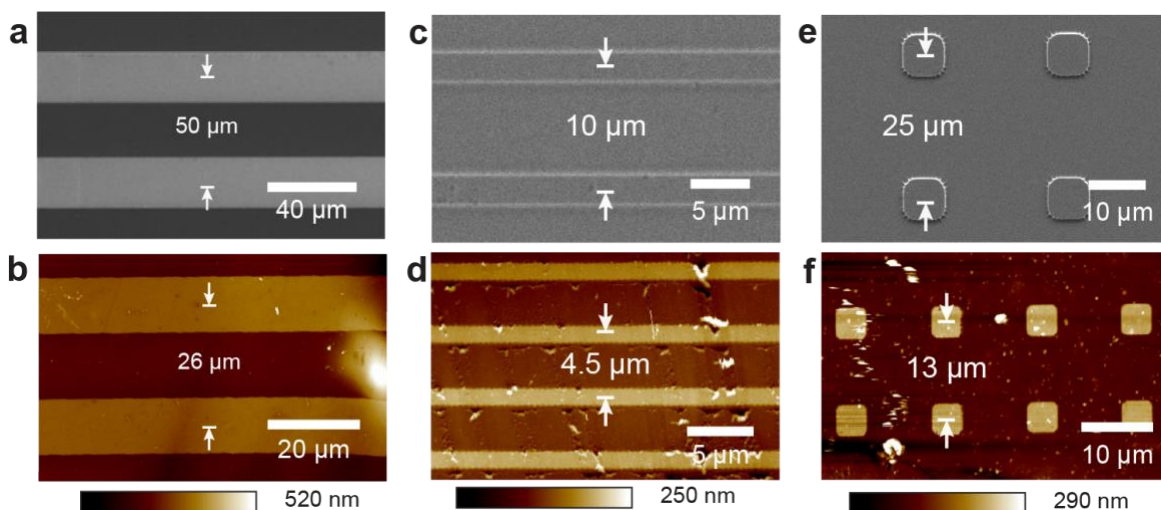


Figure 4.3. SEM Images of Si masters and their resulting contracted S12 microfeatures. SEM images of Si masters with (a) $a' = 50 \mu\text{m}$ lines, (c) $a' = 10 \mu\text{m}$ lines and (e) $a' = 25 \mu\text{m}$ squares. AFM images of contracted S12 microfeatures with (b) $a'' = 26 \mu\text{m}$, (b) $a'' = 4.5 \mu\text{m}$ and (b) $a'' = 13 \mu\text{m}$. All samples used 6 wt% S12 solution and contracted in 100 mM NaOAc buffer.

master line gratings with $a' = 50 \mu\text{m}$ that was used to mold a PDMS mask. These features are relatively large and 1D, which makes them a simple platform to ensure S12 contraction is similar at microscale to macroscale while using our procedures. **Figure 4.3b** shows an AFM image of S12 lines that have contracted to $a'' = 26 \mu\text{m}$, which represents a decrease of approximately 50%. Liquid cell AFM was used to capture the images as the hydrated state in buffer solution represents a more accurate environment for future applications than dried in air. We tested additional microscale line patterns with $a' = 10 \mu\text{m}$ (**Figure 4.3c-d**) and found similar contraction to $a'' = 4.5 \mu\text{m}$. Both contracted microscale lines show relatively sharp side walls, flat tops and flat troughs, which indicates that contraction occurs under hydrostatic compressive stress. This is consistent with the theory that water is excised from the hydrogel during contraction because of charge screening.

We further tested S12 contraction with microscale PDMS masks consisting of 2D square array features (**Figure 4.3e**). **Figure 4.3f** shows that the contracted period ($a'' = 13\mu\text{m}$) continues to be approximately 50% of the original mask dimensions ($a' = 25\mu\text{m}$). In addition, the microscale squares do not exhibit significant rounding at their corners, which suggests that S12 contraction can accurately scale features to smaller dimensions without losing geometric integrity. The squares and their surrounding area also show flat surfaces without noticeable bowing.

4.3.2. Effect of S12 Solution Concentration on Microscale Features

After determining 6% S12 solution contracted at the microscale in similar fashion to the macroscale, we proceeded to vary the concentration. **Figure 2.4** shows decreasing the wt% of S12 in solution further shrinks the dimensions of the S12. **Figure 2.4a-b** are similar to the results shown in **Figure 2.3e-f**. **Figure 2.4c** shows that 3 wt% S12 contracts features to approximately 40% of their original PDMS mask size. Even under more extreme contraction, the squares do not show significant rounding. AFM line traces indicate that while the tops of the posts are of relatively even height, they contain of many bumps that are several nanometers in height. These features may be due to individual S12 nanospheres, which are on the order of tens of nanometers.¹⁷⁴

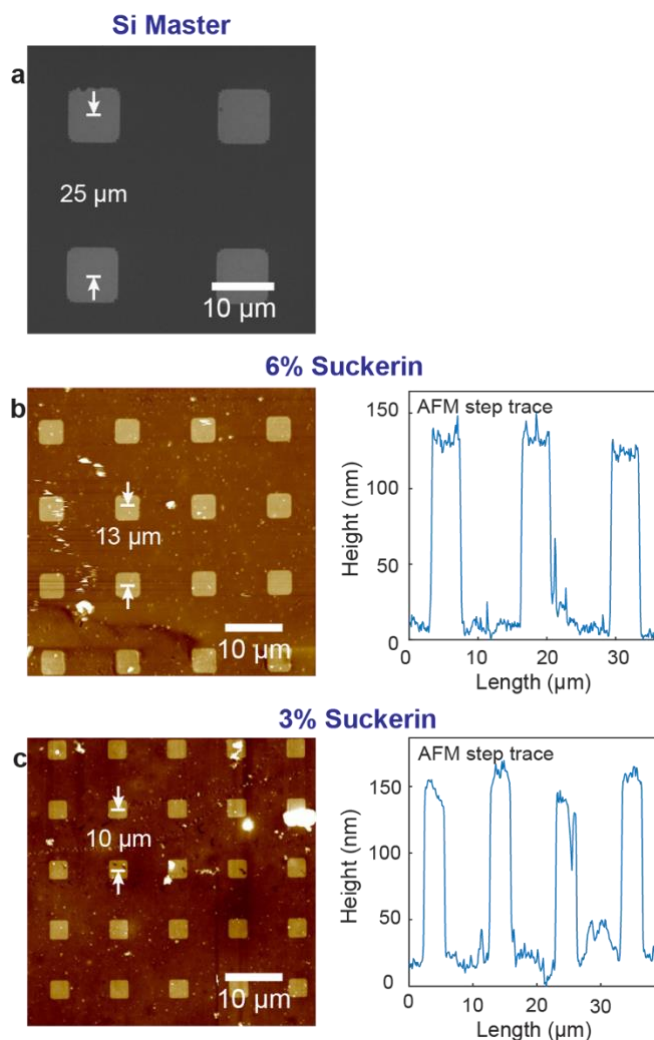


Figure 4.4. Effect of S12 solution concentration on contracted microfeatures. (a) SEM images of Si masters with $a' = 25 \mu\text{m}$ squares. AFM images and height line traces of contracted S12 microfeatures from (b) 6 wt% and (c) 3 wt%. All samples were contracted in 100 mM NaOAc buffer.

4.4. Nanoscale Suckerin-12 Architectures from Microscale Masks

To confirm that the S12 contraction trends observed at the micro- and macroscales continue at the nanoscale, we fabricated Si masters and molded PDMS masks with periodicity of $a' = 2 \mu\text{m}$

(Figure 4.5a) and $a' = 1 \mu\text{m}$ (Figure 4.5b) through photolithography and pattern transfer. Figures 4.5b,c,e,f show that the periodicity of the resulting S12 nanostructure continues to contract to similar percentage of the mask features (50% for 6wt% S12 and 40% for 3wt% S12). However, the lines themselves contract less than in the microscale patterns while the gaps between them contract more significantly (quantitatively shown in Figure 4.7). We hypothesize that as we approach the size of the individual S12 nanoassemblies, the resolvable features reach their lower

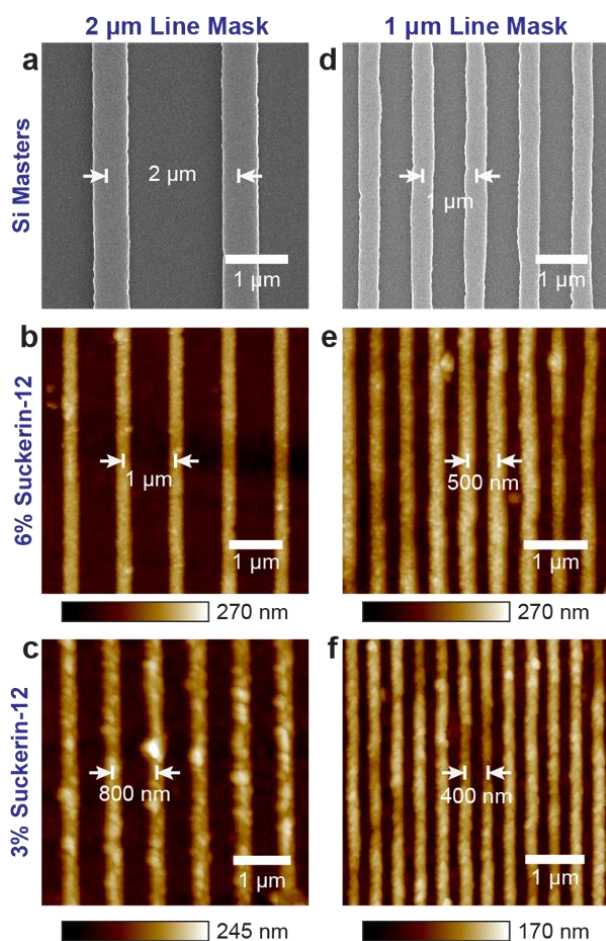


Figure 4.5. S12 nanostructures from microscale masks. SEM images of Si masters used for PDMS masks with $a' =$ (a) $2 \mu\text{m}$ and (d) $1 \mu\text{m}$ lines. AFM images and height line traces of contracted S12 nanostructures from $a' = 2 \mu\text{m}$ masks from (b) 6 wt% and (c) 3 wt% solution and $a' = 1 \mu\text{m}$ masks from (e) 6 wt% and (f) 3 wt% solution. All samples were contracted in 100 mM NaOAc buffer.

limit. These results indicate that S12 nanostructures below the diffraction of light can be achieved through highly scalable photolithography techniques.

4.5. Anisotropic S12 Replication of Mask Through Surface Modification

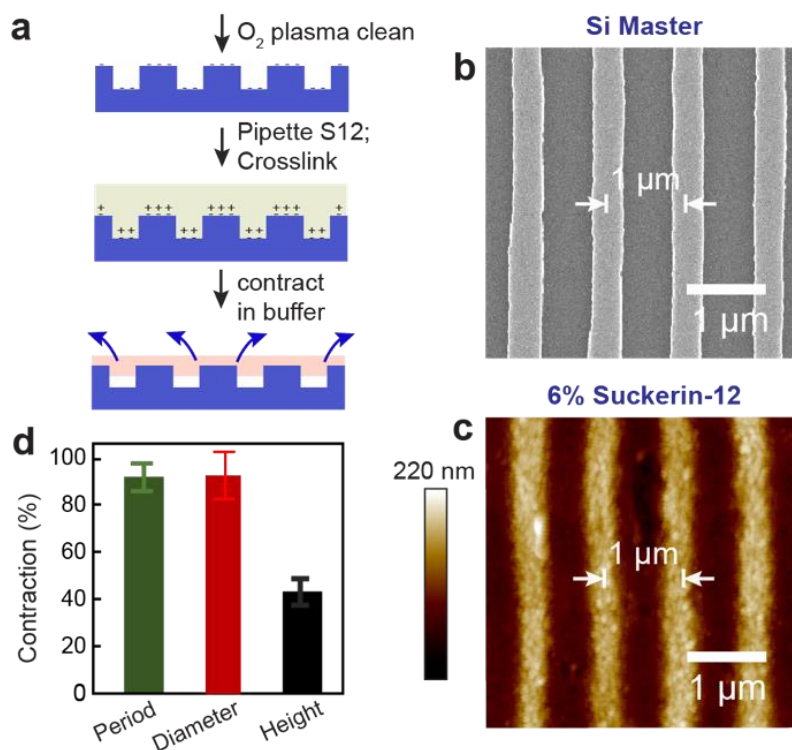


Figure 4.6. Anisotropic contraction of S12 nanostructures through PDMS surface functionalization. (a) Process flow depicting anisotropic contraction by treating PDMS mask with O_2 plasma. (b) SEM of Si master with $a' = 1 \mu\text{m}$ masks that was used to mold PDMS mask. (c) S12 nanostructure (6 wt% solution) after several hours immersed in buffer solution while in negatively charged PDMS mask. (d) Bar graph showing contraction percentage of S12 nanostructure period, line diameter and line height relative to initial PDMS mask. Samples was contracted in 100 mM NaOAc buffer.

Although the ability to produce isotropically contracted nanoscale patterns from microscale masters is a powerful tool for generating large areas of bio-active nanophotonic devices, there may be instances when direct replication or anisotropic contraction of feature dimensions is preferred.

We hypothesized that we could pin the S12 nanostructure to the PDMS mask by taking advantage of the positively charged S12 backbone. **Figure 4.6a** shows the process flow for achieving direct replication and theorized mechanism. Before pipetting S12 solution into the PDMS mask (Si master shown in **Figure 4.6b**), we treated the mask with approximately 1 minute of O₂ plasma by an oxygen plasma cleaner. This process negatively charges the PDMS mask. We added 6% S12 solution, crosslinked and incubated similar to our previous experiments, then placed the sample in NaOAc buffer solution. Unlike when using an untreated mask, the S12 did not naturally release from the PDMS after a few minutes of contraction. We attempted to detach the S12 but found the S12 to be more strongly adhered to the mask. After several hours, we pulled the S12 from the PDMS with more force, which the S12 structure was able to tolerate due to its high Young's modulus. The S12 structure showed no observable contraction after additional time in the buffer solution. The AFM image in **Figure 4.6c** shows that the periodicity and width of the S12 lines are approximately the same dimensions as the Si master, which indicates that surface functionalization of the mask is successful in pinning the crosslinked S12. Further experiments must be performed to conclude the precise mechanism, but these results suggest that the S12 may be deprotonated by the negative charges on the PDMS mask. Another possible explanation is that the S12 is only pinned on the top of the PDMS due to the high surface area, but anisotropically contracts out of plane. This conclusion is supported by the height of the S12 lines being approximately 45% of the original PDMS mask (**Figure 4.6d**). However, we are unsure if contraction of the height of the nanofeatures occurs after releasing the S12 from the PDMS or if it occurred while still inside the mask. By confining the contraction to a single dimension, we show a possible explanation for how functional biocomponents can be engineered in nature.

4.6. Summary of S12 Contraction Experiments

Figure 4.7 shows the general trends of contraction for all S12 samples addressed in Chapter 4.2-4.5. Regardless of original PDMS mask dimensions, the periodicity of contracted S12 (green bars) is primarily dictated by the S12 solution concentration. This parameter is the most essential for controlling the wavelength of SLR wavelengths in an ordered array, which could be an ideal application of these contracted patterns. However, as the mask sizes approach the nanoscale, the gaps between lines (blue bars) contract more relative to the microscale patterns while the line widths (red bars) remain closer to the width of the line features on the PDMS masks. We suspect this phenomenon is related to the average diameter of self-assembled S12 nanoparticles, but smaller mask features are necessary to confirm this assumption.

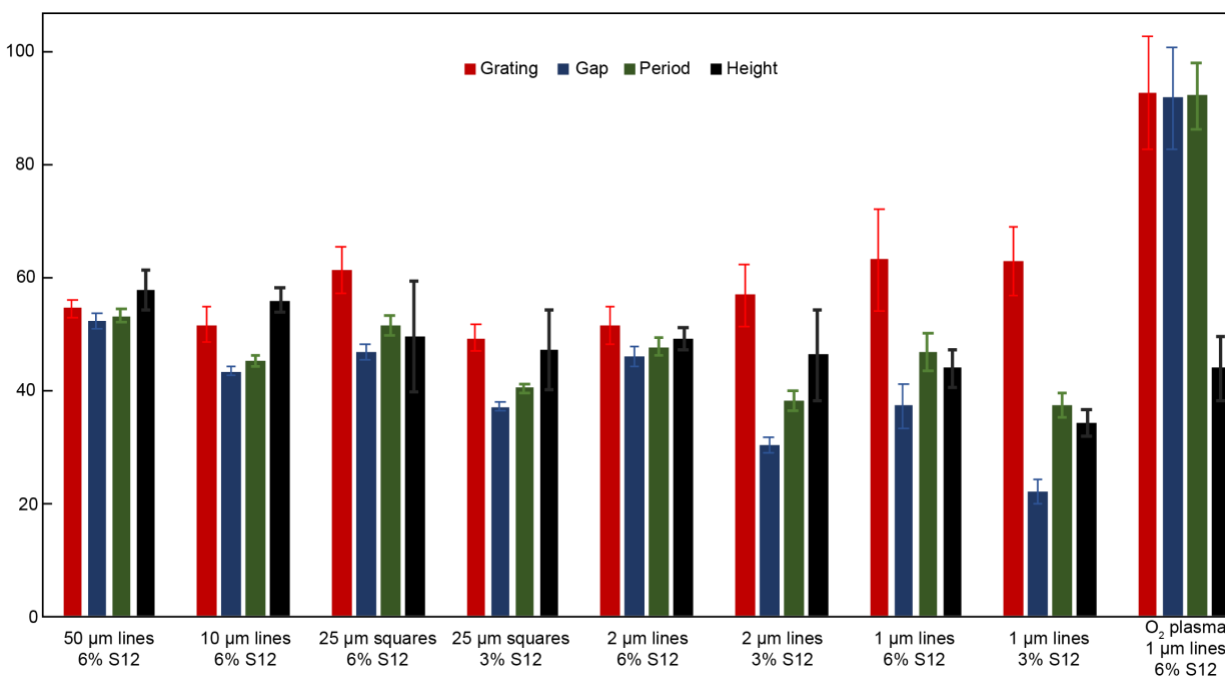


Figure 4.7. Contraction percentage of grating width, trough gap, periodicity and height for S12 hydrogels using different masks and procedures.

4.7. Expanding Process Flow to NVJP-1

To ensure that our process flow could be generalized to additional protein polymers in the future, we also contracted *Nereis virens* jaw protein (NVJP-1) nanostructures. Similar to S12, NVJP-1 can achieve robust mechanical properties and significant contraction through crosslinking and ion exposure. NVJP-1 also has a histidine-rich backbone,¹⁷⁵ so the mechanism of charge-screening is thought to be the same (or closely related) to that of S12. However, unlike S12, NVJP-1 can be reversibly sclerotized through progressive anionic exposure. NVJP-1 may have broader biomedical and biophotonic applications than S12 because the dimensions and properties of a structure can be active tuned. **Figure 4.8a** shows the PDMS mask that we previously used in

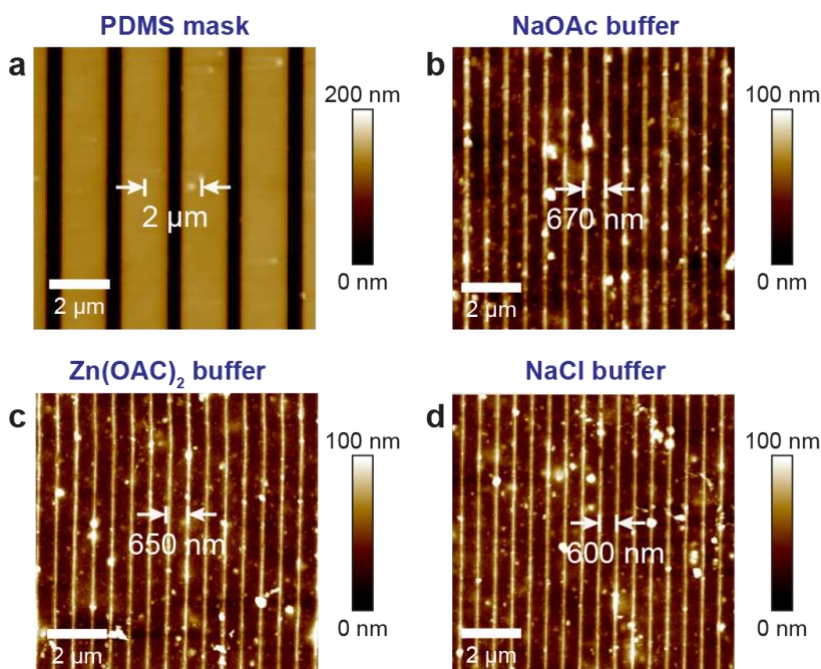


Figure 4.8. NVJP-1 nanostructures with buffer progression (a) AFM image of PDMS mask used in NVJP-1 molding and contraction with $a' = 2 \mu\text{m}$. AFM images of NVJP-1 nanostructures after in contraction in (b) NaOAc, then (c) $\text{Zn}(\text{OAc})_2$ and finally (d) NaCl 200 mM buffer solutions. Hydrogels were imaged in their respective buffer solution.

Figure 4.5a with $a' = 2 \mu\text{m}$. We prepared NVJP-1 protein through a similar gram-scale production using bacterial expression.¹¹⁹ NVJP-1 was reconstituted into 3 wt% aqueous solution and pipetted into the PDMS mask according to the procedures shown in Figure 4.1 and Figure 4.2. After contracting in 200 mM NaOAc buffer solution for several hours, the NVJP-1 line patterns show $a'' \approx 670 \text{ nm}$, which represents a decrease to 33% of the original dimensions (**Figure 4.8b**). This reduction in dimensions is similar to what we observe for 3% S12 using the same mask. After imaging in NaOAc buffer, the sample was transferred to 200 mM $\text{Zn}(\text{OAc})_2$ buffer for several hours. This process metalizes the NVJP-1 to increase the rigidity of the structure (the Young's modulus by approximately two orders of magnitude).¹¹⁹ **Figure 4.8c** shows that there is minimal reduction of periodicity to $a'' \approx 650 \text{ nm}$. To further increase contraction and Young's modulus, the nanostructure was placed in 200 mM NaCl buffer solution (**Figure 4.8d**). After exposure to Cl^- ions, the periodicity decreases to $a'' \approx 600 \text{ nm}$. Future experiments will reintroduce NaOAc buffer and strain the sample to modify the periodicity at will.

4.8. Conclusions

In summary, we developed a scalable procedure to generate sub-micron protein hydrogel features from microscale PDMS masks. Depending on the protein concentration used, we could contract the hydrogel features to 35-50% of their original dimensions through ionic crosslinking. Furthermore, we showed that O_2 plasma could be used to functionalize the PDMS masks and cause anisotropic contraction of the hydrogel nanostructures by pinning in-plane features while out-of-plane features shrink. This pinning may be due to bonding of the negatively charged PDMS surface

to the positively charged histidine residues in the protein backbone and suggests a possible mechanism for controlled biomineralization in nature. In the future, the reversible mechanical properties of NVJP-1 could be used as a substrate for ordered plasmonic nanostructures that can spontaneously react to the environment to modulate the optical response. The fabrication techniques shown here enable future development of bio-compatible nanoscale devices that may have applications in regenerative medicine, bio-electronics or bio-photonics.

4.9. Methods

4.9.1. PDMS Mask Fabrication

To generate Si master, photoresist (Shipley 1805) was mixed with PGMEA in a 1:2 ratio and spincoated onto a ALD-alumina coated Si wafer. Cr mask patterns were exposed at a dosage of 90-120 mJ/cm² at $\lambda = 365$ nm in a mask aligner system. After development, the PR patterns were transferred into alumina by an Al wet etch (Transene type A)¹⁷⁶ and then Si through a DRIE etch for 2-5 min of exposure. The PR was removed by sonicating in solvent (Microchem photoresist remover 1165). A Sylgard-184 PDMS mask was cast from the Si masters.

4.9.2. Expression of NVJP-1

A codon optimized Nvjp-1a1 isoform coding sequence was synthesized (Genescript) and cloned into a pET11 expression vector. The resulting pET11 Nvjp-1 construct was then transformed into BL21 DE3 cells. M63 media was prepared by adding 3 g of anhydrous KH₂PO₄, 7 g of anhydrous K₂HPO₄, 2 g of (NH₄)₂SO₄, 2.8 mg of FeSO₄·7H₂O, 3 mg of sodium citrate tribasic dehydrate, 16 g of tryptone, 10 g of yeast extract, and distilled water to a final volume of 1 L. The media was sterilized by autoclaving. Upon cooling, 1 mL of 1 M MgSO₄ solution, 10 mL of 20% glucose solution, and ampicillin (to a final concentration of 100 µg/mL) were added to the

media. Expression cultures were inoculated and grown up in M63 media to an $OD_{600\text{ nm}}$ of 0.6–0.8 before being induced with 0.4 mM IPTG in a shaking incubator for 12 h at 37 °C. Bacterial cells were pelleted, resuspended in 50 mM Tris-HCl, pH 8, 150 mM NaCl, 100 $\mu\text{g/mL}$ lysozyme and disrupted by sonication. After centrifugation, the insoluble pellet containing inclusion bodies was washed twice with 50 mM Tris-HCl, pH 8, 150 mM NaCl, 1% Triton followed by one wash with 50 mM Tris-HCl, pH 8, 150 mM NaCl. The pellet was resuspended in water, and the pH was adjusted to 3 with 1 N HCl followed by centrifugation. NaCl was then added to the supernatant to a final concentration of 100 mM, and the pH was adjusted to 8 with 1 N NaOH followed by centrifugation. The pellet was solvated in 6 mM HCl and dialyzed overnight against water. After lyophilization, Nvjp-1 was reconstituted to a final concentration of 60 mg/mL in water, centrifuged, and lyophilized a second time before being stored dry at $-20\text{ }^{\circ}\text{C}$ until use. Full procedure adapted from ref¹¹⁹

4.9.3. NVJP-1 Hydrogel Formation

Purified Nvjp-1 was reconstituted in water to a final concentration of 30 mg/mL, and stock solutions of 2000 units/mL horseradish peroxidase (HRP) and 0.65 M hydrogen peroxide were prepared. In a typical cross-linking reaction, 4 μL of HRP and 1 μL of hydrogen peroxide stock solutions were added to 100 μL of the Nvjp-1 solution yielding a final concentration of 80 units/mL HRP and 6.5 mM hydrogen peroxide. The solution was lightly sonicated and approximately 200 μL were cast into a patterned PDMS mask. Full procedure adapted from ref¹¹⁹

4.9.4. Expression and Purification of Recombinant Suckerin-12 in Escherichia coli of NVJP-1

The coding sequence of the suckerin-12 gene was synthesized (GenScript) and sub-cloned using NdeI and BamHI into the pET15b expression plasmid (Novagen) with an amino terminal hexa-histidine tag. The plasmid was then transformed into *E. coli* (BL21 DE3) cells (Invitrogen) under ampicillin selection. Once cell cultures reached an optical density (OD₆₀₀) of 0.6–0.8, expression of the hexa-histidine tagged suckerin-12 was induced with 0.4 mM isopropyl β-D-1-thiogalactopyranoside for 12 h at 37 °C. Induced bacterial cultures were then centrifuged (8000 RPM for 10 min) and extracted with lysis buffer (50 mM Tris pH 8, 100 mM NaCl, 100 μg mL⁻¹ lysozyme) followed by sonication and centrifugation (8000 RPM for 10 min). Insoluble inclusion bodies were washed two times in Triton X-100 wash buffer (1% Triton X-100, 50 mM Tris pH 8, 100 mM NaCl) followed by one wash in the same buffer without Triton X-100. Suckerin-12 was then purified using a column-less protocol adapted from ref^{118, 173}. The washed inclusion bodies were resuspended in water and the pH adjusted to 3 with 1 M HCl followed by centrifugation (8000 rpm for 10 min). The resulting supernatant was adjusted to pH 8 with 1 M Tris HCl, pH 9, 100 mM NaCl. After centrifugation, the precipitate was washed twice in 80% ethanol, dried, weighed, and then resuspended in water at a concentration of 6 wt/vol%. Then, the pH was lowered to 3 with glacial acetic acid followed by dialysis overnight in water and then lyophilization. Dried protein was stored at –80 °C and resuspended to 6 wt/vol% protein weight in water and adjusted to pH 5 with glacial acetic acid for immediate use. Full procedure adapted from ref¹¹⁴

4.9.5. Suckerin-12 Hydrogel Formation

Suckerin-12 hydrogels were formed by casting them into PDMS molds and crosslinking with horseradish peroxidase (HRP) (Sigma P8375) using procedures adapted from ref¹⁷⁷. HRP and

H₂O₂ amounts were optimized for maximum crosslinking after overnight incubation at room temperature. The HRP (2000 units per mL, Sigma-Aldrich P8375) was stored at -80 °C in small aliquots. The hydrogel reaction mixture contained 3 wt/vol% or 6 wt/vol% suckerin-12, 0.04 wt/vol% H₂O₂, and 0.8 units per mL of HRP, and was stored in humid conditions overnight at 27 °C. Hydrogel patterns required 100-500 μL of the suckerin-12 reaction mixture. Full procedure adapted from ref¹⁴

Chapter 5

Summary & Outlook

To conclude, this thesis demonstrated a variety of nanofabrication advances that enable active materials and architectures. The procedures shown here have implications across many fields, including optical communication through optical switches or multiplexed optical components, solid state lighting through multi-wavelength lasing, CMOS integrated optoelectronics capable of withstanding extreme conditions, and bio-responsive photonics. In addition to possible applications, this work provided fundamental insight into long-range interactions of surface lattice resonances at ultrafast and steady-state timescales.

In Chapter 2, I showed highly scalable procedures to generate either multi-metallic or partially filled NP arrays with uniform dimensions. Surprisingly, we found that quasi-periodic patches (with microscale gaps) of regularly spaced NPs with very low filling factors could still act as nanoscale cavities for lasing action. By expanding to multi-metallic arrays, we could produce multiple high-quality SLRs simultaneously. Because the process flow could be customized in terms of materials and periodicities, we could realize surface lattice resonances throughout a wide range of wavelengths in the visible and near-infrared. In contrast to nanostructures that rely on anisotropic units, the normal incidence optical properties of our system are polarization-independent. With future developments in gain media, we expect that this multi-metallic system could support tri-modal lasing simultaneously. Because single metal arrays showed lasing at filling factors as low as 10%, multi-material systems may be able to expand beyond three materials. Furthermore, this procedure could likely be integrated with fabrication shown in chapter 3 to generate structures with a combination of arrays produced by top-down etching of epitaxial materials (metallic or dielectric) and materials deposited through floated Au hole masks. We expect these multi-metallic and multi-resonant architectures to have applications outside of nanoscale lasers, such as for efficient light collection or multi-step catalytic substrates.

In chapter 3, we generated high-quality TiN NP arrays that could support SLRs and measured their steady-state and excited optical properties. Because TiN is a robust material and the substrates necessary for epitaxial growth have a high index of refraction, this is the first experimental demonstration of coupled TiN NPs at normal incidence. Although sharp and deep dipolar SLRs were difficult to achieve, I was able to realize sharp quadrupolar SLRs by increasing the thickness of TiN NPs. I characterized the ultrafast properties of broad dipolar SLRs, sharp quadrupolar SLRs and broad LSPs with transient absorption at wavelengths far from TiN interband transitions and found that resonance line shape played a role in the symmetry of photoinduced features. My results suggest that a sharp resonance (and intense local electric fields) do not necessarily correlate with a significant ground state bleach. Although the relaxation for TiN photoexcited carriers is slower than noble metals, which may limit applications as optical switches, the ability of TiN to withstand extremely high fluences provides a possible way to efficiently modulate transmitted light.

Chapter 4 provides a framework for environment-sensitive ordered nanostructures. I was able to produce sub-micron Suckerin-12 and NVJP-1 protein hydrogel features over large areas from PDMS masks that could be generated by widely available photolithography equipment. The protein hydrogels contracted isotropically in a similar manner to their macroscopic counterparts. Our experiments with functionalized PDMS masks revealed that charged surfaces may be a possible mechanism for organisms to control biomineralization anisotropically. In addition, the ability to directly replicate lateral dimensions while increasing the Young's modulus of nanoscale features may prove useful for customized regenerative medicine. This work will lead to further developments in transferring NP arrays into protein hydrogels to dynamically tune the lattice spacing and therefore the SLR wavelength.

Nanofabrication will continue to play a significant role in future technological breakthroughs.

As the field of active nanophotonics transitions from fundamental research to applied devices, scalable methods of production will become even more critical. Components capable of confining and transporting light at the nanoscale may provide a low energy solution to overcoming the limitations of Moore's Law, especially if they can operate at multiple wavelengths for increased data throughput. In the near future, emerging topics in nano-optics, such as plasmonic Moiré patterns and topological photonics, will require innovative nanofabrication techniques to realize their widespread potential. Further, as computational methods for predicting and synthesizing more efficient plasmonic materials become more prevalent, new nanofabrication methods will be critical for maximizing their potential in the form of compact optical devices.

Appendix A

Optimization and Fabrication of Stretchable Metalenses

This work is based on the final report completed to fulfill the requirements of the Predictive Science and Engineering Design Cluster Fellowship.

A.1. Introduction to Metalenses

Traditional lenses give a constant optical response throughout their lifetime and therefore cannot be modulated on-the-fly to correct for damage or any sort of aberration. Metalenses, or two-dimensional lattices comprised of subwavelength features, can focus the flow of light in unique ways not realized in nature. Such structures have been used to realize cloaking devices, achromatic flat lenses, and optoelectronic components.

The arrangement of nanofeatures can control the phase of the scattered light, which interacts constructively and destructively to result in a far field light profile. Through computational optimization techniques are able to determine the optimal structure that produces the light profile desired. The design of the metasurfaces often relies on heuristic optimization algorithms which determine the location of the nanofeatures on a square array to achieve a desired light profile. This method results in extremely complex layouts that are difficult to manufacture and limit scalability. In addition, 3D electric fields must be saved for each particle over the entire volume of interest, therefore the required memory storage increases geometrically with the total area.

We propose stretchable plasmonic metasurfaces, which are multifunctional, mechanically flexible and durable, and more compact than classical dielectric lenses. Our research objective is to incorporate a novel fabrication method with a genetic algorithm (GA) optimization approach while accounting for the manufacturing constraints to stretchable metasurfaces, effectively allowing a single physical surface to achieve multiple lattice spacing dependent desired responses.

A.2. Predictive Results of Stretchable Metalenses

Genetic Algorithm based optimization approaches have been developed to determine the metalens designs that are able to achieve a specified focal location or locations. The inputs of the algorithm are particle type, particle size, particle spacing, size of the array, and desired focal points. In the case of a single focal point, the GA evaluates the far-field response of the array of nanoparticles at a $1\ \mu\text{m}$ square window around the desired focal point location. The response is only calculated over a small domain is to decrease computational expense, as the larger the window

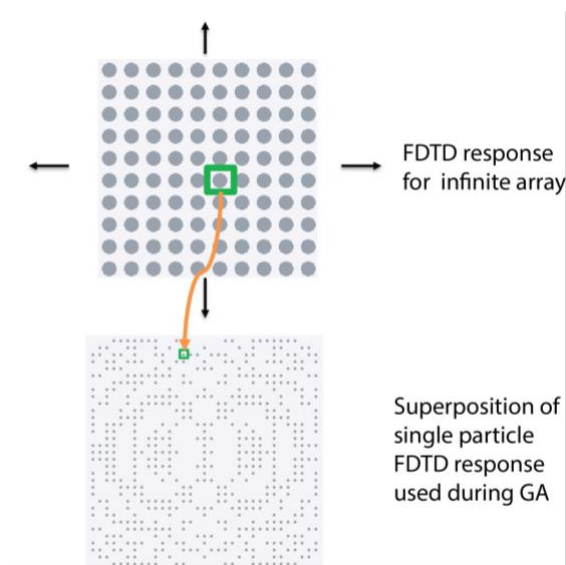


Figure A.1. Schematic showing how the fields for a single NP are saved assuming an infinite, perfectly periodic array and are superimposed to determine the response in the GA.

the greater the computational cost. While the full response can be calculated extremely accurately using a FDTD computation, a simpler superposition has shown to be extremely effective. For the simplified superposition response calculation, a full FDTD simulation is observed for a window above a single particle in an infinite array of particles, as shown in **Figure A.1**. While this assumes that the particle is surrounded by an infinite array and accounts for all possible coupling effects, in

previous work this assumption has shown to be sufficient. Each FDTD simulation takes approximately 8-12 hours while the simplified superposition approach takes only a few minutes, greatly decreasing the computational expense of the algorithm while it is searching for the optimal design.

For a single focal point, the objective function of the GA is:

$$\max F = \frac{I}{\|d_{true} - d_{desired}\| + c}$$

Where I , is the max intensity within the window that the GA is calculating the response, d_{true} is the location at which the max intensity occurs, $d_{desired}$ is the center of the window, and c is a constant to ensure that the denominator is nonzero. The algorithm balances the location of the focal point (relative to where it is desired) by minimizing the denominator, and by maximizing the numerator by increasing the intensity of the focal point. To extend the GA to incorporate n focal points the objective function was originally adjusted to the summation of the single objective responses:

$$\max G = \sum_{i=1}^n F_n$$

Where F_i is the defined as the objective function for a single objective. However, this objective function can result in a solution that only achieves a subset of the desired focal points if some objectives dominate and does not guarantee that all focal points will be achieved. As such the multiobjective optimization was chosen to be:¹⁴⁸

$$\max G' = \sum_{i=1}^n F_n + \frac{1}{2} \sum_{i=1}^n \sum_{j=1}^n |F_i - F_j| / (F_i + F_j)^2$$

In this case the first term is the same, while the second term comprised of the double summation is used to ensure that the magnitude of each focal point is approximately the same.

To extend the existing metasurface design framework to the design of stretchable metasurfaces we extended the multiobjective function to incorporate the responses of both particle spacings. The inputs are the two desired particle spacings as well as the locations of the desired focal points at the respective spacing. The algorithm evaluates the response at the window location(s) for each particle spacing and the objective function is the same as before, with the only major difference being that each F_i could come from either spacing.

One of the major challenges remaining is the amount of time necessary to perform the GA optimization and its accuracy while considering the response at multiple particle spacings concurrently. After optimization of the lattice, each FDTD of the full metasurface structure at each lattice spacing takes approximately 4-6 hours. When attempting to optimize a large number of variable such as particle diameter, lattice spacing and wavelength, it can become extremely computationally

expensive to run many different trials for each changed variable. To begin with, we explored whether the superposition response evaluation of the GA was valid. While this assumption that the response of every individual particle, regardless of its surrounding particles, was treated as if it were within an infinite array of particles would hold for a particle surrounded by multiple other particles, the concern was that the GA was not able to accurately model a sparse distribution of particles for which there were no strongly interacting effects with other particles. To validate this hypothesis we calculated both the GA simplified response as well as the true response via an

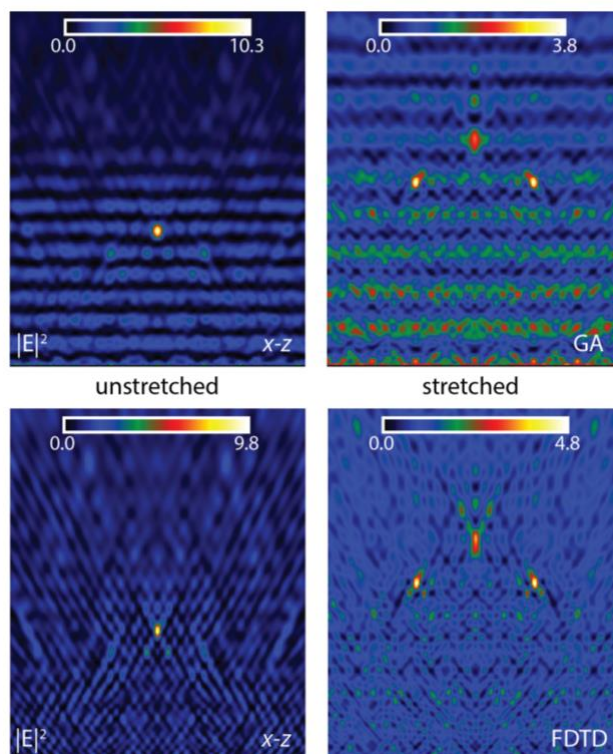


Figure A.2. (Top) x - z windows calculated by the superposition of fields from each lattice unit taken assuming an infinite array. (Bottom) x - z windows calculated by simulating the entire lattice optimized by GA in FDTD

FDTD simulation of the entire optimized lattice for a large variety of converged particle arrays.

We found that both responses were almost identical. An exemplary case is shown in **Figure A.2**.

While the GA response appears to display periodic lines, this is likely due to the smoothing that was used to generate these images, as the GA response has a much lower pixel count than that of the FDTD. It was concluded that the FDTD calculations were no longer necessary to validate the optimized array.

By verifying the accuracy of the GA superposition method of calculating the farfield response we were able to eliminate the FDTD simulations from our designs allowing us to achieve

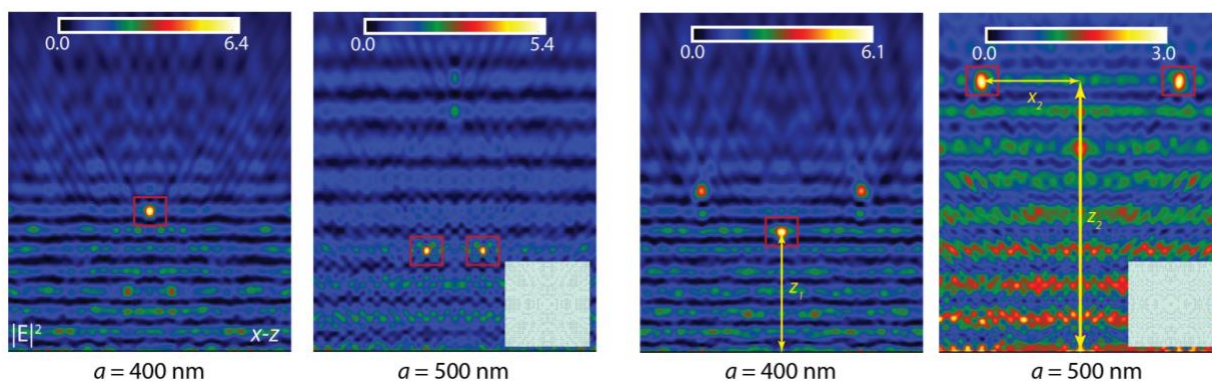


Figure A.3. Two of the compatible responses from the DoE. Red boxes indicate the $1 \mu\text{m}^2$ window that is calculated and optimized by the GA. Yellow arrows indicate the variables that were varied in the DoE. Lattices were optimized for $\lambda = 475 \text{ nm}$, with Al NP diameter of 100 nm and thickness of 50 nm . 40×40 lattice units.

converged solutions in less than half the time. We were also released from the constraints of using Lumerical FDTD licenses, which are limited through the Quest cluster computer at Northwestern University. Meanwhile, we can submit over 100 GA jobs at a time, giving us the full results of all of these jobs which typically converge in 1-12 hours depending on the complexity of the focal points. This allowed us to greatly explore the design space without accounting for computational expense.

During our exploration we found that the algorithm did not always achieve a solution that contained all the desired focal points at both spacings. We sought to determine if was a physical

phenomenon that contributed to the idea of ‘response compatibility’ across the different particle spacings. To explore this phenomenon, we first formulated a confined design space consisting of arrays with four fold symmetry, a single focal point in the unstretched state ($a = 400 \text{ nm}$) located along the z -axis, and two focal points at the stretched state ($a = 500 \text{ nm}$) symmetric about the z -axis. This effectively left us with a design space of 3 variables $z_1, x_2,$ and z_2 , as shown in Figure A.3.

To explore this design space a design of experiments (DoE) of size 200 was generated using Optimal Latin Hypercube Sampling and the GA was performed using the DoE points as the inputs for the desired focal point locations at the respective spacing’s. The figure of merit for the converged results was selected as

$$K = \frac{I_1}{I_2}$$

Where I_1 was the intensity of the single focal point of the unstretched response and I_2 was the average of the two focal points (essentially the intensity of either one due to the symmetry constraint) of the stretched state. A compatible solution was defined as $0.8 < K < 1.25$ (~40% met this criteria) and the others were considered incompatible. With the mindset of determining a

rule of compatibility for the focal locations at the different particle spacing's, we attempted to fit a predictive model to the data. A variety of models were used including neural networks, Gaussian process models, and support vector machines with a variety of response types including classification, modeling I_1 and I_2 independently, and modeling K directly. Regardless of the model or response chosen the predictive model was only able to correctly predict the compatibility of responses 40 – 60% of the time. Based on these results it is inconclusive whether the correct model was chosen or whether there was simply not enough data to correctly model the response. Some of more optimal solutions are shown in Figure A.3. To further investigate we can examine a scatter plot in 3D of both the compatible and incompatible responses shown in **Figure A.4**. In

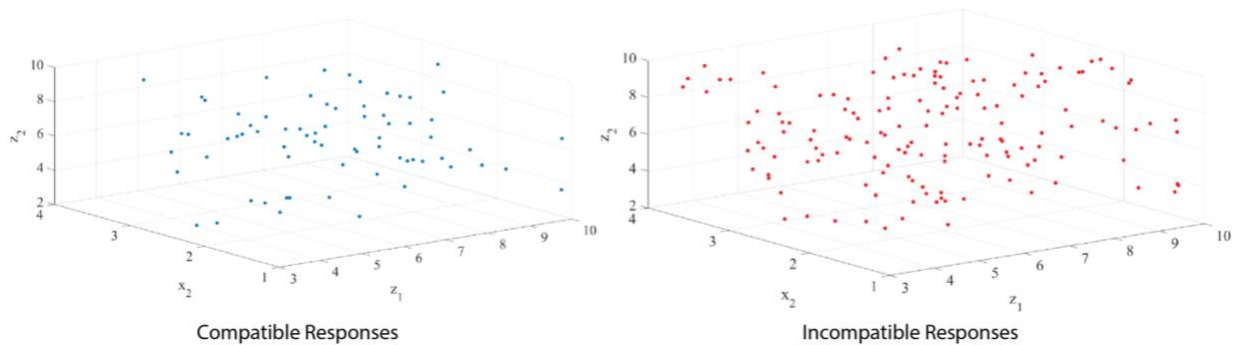


Figure A.4. 3D scatter plot of the (left) compatible responses and (right) incompatible results of the 200 trial DoE

both cases, we see that there is no apparent clustering or correlation between the inputs and the compatibility of the two responses. This result suggests that the response is either not well defined as a function of the input variables or that the response is not continuous. While many of the samples in the DoE were able to converge to acceptable solutions, many of them resulted in solutions in which one of the three focal points dominated over the others. Further work is still

needed to determine the underlying mechanism of this effect. We computationally validated that stretchable metasurfaces are a feasible idea in which a single real space design can achieve multiple targeted response's depending on the chosen particle spacing.

A.1. Fabrication of Stretchable Metalenses

It was necessary to fabricate the proposed flexible metasurface designs to verify the feasibility of embedding an Al NP lattice in PDMS, as well as to measure the resulting light profiles at different lattice spacings through biaxial strain of the sample. Most metasurface structures use a positive tone resist with electron beam lithography or focused ion beam, but we needed to develop a new process flow that would allow transfer of Al NPs off of a Si substrate and into PDMS, which is an elastomer that can be easily strained. The GA was used to optimize lattices for operation at $\lambda = 475$ nm. Optimal Al NPs for this wavelength were found to have a diameter of 100 nm and a thickness of 50 nm. The unstrained lattice spacing used was 400 nm, with the strained state of 500 nm. The optimized lattices were 40 x 40 lattice units. The lattice was then imported into designCAD and saved as a .dc2 file, which can be read by the e beam tool to selectively expose the pattern into the resist.

Figure A.5 shows our proposed process flow. First, a negative tone e-beam resist was to be spun onto a Si substrate. Next, e beam lithography would be used to define the pattern of the lattice optimized by the GA. This pattern would be developed, and in the case of negative tone resists, the unexposed regions of the resist are soluble in the developer solution, and so they are washed

away. A short O₂ reactive ion etch (RIE) step would be used to clean residual resist off of the Si substrate to ensure Al would be deposited directly onto Si. Al would then be deposited through e-beam evaporation, with a thickness according to the desired height of the final NPs to be embedded in the PDMS. Most of our designs used a thickness of 50 nm, as simulations showed this would be thick enough to sufficiently scatter and focus light without forming a conformal layer of Al over the resist posts, which would have limited pattern transfer into the PDMS. The Al coated samples would then be back filled with of PDMS and allowed to cure. The PDMS would then be peeled off, and due to the higher adhesion of Al to Si than the resist, the resist posts topped with Al would be removed from the Si substrate while the majority of the Al film would remain on the Si substrate.

Multiple negative tone e beam resists were used to give flexibility over the fabrication

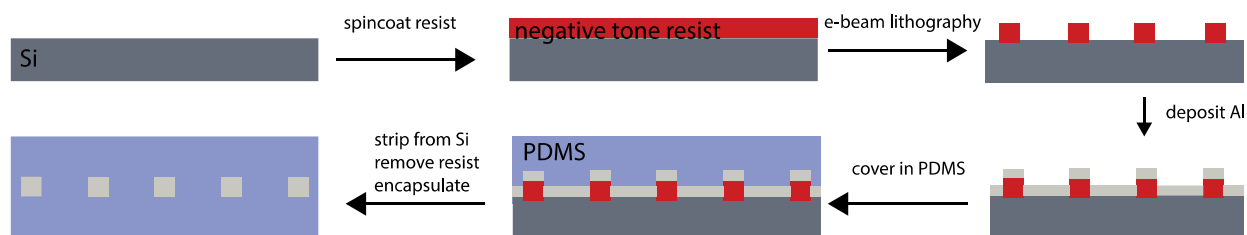


Figure A.5. Process flow for fabricating Al NPs and embedding them in PDMS

process. PMMA, a standard positive tone resist, can be crosslinked at much higher doses than are usually used to act as a negative tone resist.¹⁷⁸ Typical doses are approximately 400-600 $\mu\text{C}/\text{cm}^2$ – we found a dose closer to 18,000 $\mu\text{C}/\text{cm}^2$ gave reproducible negative tone features of our desired dimensions. The standard developer for PMMA when used in a positive resist manner is MIBK, which could be used to give negative tone features (**Figure A.6, left**). However, MIBK

development would remove the resist down to the Si substrate only in the immediate area

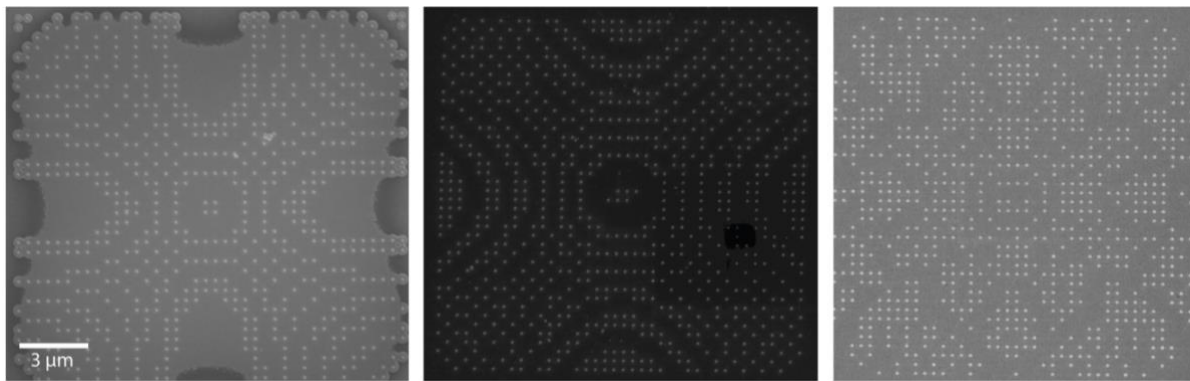


Figure A.6. Post patterns of negative tone e beam resists. Over dosed PMMA developed in (left) MIBK or (right) developed in acetone. (Center) Microchem ma-N 2401 developed in microchem ma-D 331.

surrounding the features. Outside of the developed patch, the resist would still be present.

Acetone is often used in lift-off procedures with PMMA because the unexposed regions of PMMA are soluble after they have been developed. We found that rinsing samples that had been exposed with a dose $18,000 \mu\text{C}/\text{cm}^2$ in acetone preserved the negative tone features while removing rid of unexposed resist (**Figure A.6, center**). However, these high doses require much longer write times, so we purchased a commercially available negative tone resist from Microchem. This resist allowed us to write negative tone features with doses as low as $150 \mu\text{C}/\text{cm}^2$, which shortened the entire fabrication process (**Figure A.6, right**). This advance enabled more samples to be made at a time so other parameters such as RIE time and development time could be optimized more quickly.

After negative tone resist posts were patterned by electron beam lithography, an O_2 RIE step was performed. We used 50 SCCM of O_2 with a pressure of 20 Pa under 70 W of power. Samples were etched for 3-12 s to remove residual resist in the non-developed areas. It was found

that for times longer than 10 s, the patterns were often destroyed during RIE. After RIE, 50 nm of Al was then deposited by e beam evaporation. Following Al deposition, the samples were placed in a petri dish and backfilled with 10 g of PDMS. They were allowed to sit overnight, and then were baked for 2 hours to allow the PDMS cure. The section of PDMS above the sample was cut

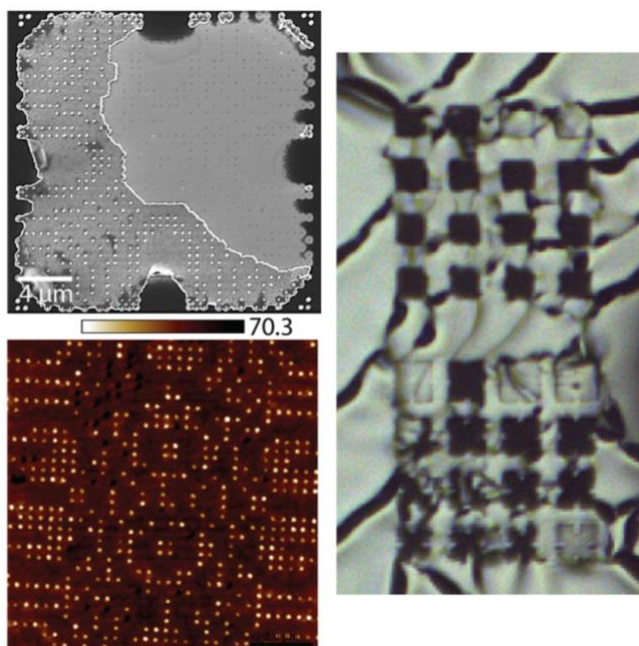


Figure A.7. (Top left) SEM showing partial transfer of Al posts on Si after backfilling with PDMS and stripping. (Right) Optical microscope image of cracked Al film on PDMS after stripping. (Bottom left) AFM of a successful pattern transfer off of the Si substrate and into PDMS

out, then stripped from the Si template. Because PDMS is non-conductive, it cannot be imaged in SEM, however, the Si template was imaged to determine if the posts were still on the Si or if they had been stripped (**Figure A.7**). The top left tile of **Figure A.7** shows an example where part of the pattern was peeled into the PDMS, although the transfer was largely incomplete. The optical microscope image in the right tile in **Figure A.7** shows a typical PDMS sample after the Si template had been stripped. Almost the entire Al thin film is transferred, but in some cases, the

area around the metasurface was not. The bottom left tile of **Figure 8** is an AFM trace of posts protruding from the PDMS after transfer. This pattern appears to have successfully transferred. Following this, the sample could be rinsed with isopropanol to remove the resist posts, and back filled with additional PDMS to encapsulate the Al NP structure.

Appendix B

Nanofrazor for Multi-Material Overlay

B.1. Aligned Multi-metallic Metasurfaces

Although the multi-metallic fabrication procedure reported in Chapter 2 is capable of generating large area structures for multi-color applications, it cannot be precisely patterned on an existing structure. E-beam lithography can achieve registration through the use of alignment markers, but even state-of-the-art registration is on the order of tens (if not hundreds) of nanometers. Thermal scanning probe lithography (t-SPL) is able to achieve alignment on the order of several nanometers through the use of real time tracking with a “read” probe to correlate with a heated “write” probe. One example where this capability may be required is for bi-metallic metalenses that can achieve wavelength dependent focusing.

Figure B.1a shows a possible Au and Al lattice optimized to focus $\lambda = 475$ nm and 650 nm light to a single focal point 5 μm above the device. To design this lens, we first simulated periodic cylindrical NPs and found that Al and Au NPs with $r = 80$ nm had resonances at $\lambda = 475$ nm and 650 nm respectively (two common diode laser wavelengths in the visible regime). We treated these two NPs as our basic units and used their electric fields with our object-oriented lattice evolutionary algorithm (OLEA)^{16, 148, 179} to generate square lattices that focused light to

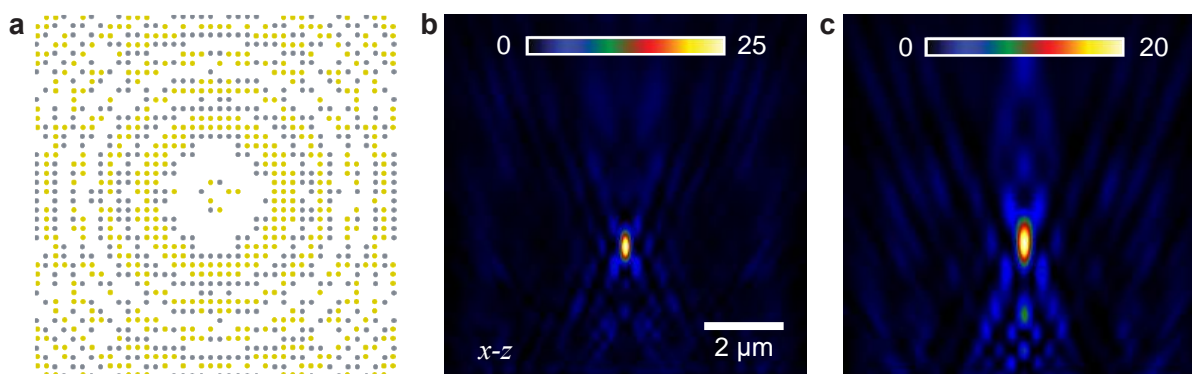


Figure B.1. Al + Au Metalens. (a) Au and Al lattice optimized by OLEA. (b) FDTD simulated electric far field intensities at $\lambda = 475$ nm and (c) 650 nm. Lens parameters: $a = 300$ nm, $t = 50$ nm, $r_{\text{Au}} = r_{\text{Al}} = 80$ nm.

programmed locations. As we can see from FDTD far field simulations shown in **Figure B.1b-c** the multi-metallic lens focuses light as predicted, with little crosstalk. The low interference between responses at each wavelength indicates that the multiple plasmonic responses resonant independent of each other and serve as an ideal platform for designing tailor-made optical components.

B.2. Fabrication of Aligned Multi-metallic Metasurfaces

Figure B.2 describes our process for realizing alignment marker-free multi-metallic structures. The M1 metasurface on a glass substrate is patterned through a standard e-beam lithography, metal deposition and liftoff procedure. The material desired for the second metasurface (M2) is then directionally deposited on top of the M1 layer. We spin on PPA, which is the thermally active resist used to define patterns by t-SPL (Nanofrazor). Before the next array (M2 metasurface) is formed, the surface of the M1/M2/PPA stack is scanned so the next pattern can be precisely aligned. Residual PPA is removed through a brief O₂ RIE plasma step, then a hard mask (we used Cu) is deposited and the PPA is lifted-off. Finally, we perform ICP-RIE to transfer the t-SPL pattern into M2 through an anisotropic etch.

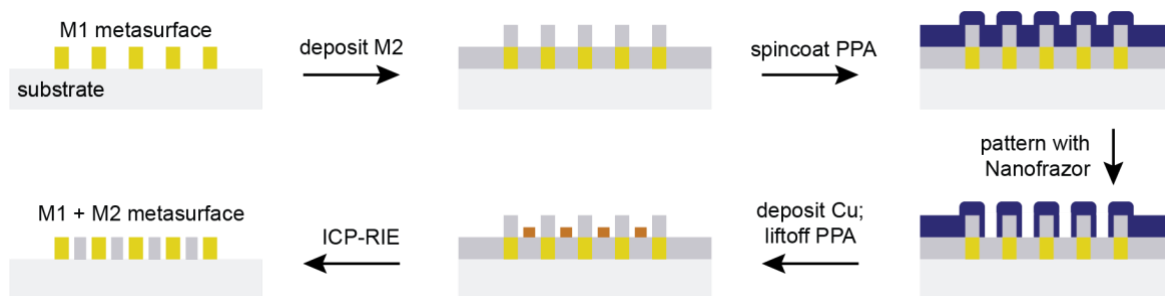


Figure B.2. Multi-metallic Metasurface Process Flow. Alignment marker-free fabrication procedure for patterning bi-metal ultrathin optical devices by Nanofrazor (t-SPL)

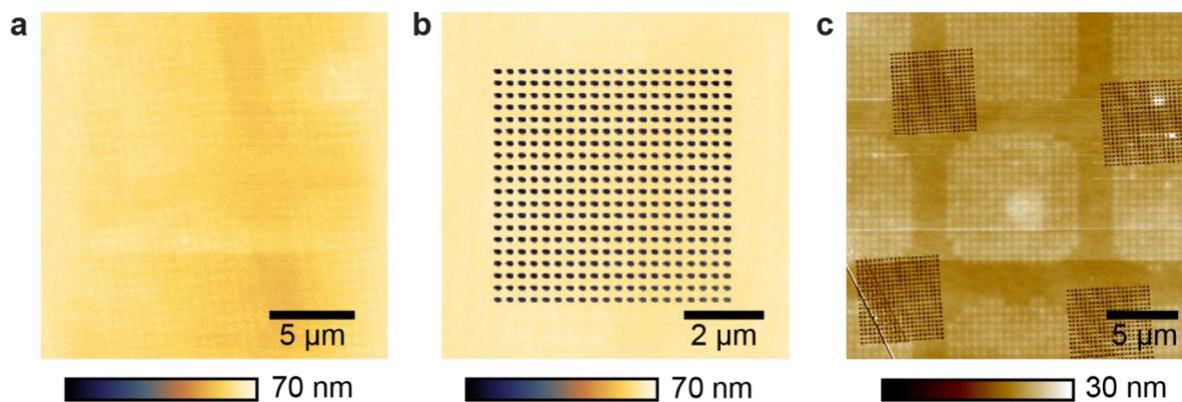


Figure B.3. Nanofrazor Overlay Patterning on Au Superlattice Arrays. (a) Scan by Nanofrazor read tip of Au structure coated in Al and PPA resist. (b) Hole array pattern overlay by Nanofrazor. (c) AFM image of grid of hole arrays patterned by Nanofrazor.

Before attempting to pattern a bi-metallic metalens, we decided to pattern a bi-metallic superlattice in order to optimize PPA etch rate, Cu mask and Al etch process. The samples consisted of Au NP superlattices (patch periodicity = 12 μm , patch width = 9 μm , NP periodicity = 600 nm, thickness = 50 nm) patterned by Odom Group graduate student Danqing Wang. 50 nm of Al was deposited by e-beam evaporation onto the Au superlattices. We spincoated PPA resist onto these samples, then patterned periodic hole arrays ($r = 80$ nm, $a = 300$ nm, $L = 6$ μm , depth = 80 nm) with the Nanofrazor. **Figure B.3a.** that scans by the Nanofrazor read tip can resolve nanoscale lateral features, even when the initial 50 nm tall Au NPs are covered in 50 nm of Al and approximately 100 nm of PPA. While the cylindrical posts have rounded and become much shorter, the Nanofrazor read tip has nanometer scale sensitivity, similar to an AFM cantilever. **Figure B.3b.** shows a Nanofrazor scan taken directly after writing an array of holes on an uneven surface. The micro-second feedback loop built into the Nanofrazor allows it to correct for surface variation on-the-fly, and form resist holes of consistent depths. The Nanofrazor software takes note of where it has recently scanned and etched, so we can specify locations of new patterns relative to pre-existing designs. **Figure B.3c** shows we can take advantage of the footprint view to generate

a grid of resist holes across a large area. Besides having consistent hole depths in a single write sequence, consecutive patterning steps also have consistent hole depths, independent of their underlying roughness.

Because the holes patterned by t-SPL do not completely remove all of the PPA between the tip and the underlying material, we characterized the PPA etch rate. We spun PPA onto Si wafers and treated them with O₂ RIE. To test the etch depth (d), we measured the thickness of PPA film by ellipsometry after each RIE step (t). We found that the etch rate of PPA by O₂ RIE follows a linear trend of 2.2 nm/s (**Figure B.4**).

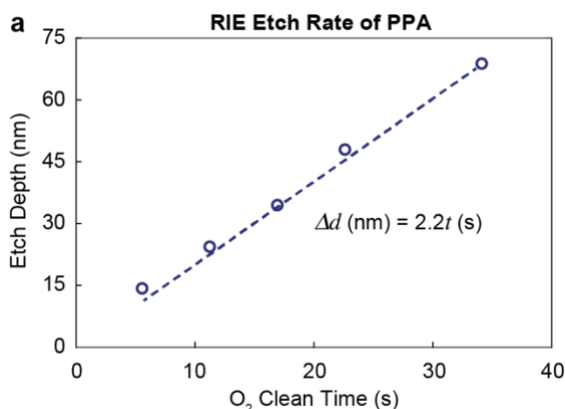


Figure B.4. PPA Etch. (a) Plot of the thickness of PPA etched versus O₂ RIE time.

Figure B.5a shows we are able to align Nanofrazor patterned holes to the gaps between patches in a superlattice array. The PPA features have $a = 300$ nm & $r = 50$ nm and are approximately 50 nm deep. The holes have fairly uniform contrast in the SEM, indicating that they are of similar depth. **Figure B.5b** shows that after PPA thinning by RIE, Cu deposition and PPA liftoff, we were able to translate Nanofrazor patterns into a Cu hard mask on the Al film. The Cu disk array is incomplete, likely due to slight variation in the PPA hole depth patterned by the Nanofrazor. In the future, we will slightly increase the RIE clean time to over etch the PPA and expose more of

the underlying Al. We may also need to shrink the initial size of the Nanofrazor holes to compensate for any increase in diameter due to the isotropic O₂ RIE step. **Figure B.5c** shows that

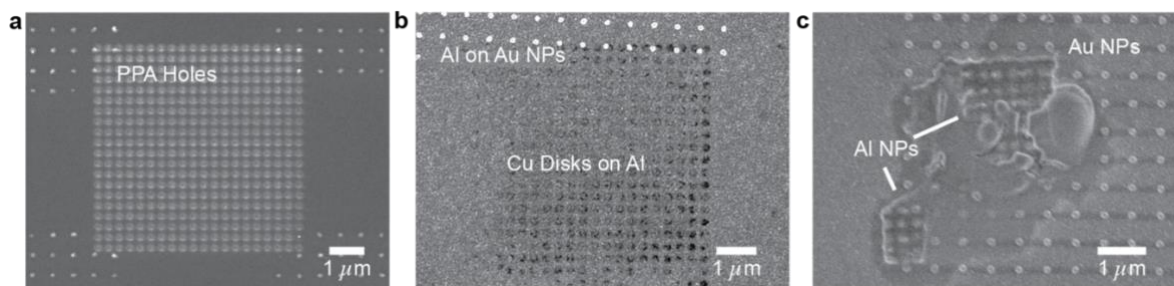


Figure B.5. Fabricating Al-Au Nanostructures. SEM images of (a) a PPA hole array patch patterned by Nanofrazor on a Au NP superlattice substrate coated in Al and PPA. The patch consists of 50 x 50 holes with $d = 80$ nm and $a = 300$ nm. (b) The same sample after 15 nm of Cu deposition and liftoff in acetone. (c) The same sample after ICP-RIE etch of Al and Cu removal.

ICP-RIE is able to transfer the Cu mask into the Al film to produce an Al NP array interleaved in a Au NP superlattice patch. The Al NP array is significantly damaged because of the issues with the Cu mask previously stated. Further optimization is needed for the PPA etch time before we can realize reliable multi-metallic metasurfaces.

The simulated architecture shown in Figure B.1 has traditionally been technologically difficult to realize due to the nanoscale spatial alignment required to place multiple metals in the same layer. With e-beam lithography, we approximate that we could approach 50 nm spatial registration by fabricating large alignment markers with the Au layer. However, the Nanofrazor Explore is able to overlay a new resist pattern over an existing structure with less than 10 nm spatial error, without using alignment markers. **Figure B.6a** confirms that the 50 nm tall Au metalens layer coated in 50 nm of Al and approximately 100 nm of PPA can be detected by the read tip of the Nanofrazor. We also observe that the topology of the features is less pronounced than the original 50 nm thick Au device, which we expected to occur after Al and PPA deposition.

Figure B.6b shows that we can accurately pattern resist holes with uniform depth and diameter to our desired locations by using the Nanofrazor. The underlying topology does not significantly interfere with resist patterning, and by scanning an area first, we can precisely pattern on top of existing structures.

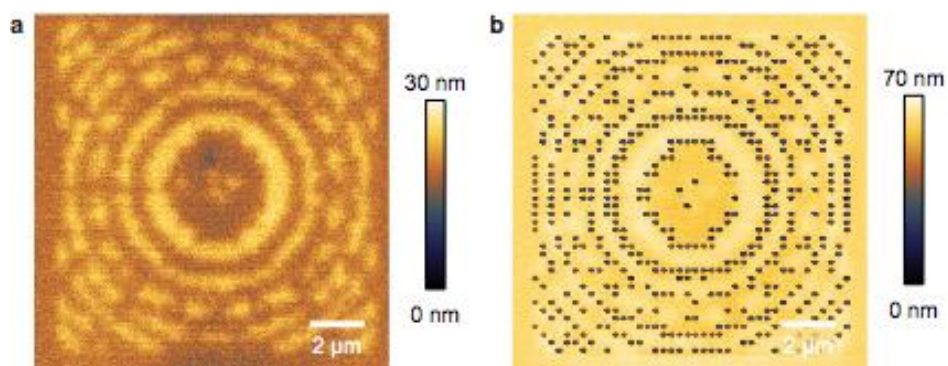


Figure B.6. Nanofrazor Metalens Overlay. (a) Nanofrazor scan of Au metalens coated in Al and PPA resist. (b) Nanofrazor scan after writing hole pattern that will become Al NPs in final metalens.

REFERENCES

1. Atwater, H. A.; Polman, A., Plasmonics for improved photovoltaic devices. In *Materials for Sustainable Energy*, Co-Published with Macmillan Publishers Ltd, UK: 2010; pp 1-11.
2. Pillai, S. a.; Green, M., Plasmonics for photovoltaic applications. *Solar Energy Materials and Solar Cells* **2010**, *94* (9), 1481-1486.
3. Li, W.; Guler, U.; Kinsey, N.; Naik, G. V.; Boltasseva, A.; Guan, J.; Shalaev, V. M.; Kildishev, A. V., Refractory Plasmonics with Titanium Nitride: Broadband Metamaterial Absorber. *Advanced Materials* **2014**, *26* (47), 7959-7965.
4. Beck, F.; Polman, A.; Catchpole, K., Tunable light trapping for solar cells using localized surface plasmons. *Journal of Applied Physics* **2009**, *105* (11), 114310.
5. Yang, Y.; Pillai, S.; Mehrvarz, H.; Green, M. A., Plasmonic degradation and the importance of over-coating metal nanoparticles for a plasmonic solar cell. *Solar Energy Materials and Solar Cells* **2014**, *122*, 208-216.
6. Naldoni, A.; Guler, U.; Wang, Z.; Marelli, M.; Malara, F.; Meng, X.; Besteiro, L. V.; Govorov, A. O.; Kildishev, A. V.; Boltasseva, A.; Shalaev, V. M., Broadband Hot-Electron Collection for Solar Water Splitting with Plasmonic Titanium Nitride. *Advanced Optical Materials* **2017**, *5* (15), 1601031.
7. Pang, L.; Hwang, G. M.; Slutsky, B.; Fainman, Y., Spectral sensitivity of two-dimensional nanohole array surface plasmon polariton resonance sensor. *Applied Physics Letters* **2007**, *91* (12), 123112.
8. Stewart, M. E.; Anderton, C. R.; Thompson, L. B.; Maria, J.; Gray, S. K.; Rogers, J. A.; Nuzzo, R. G., Nanostructured Plasmonic Sensors. *Chemical Reviews* **2008**, *108* (2), 494-521.
9. El-Sayed, I. H.; Huang, X.; El-Sayed, M. A., Surface plasmon resonance scattering and absorption of anti-EGFR antibody conjugated gold nanoparticles in cancer diagnostics: applications in oral cancer. *Nano letters* **2005**, *5* (5), 829-834.
10. Gagner, J. E.; Kim, W.; Chaikof, E. L., Designing protein-based biomaterials for medical applications. *Acta Biomaterialia* **2014**, *10* (4), 1542-1557.
11. Kah, J. C. Y.; Kho, K. W.; Lee, C. G. L.; Richard, C. J., Early diagnosis of oral cancer based on the surface plasmon resonance of gold nanoparticles. *International journal of nanomedicine* **2007**, *2* (4), 785.
12. Mallidi, S.; Larson, T.; Tam, J.; Joshi, P. P.; Karpiouk, A.; Sokolov, K.; Emelianov, S., Multiwavelength photoacoustic imaging and plasmon resonance coupling of gold nanoparticles for selective detection of cancer. *Nano letters* **2009**, *9* (8), 2825-2831.
13. Gao, H.; Hyun, J. K.; Lee, M. H.; Yang, J. C.; Lauhon, L. J.; Odom, T. W., Broadband plasmonic microlenses based on patches of nanoholes. *Nano Lett* **2010**, *10* (10), 4111-6.
14. Aieta, F.; Genevet, P.; Kats, M. A.; Yu, N.; Blanchard, R.; Gaburro, Z.; Capasso, F., Aberration-free ultrathin flat lenses and axicons at telecom wavelengths based on plasmonic metasurfaces. *Nano Lett* **2012**, *12* (9), 4932-6.
15. Ni, X.; Ishii, S.; Kildishev, A. V.; Shalaev, V. M., Ultra-thin, planar, Babinet-inverted plasmonic metalenses. *Light: Science & Applications* **2013**, *2* (4), e72-e72.

16. Hu, J.; Liu, C.-H.; Ren, X.; Lauhon, L. J.; Odom, T. W., Plasmonic Lattice Lenses for Multiwavelength Achromatic Focusing. *ACS Nano* **2016**, *10* (11), 10275-10282.
17. Xian, Y.; Cai, Y.; Sun, X.; Liu, X.; Guo, Q.; Zhang, Z.; Tong, L.; Qiu, J., Refractory Plasmonic Metal Nitride Nanoparticles for Broadband Near-Infrared Optical Switches. *Laser & Photonics Reviews* **2019**, *13* (6), 1900029.
18. Paul, S.; Ray, M., Multispectral Switching Using Fano Resonance and Plasmon-Induced Transparency in a Plasmonic Waveguide-Coupled Resonator System. *Plasmonics* **2019**, *14* (5), 1113-1122.
19. Hutter, E.; Fendler, J. H., Exploitation of Localized Surface Plasmon Resonance. *Advanced Materials* **2004**, *16* (19), 1685-1706.
20. Willets, K. A.; Van Duyne, R. P., Localized surface plasmon resonance spectroscopy and sensing. *Annu. Rev. Phys. Chem.* **2007**, *58*, 267-297.
21. Mayer, K. M.; Hafner, J. H., Localized surface plasmon resonance sensors. *Chemical reviews* **2011**, *111* (6), 3828-3857.
22. West, P. R.; Ishii, S.; Naik, G. V.; Emani, N. K.; Shalaev, V. M.; Boltasseva, A., Searching for better plasmonic materials. *Laser & Photonics Reviews* **2010**, *4* (6), 795-808.
23. Naik, G. V.; Kim, J.; Boltasseva, A., Oxides and nitrides as alternative plasmonic materials in the optical range [Invited]. *Opt. Mater. Express* **2011**, *1* (6), 1090-1099.
24. Naik, G. V.; Shalaev, V. M.; Boltasseva, A., Alternative Plasmonic Materials: Beyond Gold and Silver. *Advanced Materials* **2013**, *25* (24), 3264-3294.
25. McMahon, J. M.; Schatz, G. C.; Gray, S. K., Plasmonics in the ultraviolet with the poor metals Al, Ga, In, Sn, Tl, Pb, and Bi. *Physical Chemistry Chemical Physics* **2013**, *15* (15), 5415-5423.
26. Kelly, K. L.; Coronado, E.; Zhao, L. L.; Schatz, G. C., The optical properties of metal nanoparticles: the influence of size, shape, and dielectric environment. ACS Publications: 2003.
27. Zhou, F.; Li, Z.-Y.; Liu, Y.; Xia, Y., Quantitative analysis of dipole and quadrupole excitation in the surface plasmon resonance of metal nanoparticles. *The Journal of Physical Chemistry C* **2008**, *112* (51), 20233-20240.
28. Li, Z.; Yu, Y.; Chen, Z.; Liu, T.; Zhou, Z.-K.; Han, J.-B.; Li, J.; Jin, C.; Wang, X., Ultrafast third-order optical nonlinearity in Au triangular nanoprism with strong dipole and quadrupole plasmon resonance. *The Journal of Physical Chemistry C* **2013**, *117* (39), 20127-20132.
29. Tsuei, K.-D.; Plummer, E.; Liebsch, A.; Kempa, K.; Bakshi, P., Multipole plasmon modes at a metal surface. *Physical review letters* **1990**, *64* (1), 44.
30. Raza, S.; Kadkhodazadeh, S.; Christensen, T.; Di Vece, M.; Wubs, M.; Mortensen, N. A.; Stenger, N., Multipole plasmons and their disappearance in few-nanometre silver nanoparticles. *Nature communications* **2015**, *6* (1), 1-9.
31. Wiley, B. J.; Im, S. H.; Li, Z.-Y.; McLellan, J.; Siekkinen, A.; Xia, Y., Maneuvering the surface plasmon resonance of silver nanostructures through shape-controlled synthesis. ACS Publications: 2006.
32. Zhang, J.; Liu, H.; Wang, Z.; Ming, N., Shape-selective synthesis of gold nanoparticles with controlled sizes, shapes, and plasmon resonances. *Advanced Functional Materials* **2007**, *17* (16), 3295-3303.
33. Cobby, C. M.; Skrabalak, S. E.; Campbell, D. J.; Xia, Y., Shape-controlled synthesis of silver nanoparticles for plasmonic and sensing applications. *Plasmonics* **2009**, *4* (2), 171-179.

34. Khalavka, Y.; Becker, J.; Sonnichsen, C., Synthesis of rod-shaped gold nanorattles with improved plasmon sensitivity and catalytic activity. *Journal of the American Chemical Society* **2009**, *131* (5), 1871-1875.
35. Liu, S.; Chen, G.; Prasad, P. N.; Swihart, M. T., Synthesis of monodisperse Au, Ag, and Au–Ag alloy nanoparticles with tunable size and surface plasmon resonance frequency. *Chemistry of Materials* **2011**, *23* (18), 4098-4101.
36. Auguie, B.; Barnes, W. L., Collective Resonances in Gold Nanoparticle Arrays. *Physical Review Letters* **2008**, *101* (14), 143902.
37. Kravets, V. G.; Kabashin, A. V.; Barnes, W. L.; Grigorenko, A. N., Plasmonic Surface Lattice Resonances: A Review of Properties and Applications. *Chemical Reviews* **2018**, *118* (12), 5912-5951.
38. Zou, S.; Janel, N.; Schatz, G. C., Silver nanoparticle array structures that produce remarkably narrow plasmon lineshapes. *The Journal of chemical physics* **2004**, *120* (23), 10871-10875.
39. Hicks, E. M.; Zou, S.; Schatz, G. C.; Spears, K. G.; Van Duyne, R. P.; Gunnarsson, L.; Rindzevicius, T.; Kasemo, B.; Käll, M., Controlling Plasmon Line Shapes through Diffractive Coupling in Linear Arrays of Cylindrical Nanoparticles Fabricated by Electron Beam Lithography. *Nano Letters* **2005**, *5* (6), 1065-1070.
40. Kravets, V.; Schedin, F.; Grigorenko, A. J. P. r. l., Extremely narrow plasmon resonances based on diffraction coupling of localized plasmons in arrays of metallic nanoparticles. **2008**, *101* (8), 087403.
41. Chu, Y.; Schonbrun, E.; Yang, T.; Crozier, K. B. J. A. P. L., Experimental observation of narrow surface plasmon resonances in gold nanoparticle arrays. **2008**, *93* (18), 181108.
42. Thackray, B. D.; Kravets, V. G.; Schedin, F.; Auton, G.; Thomas, P. A.; Grigorenko, A. N., Narrow collective plasmon resonances in nanostructure arrays observed at normal light incidence for simplified sensing in asymmetric air and water environments. *ACS Photonics* **2014**, *1* (11), 1116-1126.
43. Danilov, A.; Tselikov, G.; Wu, F.; Kravets, V. G.; Ozerov, I.; Bedu, F.; Grigorenko, A. N.; Kabashin, A. V., Ultra-narrow surface lattice resonances in plasmonic metamaterial arrays for biosensing applications. *Biosensors and Bioelectronics* **2018**, *104*, 102-112.
44. Deng, S.; Zhang, B.; Choo, P.; Smeets, P. J. M.; Odom, T. W., Plasmonic Photoelectrocatalysis in Copper–Platinum Core–Shell Nanoparticle Lattices. *Nano Letters* **2021**, *21* (3), 1523-1529.
45. Hakala, T. K.; Moilanen, A. J.; Väkeväinen, A. I.; Guo, R.; Martikainen, J.-P.; Daskalakis, K. S.; Rekola, H. T.; Julku, A.; Törmä, P., Bose–Einstein condensation in a plasmonic lattice. *Nature Physics* **2018**, *14* (7), 739-744.
46. Väkeväinen, A. I.; Moerland, R. J.; Rekola, H. T.; Eskelinen, A. P.; Martikainen, J. P.; Kim, D. H.; Törmä, P., Plasmonic Surface Lattice Resonances at the Strong Coupling Regime. *Nano Letters* **2014**, *14* (4), 1721-1727.
47. Zhou, W.; Dridi, M.; Suh, J. Y.; Kim, C. H.; Co, D. T.; Wasielewski, M. R.; Schatz, G. C.; Odom, T. W., Lasing action in strongly coupled plasmonic nanocavity arrays. *Nat Nanotechnol* **2013**, *8* (7), 506-11.
48. Yang, A.; Hoang, T. B.; Dridi, M.; Deeb, C.; Mikkelsen, M. H.; Schatz, G. C.; Odom, T. W., Real-time tunable lasing from plasmonic nanocavity arrays. *Nat Commun* **2015**, *6*, 6939.

49. Ma, R.-M.; Oulton, R. F., Applications of nanolasers. *Nature Nanotechnology* **2019**, *14* (1), 12-22.
50. Pease, R. F. W., Electron beam lithography. *Contemporary Physics* **1981**, *22* (3), 265-290.
51. Vieu, C.; Carcenac, F.; Pépin, A.; Chen, Y.; Mejias, M.; Lebib, A.; Manin-Ferlazzo, L.; Couraud, L.; Launois, H., Electron beam lithography: resolution limits and applications. *Applied Surface Science* **2000**, *164* (1), 111-117.
52. Tseng, A. A.; Kuan, C.; Chen, C. D.; Ma, K. J., Electron beam lithography in nanoscale fabrication: recent development. *IEEE Transactions on Electronics Packaging Manufacturing* **2003**, *26* (2), 141-149.
53. Garcia, R.; Knoll, A. W.; Riedo, E., Advanced scanning probe lithography. *Nature Nanotechnology* **2014**, *9* (8), 577-587.
54. Wolf, H.; Rawlings, C.; Mensch, P.; Hedrick, J. L.; Coady, D. J.; Duerig, U.; Knoll, A. W., Sub-20 nm silicon patterning and metal lift-off using thermal scanning probe lithography. *Journal of Vacuum Science & Technology B* **2015**, *33* (2), 02B102.
55. Ryu Cho, Y. K.; Rawlings, C. D.; Wolf, H.; Spieser, M.; Bisig, S.; Reidt, S.; Sousa, M.; Khanal, S. R.; Jacobs, T. D. B.; Knoll, A. W., Sub-10 Nanometer Feature Size in Silicon Using Thermal Scanning Probe Lithography. *ACS Nano* **2017**, *11* (12), 11890-11897.
56. Sewell, H., Immersion photolithography system and method using inverted wafer-projection optics interface. Google Patents: 2005.
57. Vogel, H.; Simon, K.; Derksen, A. T. A. M., Immersion photolithography system and method using microchannel nozzles. Google Patents: 2005.
58. Tran, L.; Rericha, W. T.; Lee, J.; Alapati, R.; Honarkhah, S.; Meng, S.; Sharma, P.; Bai, J. J.; Yin, Z.; Morgan, P., Pitch reduced patterns relative to photolithography features. Google Patents: 2007.
59. Lee, M. H.; Huntington, M. D.; Zhou, W.; Yang, J.-C.; Odom, T. W., Programmable Soft Lithography: Solvent-Assisted Nanoscale Embossing. *Nano Letters* **2011**, *11* (2), 311-315.
60. Amsden, J. J.; Domachuk, P.; Gopinath, A.; White, R. D.; Negro, L. D.; Kaplan, D. L.; Omenetto, F. G., Rapid Nanoimprinting of Silk Fibroin Films for Biophotonic Applications. *Advanced Materials* **2010**, *22* (15), 1746-1749.
61. Chen, W.; Tymchenko, M.; Gopalan, P.; Ye, X.; Wu, Y.; Zhang, M.; Murray, C. B.; Alu, A.; Kagan, C. R., Large-Area Nanoimprinted Colloidal Au Nanocrystal-Based Nanoantennas for Ultrathin Polarizing Plasmonic Metasurfaces. *Nano Letters* **2015**, *15* (8), 5254-5260.
62. Murai, S.; Fujita, K.; Daido, Y.; Yasuhara, R.; Kamakura, R.; Tanaka, K., Plasmonic arrays of titanium nitride nanoparticles fabricated from epitaxial thin films. *Opt Express* **2016**, *24* (2), 1143-53.
63. Alvarez-Puebla, R.; Cui, B.; Bravo-Vasquez, J.-P.; Veres, T.; Fenniri, H., Nanoimprinted SERS-active substrates with tunable surface plasmon resonances. *The Journal of Physical Chemistry C* **2007**, *111* (18), 6720-6723.
64. Boltasseva, A., Plasmonic components fabrication via nanoimprint. *Journal of Optics A: Pure and Applied Optics* **2009**, *11* (11), 114001.
65. Bardwell, J. A.; Foulds, I. G.; Webb, J. B.; Tang, H.; Fraser, J.; Moisa, S.; Rolfe, S., A simple wet etch for GaN. *Journal of electronic materials* **1999**, *28* (10), L24-L26.
66. Love, J. C.; Paul, K. E.; Whitesides, G. M., Fabrication of Nanometer-Scale Features by Controlled Isotropic Wet Chemical Etching. *Advanced Materials* **2001**, *13* (8), 604-607.

67. Albero, J.; Nieradko, L.; Gorecki, C.; Ottevaere, H.; Gomez, V.; Thienpont, H.; Pietarinen, J.; Päivänranta, B.; Passilly, N., Fabrication of spherical microlenses by a combination of isotropic wet etching of silicon and molding techniques. *Opt. Express* **2009**, *17* (8), 6283-6292.
68. Schwartz, G.; Schaible, P., Reactive ion etching of copper films. *J. Electrochem. Soc* **1983**, *130* (8), 1777-1779.
69. Foad, M.; Wilkinson, C.; Dunscomb, C.; Williams, R., CH₄/H₂: A universal reactive ion etch for II-VI semiconductors? *Applied physics letters* **1992**, *60* (20), 2531-2533.
70. Jansen, H.; Gardeniers, H.; de Boer, M.; Elwenspoek, M.; Fluitman, J., A survey on the reactive ion etching of silicon in microtechnology. *Journal of micromechanics and microengineering* **1996**, *6* (1), 14.
71. Laerme, F.; Schilp, A.; Funk, K.; Offenber, M. In *Bosch deep silicon etching: improving uniformity and etch rate for advanced MEMS applications*, Technical Digest. IEEE International MEMS 99 Conference. Twelfth IEEE International Conference on Micro Electro Mechanical Systems (Cat. No. 99CH36291), IEEE: 1999; pp 211-216.
72. Shul, R.; McClellan, G.; Casalnuovo, S.; Rieger, D.; Pearton, S.; Constantine, C.; Barratt, C.; Karlicek Jr, R.; Tran, C.; Schurman, M., Inductively coupled plasma etching of GaN. *Applied physics letters* **1996**, *69* (8), 1119-1121.
73. Totonani, J.; Iwamoto, T.; Sato, F.; Hattori, K.; Ohmi, S.; Iwai, H., Dry etching characteristics of TiN film using Ar/CHF₃, Ar/Cl₂, and Ar/BCl₃ gas chemistries in an inductively coupled plasma. *Journal of Vacuum Science & Technology B: Microelectronics and Nanometer Structures* **2003**, *21* (5).
74. Lee Sang, B.; Gour, M.-J.; Darnon, M.; Ecoffey, S.; Jaouad, A.; Sadani, B.; Drouin, D.; Souifi, A., Selective dry etching of TiN nanostructures over SiO₂ nanotrenches using a Cl₂/Ar/N₂ inductively coupled plasma. *Journal of Vacuum Science & Technology B, Nanotechnology and Microelectronics: Materials, Processing, Measurement, and Phenomena* **2016**, *34* (2).
75. MacDonald, K. F.; Sámson, Z. L.; Stockman, M. I.; Zheludev, N. I., Ultrafast active plasmonics. *Nature Photonics* **2009**, *3* (1), 55-58.
76. Dhakshinamoorthy, A.; Garcia, H., Catalysis by metal nanoparticles embedded on metal-organic frameworks. *Chemical Society reviews* **2012**, *41* (15), 5262-84.
77. Liu, J.; Wang, W.; Wang, D.; Hu, J.; Ding, W.; Schaller, R. D.; Schatz, G. C.; Odom, T. W., Spatially defined molecular emitters coupled to plasmonic nanoparticle arrays. *Proceedings of the National Academy of Sciences* **2019**, *116* (13), 5925-5930.
78. Tran, T. T.; Wang, D.; Xu, Z.-Q.; Yang, A.; Toth, M.; Odom, T. W.; Aharonovich, I., Deterministic Coupling of Quantum Emitters in 2D Materials to Plasmonic Nanocavity Arrays. *Nano Letters* **2017**, *17* (4), 2634-2639.
79. Deng, S.; Li, R.; Park, J.-E.; Guan, J.; Choo, P.; Hu, J.; Smeets, P. J. M.; Odom, T. W., Ultranarrow plasmon resonances from annealed nanoparticle lattices. *Proceedings of the National Academy of Sciences* **2020**, *117* (38), 23380-23384.
80. Tsuboi, Y.; Shimizu, R.; Shoji, T.; Kitamura, N., Near-infrared continuous-wave light driving a two-photon photochromic reaction with the assistance of localized surface plasmon. *Journal of the American Chemical Society* **2009**, *131* (35), 12623-12627.
81. Lenyk, B.; Schöps, V.; Boneberg, J.; Kabdulov, M.; Huhn, T.; Scheer, E.; Offenhäusser, A.; Mayer, D., Surface Plasmon-Enhanced Switching Kinetics of Molecular Photochromic Films on Gold Nanohole Arrays. *Nano Letters* **2020**, *20* (7), 5243-5250.

82. Kim, J.; Son, H.; Cho, D. J.; Geng, B.; Regan, W.; Shi, S.; Kim, K.; Zettl, A.; Shen, Y.-R.; Wang, F., Electrical Control of Optical Plasmon Resonance with Graphene. *Nano Letters* **2012**, *12* (11), 5598-5602.
83. Yao, Y.; Shankar, R.; Kats, M. A.; Song, Y.; Kong, J.; Loncar, M.; Capasso, F., Electrically Tunable Metasurface Perfect Absorbers for Ultrathin Mid-Infrared Optical Modulators. *Nano Letters* **2014**, *14* (11), 6526-6532.
84. Ee, H. S.; Agarwal, R., Tunable Metasurface and Flat Optical Zoom Lens on a Stretchable Substrate. *Nano Lett* **2016**, *16* (4), 2818-23.
85. Wang, D.; Bourgeois, M. R.; Lee, W.-K.; Li, R.; Trivedi, D.; Knudson, M. P.; Wang, W.; Schatz, G. C.; Odom, T. W., Stretchable Nanolasing from Hybrid Quadrupole Plasmons. *Nano Letters* **2018**, *18* (7), 4549-4555.
86. Pae, J. Y.; Medwal, R.; Nair, R. V.; Chaurasiya, A.; Battiato, M.; Rawat, R. S.; Matham, M. V., Electro-Ionic Control of Surface Plasmons in Graphene-Layered Heterostructures. *Nano Letters* **2020**, *20* (11), 8305-8311.
87. Jiao, Z.; Xia, H.; Tao, X., Modulation of Localized Surface Plasmon Resonance of Nanostructured Gold Crystals by Tuning Their Tip Curvature with Assistance of Iodide and Silver(I) Ions. *The Journal of Physical Chemistry C* **2011**, *115* (16), 7887-7895.
88. Guo, P.; Schaller, R. D.; Ketterson, J. B.; Chang, R. P. H., Ultrafast switching of tunable infrared plasmons in indium tin oxide nanorod arrays with large absolute amplitude. *Nature Photonics* **2016**, *10*, 267.
89. Wang, W.; Watkins, N.; Yang, A.; Schaller, R. D.; Schatz, G. C.; Odom, T. W., Ultrafast Dynamics of Lattice Plasmon Lasers. *The Journal of Physical Chemistry Letters* **2019**, *10* (12), 3301-3306.
90. Logunov, S. L.; Ahmadi, T. S.; El-Sayed, M. A.; Khoury, J. T.; Whetten, R. L., Electron Dynamics of Passivated Gold Nanocrystals Probed by Subpicosecond Transient Absorption Spectroscopy. *The Journal of Physical Chemistry B* **1997**, *101* (19), 3713-3719.
91. Link, S.; Burda, C.; Mohamed, M. B.; Nikoobakht, B.; El-Sayed, M. A., Femtosecond transient-absorption dynamics of colloidal gold nanorods: Shape independence of the electron-phonon relaxation time. *Physical Review B* **2000**, *61* (9), 6086-6090.
92. Yu, K.; Polavarapu, L.; Xu, Q.-H., Excitation Wavelength and Fluence Dependent Femtosecond Transient Absorption Studies on Electron Dynamics of Gold Nanorods. *The Journal of Physical Chemistry A* **2011**, *115* (16), 3820-3826.
93. Zhou, M.; Long, S.; Wan, X.; Li, Y.; Niu, Y.; Guo, Q.; Wang, Q.-M.; Xia, A., Ultrafast relaxation dynamics of phosphine-protected, rod-shaped Au₂₀ clusters: interplay between solvation and surface trapping. *Physical Chemistry Chemical Physics* **2014**, *16* (34), 18288-18293.
94. Scotognella, F.; Della Valle, G.; Srimath Kandada, A. R.; Zavelani-Rossi, M.; Longhi, S.; Lanzani, G.; Tassone, F., Plasmonics in heavily-doped semiconductor nanocrystals. *The European Physical Journal B* **2013**, *86* (4), 154.
95. Doiron, B.; Li, Y.; Mihai, A. P.; Cohen, L. F.; Petrov, P. K.; Alford, N. M.; Oulton, R. F.; Maier, S. A., *Comparison of the ultrafast hot electron dynamics of titanium nitride and gold for plasmonic applications*. SPIE: 2017; Vol. 10346, p 5.
96. Li, R.; Wang, D.; Guan, J.; Wang, W.; Ao, X.; Schatz, G. C.; Schaller, R.; Odom, T. W., Plasmon nanolasing with aluminum nanoparticle arrays [Invited]. *J. Opt. Soc. Am. B* **2019**, *36* (7), E104-E111.

97. Hoang, T. B.; Akselrod, G. M.; Yang, A.; Odom, T. W.; Mikkelsen, M. H., Millimeter-Scale Spatial Coherence from a Plasmon Laser. *Nano Letters* **2017**, *17* (11), 6690-6695.
98. Li, R.; Bourgeois, M. R.; Cherqui, C.; Guan, J.; Wang, D.; Hu, J.; Schaller, R. D.; Schatz, G. C.; Odom, T. W., Hierarchical Hybridization in Plasmonic Honeycomb Lattices. *Nano Letters* **2019**, *19* (9), 6435-6441.
99. Lin, Y.; Wang, D.; Hu, J.; Liu, J.; Wang, W.; Guan, J.; Schaller, R. D.; Odom, T. W., Engineering Symmetry-Breaking Nanocrescent Arrays for Nanolasing. *Advanced Functional Materials* **2019**, *29* (42), 1904157.
100. Fernandez-Bravo, A.; Wang, D.; Barnard, E. S.; Teitelboim, A.; Tajon, C.; Guan, J.; Schatz, G. C.; Cohen, B. E.; Chan, E. M.; Schuck, P. J., Ultralow-threshold, continuous-wave upconverting lasing from subwavelength plasmons. *Nature materials* **2019**, *18* (11), 1172-1176.
101. Knudson, M. P.; Li, R.; Wang, D.; Wang, W.; Schaller, R. D.; Odom, T. W., Polarization-Dependent Lasing Behavior from Low-Symmetry Nanocavity Arrays. *ACS Nano* **2019**, *13* (7), 7435-7441.
102. Wang, D.; Yang, A.; Wang, W.; Hua, Y.; Schaller, R. D.; Schatz, G. C.; Odom, T. W., Band-edge engineering for controlled multi-modal nanolasing in plasmonic superlattices. *Nature Nanotechnology* **2017**, *12*, 889.
103. Winkler, J. M.; Ruckriegel, M. J.; Rojo, H.; Keitel, R. C.; De Leo, E.; Rabouw, F. T.; Norris, D. J., Dual-wavelength lasing in quantum-dot plasmonic lattice lasers. *ACS nano* **2020**, *14* (5), 5223-5232.
104. Yang, A.; Hryn, A. J.; Bourgeois, M. R.; Lee, W.-K.; Hu, J.; Schatz, G. C.; Odom, T. W., Programmable and reversible plasmon mode engineering. *Proceedings of the National Academy of Sciences* **2016**, *113* (50), 14201-14206.
105. Yoo, D.; Johnson, T. W.; Cherukulappurath, S.; Norris, D. J.; Oh, S.-H., Template-Stripped Tunable Plasmonic Devices on Stretchable and Rollable Substrates. *ACS Nano* **2015**, *9* (11), 10647-10654.
106. Malek, S. C.; Ee, H.-S.; Agarwal, R., Strain Multiplexed Metasurface Holograms on a Stretchable Substrate. *Nano Letters* **2017**, *17* (6), 3641-3645.
107. Qiu, Y.; Park, K., Environment-sensitive hydrogels for drug delivery. *Advanced Drug Delivery Reviews* **2001**, *53* (3), 321-339.
108. Hoffman, A. S., Hydrogels for biomedical applications. *Advanced Drug Delivery Reviews* **2012**, *64*, 18-23.
109. Zhang, Y. S.; Khademhosseini, A., Advances in engineering hydrogels. *Science* **2017**, *356* (6337), eaaf3627.
110. Tsioris, K.; Raja, W. K.; Pritchard, E. M.; Panilaitis, B.; Kaplan, D. L.; Omenetto, F. G., Fabrication of Silk Microneedles for Controlled-Release Drug Delivery. *Advanced Functional Materials* **2012**, *22* (2), 330-335.
111. Wang, Z.; Zhang, Y.; Zhang, J.; Huang, L.; Liu, J.; Li, Y.; Zhang, G.; Kundu, S. C.; Wang, L., Exploring natural silk protein sericin for regenerative medicine: an injectable, photoluminescent, cell-adhesive 3D hydrogel. *Scientific Reports* **2014**, *4* (1), 7064.
112. Ding, D.; Guerette, P. A.; Fu, J.; Zhang, L.; Irvine, S. A.; Miserez, A., From Soft Self-Healing Gels to Stiff Films in Suckerin-Based Materials Through Modulation of Crosslink Density and β -Sheet Content. *Advanced Materials* **2015**, *27* (26), 3953-3961.

113. Wu, J.; Li, P.; Dong, C.; Jiang, H.; Bin, X.; Gao, X.; Qin, M.; Wang, W.; Bin, C.; Cao, Y., Rationally designed synthetic protein hydrogels with predictable mechanical properties. *Nature Communications* **2018**, *9* (1), 620.
114. Buck, C. C.; Dennis, P. B.; Gupta, M. K.; Grant, M. T.; Crosby, M. G.; Slocik, J. M.; Mirau, P. A.; Becknell, K. A.; Comfort, K. K.; Naik, R. R., Anion-Mediated Effects on the Size and Mechanical Properties of Enzymatically Crosslinked Suckerin Hydrogels. *Macromolecular Bioscience* **2019**, *19* (3), 1800238.
115. Lawrence, B. D.; Cronin-Golomb, M.; Georgakoudi, I.; Kaplan, D. L.; Omenetto, F. G., Bioactive Silk Protein Biomaterial Systems for Optical Devices. *Biomacromolecules* **2008**, *9* (4), 1214-1220.
116. Parker, S. T.; Domachuk, P.; Amsden, J.; Bressner, J.; Lewis, J. A.; Kaplan, D. L.; Omenetto, F. G., Biocompatible Silk Printed Optical Waveguides. *Advanced Materials* **2009**, *21* (23), 2411-2415.
117. Wang, C.-H.; Hsieh, C.-Y.; Hwang, J.-C., Flexible Organic Thin-Film Transistors with Silk Fibroin as the Gate Dielectric. *Advanced Materials* **2011**, *23* (14), 1630-1634.
118. Ding, D.; Guerette, P. A.; Hoon, S.; Kong, K. W.; Cornvik, T.; Nilsson, M.; Kumar, A.; Lescar, J.; Miserez, A., Biomimetic Production of Silk-Like Recombinant Squid Sucker Ring Teeth Proteins. *Biomacromolecules* **2014**, *15* (9), 3278-3289.
119. Gupta, M. K.; Becknell, K. A.; Crosby, M. G.; Bedford, N. M.; Wright, J.; Dennis, P. B.; Naik, R. R., Programmable Mechanical Properties from a Worm Jaw-Derived Biopolymer through Hierarchical Ion Exposure. *ACS Applied Materials & Interfaces* **2018**, *10* (38), 31928-31937.
120. Ozbay, E., Plasmonics: Merging Photonics and Electronics at Nanoscale Dimensions. *Science* **2006**, *311* (5758), 189-193.
121. Hwang, G. M.; Pang, L.; Mullen, E. H.; Fainman, Y., Plasmonic sensing of biological analytes through nanoholes. *IEEE sensors journal* **2008**, *8* (12), 2074-2079.
122. Zeng, S.; Sreekanth, K. V.; Shang, J.; Yu, T.; Chen, C.-K.; Yin, F.; Baillargeat, D.; Coquet, P.; Ho, H.-P.; Kabashin, A. V.; Yong, K.-T., Graphene-Gold Metasurface Architectures for Ultrasensitive Plasmonic Biosensing. *Advanced Materials* **2015**, *27* (40), 6163-6169.
123. Hu, J.; Wang, D.; Bhowmik, D.; Liu, T.; Deng, S.; Knudson, M. P.; Ao, X.; Odom, T. W., Lattice-Resonance Metalenses for Fully Reconfigurable Imaging. *ACS Nano* **2019**, *13* (4), 4613-4620.
124. Wang, D.; Yang, A.; Hryn, A. J.; Schatz, G. C.; Odom, T. W., Superlattice Plasmons in Hierarchical Au Nanoparticle Arrays. *ACS Photonics* **2015**, *2* (12), 1789-1794.
125. Wang, D.; Bourgeois, M. R.; Guan, J.; Fumani, A. K.; Schatz, G. C.; Odom, T. W., Lasing from Finite Plasmonic Nanoparticle Lattices. *ACS Photonics* **2020**, *7* (3), 630-636.
126. Schokker, A. H.; Koenderink, A. F., Statistics of Randomized Plasmonic Lattice Lasers. *ACS Photonics* **2015**, *2* (9), 1289-1297.
127. Schokker, A. H.; Koenderink, A. F., Lasing in quasi-periodic and aperiodic plasmon lattices. *Optica* **2016**, *3* (7), 686-693.
128. Avayu, O.; Almeida, E.; Prior, Y.; Ellenbogen, T., Composite functional metasurfaces for multispectral achromatic optics. *Nature Communications* **2017**, *8* (1), 14992.
129. Bowden, N.; Brittain, S.; Evans, A. G.; Hutchinson, J. W.; Whitesides, G. M., Spontaneous formation of ordered structures in thin films of metals supported on an elastomeric polymer. *Nature* **1998**, *393* (6681), 146-149.

130. Lee, W.-K.; Yu, S.; Engel, C. J.; Reese, T.; Rhee, D.; Chen, W.; Odom, T. W., Concurrent design of quasi-random photonic nanostructures. *Proceedings of the National Academy of Sciences* **2017**, 201704711.
131. Gramotnev, D. K.; Bozhevolnyi, S. I., Plasmonics beyond the diffraction limit. *Nature Photonics* **2010**, *4* (2), 83-91.
132. Mubeen, S.; Hernandez-Sosa, G.; Moses, D.; Lee, J.; Moskovits, M., Plasmonic Photosensitization of a Wide Band Gap Semiconductor: Converting Plasmons to Charge Carriers. *Nano Letters* **2011**, *11* (12), 5548-5552.
133. Mascaretti, L.; Dutta, A.; Kment, Š.; Shalaev, V. M.; Boltasseva, A.; Zbořil, R.; Naldoni, A., Plasmon-Enhanced Photoelectrochemical Water Splitting for Efficient Renewable Energy Storage. *Advanced Materials* **0** (0), 1805513.
134. Wilcox, W. R.; LaChapelle, T. J., Mechanism of Gold Diffusion into Silicon. *Journal of Applied Physics* **1964**, *35* (1), 240-246.
135. Rollert, F.; Stolwijk, N. A.; Mehrer, H., Solubility, diffusion and thermodynamic properties of silver in silicon. *Journal of Physics D: Applied Physics* **1987**, *20* (9), 1148-1155.
136. Babicheva, V. E.; Kinsey, N.; Naik, G. V.; Ferrera, M.; Lavrinenko, A. V.; Shalaev, V. M.; Boltasseva, A., Towards CMOS-compatible nanophotonics: Ultra-compact modulators using alternative plasmonic materials. *Opt. Express* **2013**, *21* (22), 27326-27337.
137. Naik, G. V.; Boltasseva, A., Semiconductors for plasmonics and metamaterials. **2010**, *4* (10), 295-297.
138. Toth, L., Transition Metal Carbides and Nitrides (Academic Press, New York, 1971).
139. Gui, L.; Bagheri, S.; Strohfeldt, N.; Hentschel, M.; Zgrabik, C. M.; Metzger, B.; Linnenbank, H.; Hu, E. L.; Giessen, H., Nonlinear Refractory Plasmonics with Titanium Nitride Nanoantennas. *Nano Lett* **2016**, *16* (9), 5708-13.
140. Sato, R.; Ishii, S.; Nagao, T.; Naito, M.; Takeda, Y., Broadband Plasmon Resonance Enhanced Third-Order Optical Nonlinearity in Refractory Titanium Nitride Nanostructures. *ACS Photonics* **2018**.
141. Heather, G.; Jennifer, R.; Manuel, F.; Clayton, D.; Alexei, L.; Augustine, U.; Theodore, B. N.; Vladimir, M. S.; Alexandra, B.; Nathaniel, K., Nonlinearities and carrier dynamics in refractory plasmonic TiN thin films. *Opt. Mater. Express* **2019**, *9* (10), 3911--3924.
142. Diroll, B. T.; Saha, S.; Shalaev, V. M.; Boltasseva, A.; Schaller, R. D., Broadband Ultrafast Dynamics of Refractory Metals: TiN and ZrN. *Advanced Optical Materials* **2020**, *8* (19), 2000652.
143. Zakomirnyi, V. I.; Rasskazov, I. L.; Gerasimov, V. S.; Ershov, A. E.; Polyutov, S. P.; Karpov, S. V., Refractory titanium nitride two-dimensional structures with extremely narrow surface lattice resonances at telecommunication wavelengths. *Applied Physics Letters* **2017**, *111* (12), 123107.
144. Hohenau, A.; Krenn, J. R.; Beermann, J.; Bozhevolnyi, S. I.; Rodrigo, S. G.; Martin-Moreno, L.; Garcia-Vidal, F., Spectroscopy and nonlinear microscopy of Au nanoparticle arrays: Experiment and theory. *Physical Review B* **2006**, *73* (15), 155404.
145. Hoang, T. B.; Akselrod, G. M.; Yang, A.; Odom, T. W.; Mikkelsen, M. H., Millimeter-Scale Spatial Coherence from a Plasmon Laser. *Nano Letters* **2017**.
146. Smith, H. A.; Elhamri, S.; Eyink, K. G.; Grazulis, L.; Hill, M. J.; Back, T. C.; Urbas, A. M.; Howe, B. M.; Reed, A. N., Epitaxial titanium nitride on sapphire: Effects of substrate

- temperature on microstructure and optical properties. *Journal of Vacuum Science & Technology A* **2018**, *36* (3), 03E107.
147. Williams, K. R.; Gupta, K.; Wasilik, M., Etch rates for micromachining processing-part II. *Journal of Microelectromechanical Systems* **2003**, *12* (6), 761-778.
148. Hu, J.; Ren, X.; Reed, A. N.; Reese, T.; Rhee, D.; Howe, B.; Lauhon, L. J.; Urbas, A. M.; Odom, T. W., Evolutionary Design and Prototyping of Single Crystalline Titanium Nitride Lattice Optics. *ACS Photonics* **2017**, *4* (3), 606-612.
149. Briggs, J. A.; Naik, G. V.; Petach, T. A.; Baum, B. K.; Goldhaber-Gordon, D.; Dionne, J. A., Fully CMOS-compatible titanium nitride nanoantennas. *Applied Physics Letters* **2016**, *108* (5), 051110.
150. Alvarez, M. M.; Khoury, J. T.; Schaaff, T. G.; Shafigullin, M. N.; Vezmar, I.; Whetten, R. L., Optical Absorption Spectra of Nanocrystal Gold Molecules. *The Journal of Physical Chemistry B* **1997**, *101* (19), 3706-3712.
151. Laskar, J. M.; Shravan Kumar, P.; Herminghaus, S.; Daniels, K. E.; Schröter, M., High refractive index immersion liquid for superresolution 3D imaging using sapphire-based aplanatic numerical aperture increasing lens optics. *Appl. Opt.* **2016**, *55* (12), 3165-3169.
152. Ahmadi, T. S.; Logunov, S. L.; El-Sayed, M. A., Picosecond Dynamics of Colloidal Gold Nanoparticles. *The Journal of Physical Chemistry* **1996**, *100* (20), 8053-8056.
153. Sudeep, P. K.; Kamat, P. V., Photosensitized Growth of Silver Nanoparticles under Visible Light Irradiation: A Mechanistic Investigation. *Chemistry of Materials* **2005**, *17* (22), 5404-5410.
154. Kovalenko, S. A.; Eilers-König, N.; Senyushkina, T. A.; Ernsting, N. P., Charge Transfer and Solvation of Betaine-30 in Polar Solvents A Femtosecond Broadband Transient Absorption Study. *The Journal of Physical Chemistry A* **2001**, *105* (20), 4834-4843.
155. Zhou, M.; Vdović, S.; Long, S.; Zhu, M.; Yan, L.; Wang, Y.; Niu, Y.; Wang, X.; Guo, Q.; Jin, R.; Xia, A., Intramolecular Charge Transfer and Solvation Dynamics of Thiolate-Protected Au₂₀(SR)₁₆ Clusters Studied by Ultrafast Measurement. *The Journal of Physical Chemistry A* **2013**, *117* (40), 10294-10303.
156. Zhang, X.-X.; Liang, M.; Ernsting, N. P.; Maroncelli, M., Complete Solvation Response of Coumarin 153 in Ionic Liquids. *The Journal of Physical Chemistry B* **2013**, *117* (16), 4291-4304.
157. Patsalas, P.; Kalfagiannis, N.; Kassavetis, S., Optical Properties and Plasmonic Performance of Titanium Nitride. *Materials* **2015**, *8* (12), 3128-3154.
158. Poddubny, A.; Iorsh, I.; Belov, P.; Kivshar, Y., Hyperbolic metamaterials. *Nature Photonics* **2013**, *7* (12), 948-957.
159. Naik, G. V.; Saha, B.; Liu, J.; Saber, S. M.; Stach, E. A.; Irudayaraj, J. M.; Sands, T. D.; Shalaev, V. M.; Boltasseva, A., Epitaxial superlattices with titanium nitride as a plasmonic component for optical hyperbolic metamaterials. *Proc Natl Acad Sci U S A* **2014**, *111* (21), 7546-51.
160. Ferrari, L.; Wu, C.; Lepage, D.; Zhang, X.; Liu, Z., Hyperbolic metamaterials and their applications. *Progress in Quantum Electronics* **2015**, *40*, 1-40.
161. Vispute, R. D.; Wu, H.; Narayan, J., High quality epitaxial aluminum nitride layers on sapphire by pulsed laser deposition. *Applied Physics Letters* **1995**, *67* (11), 1549-1551.
162. Xiong, C.; Pernice, W. H. P.; Tang, H. X., Low-Loss, Silicon Integrated, Aluminum Nitride Photonic Circuits and Their Use for Electro-Optic Signal Processing. *Nano Letters* **2012**, *12* (7), 3562-3568.

163. Madan, A.; Kim, I. W.; Cheng, S. C.; Yashar, P.; Dravid, V. P.; Barnett, S. A., Stabilization of Cubic AlN in Epitaxial AlN/TiN Superlattices. *Physical Review Letters* **1997**, *78* (9), 1743-1746.
164. Yang, J.; Si, C.; Han, G.; Zhang, M.; Ma, L.; Zhao, Y.; Ning, J., Researching the Aluminum Nitride Etching Process for Application in MEMS Resonators. *Micromachines* **2015**, *6* (2), 281-290.
165. Kulkarni, N. S.; DeHoff, R. T., Application of Volatility Diagrams for Low Temperature, Dry Etching, and Planarization of Copper. *Journal of The Electrochemical Society* **2002**, *149* (11), G620.
166. Veszelei, M.; Andersson, K.; Ribbing, C. G.; Järrendahl, K.; Arwin, H., Optical constants and Drude analysis of sputtered zirconium nitride films. *Appl. Opt.* **1994**, *33* (10), 1993-2001.
167. Dutta, A.; Kinsey, N.; Saha, S.; Guler, U.; Shalaev, V. M.; Boltasseva, A. In *Plasmonic interconnects using zirconium nitride*, 2016 Conference on Lasers and Electro-Optics (CLEO), 5-10 June 2016; 2016; pp 1-2.
168. Sadat-Shojai, M.; Khorasani, M.-T.; Jamshidi, A., 3-Dimensional cell-laden nano-hydroxyapatite/protein hydrogels for bone regeneration applications. *Materials Science and Engineering: C* **2015**, *49*, 835-843.
169. Ding, D.; Pan, J.; Lim, S. H.; Amini, S.; Kang, L.; Miserez, A., Squid suckerin microneedle arrays for tunable drug release. *Journal of Materials Chemistry B* **2017**, *5* (43), 8467-8478.
170. Kurland, N. E.; Dey, T.; Wang, C.; Kundu, S. C.; Yadavalli, V. K., Silk Protein Lithography as a Route to Fabricate Sericin Microarchitectures. *Advanced Materials* **2014**, *26* (26), 4431-4437.
171. Kim, S.; Marelli, B.; Brenckle, M. A.; Mitropoulos, A. N.; Gil, E.-S.; Tsioris, K.; Tao, H.; Kaplan, D. L.; Omenetto, F. G., All-water-based electron-beam lithography using silk as a resist. *Nature Nanotechnology* **2014**, *9* (4), 306-310.
172. Dickerson, M. B.; Dennis, P. B.; Tondiglia, V. P.; Nadeau, L. J.; Singh, K. M.; Drummy, L. F.; Partlow, B. P.; Brown, D. P.; Omenetto, F. G.; Kaplan, D. L.; Naik, R. R., 3D Printing of Regenerated Silk Fibroin and Antibody-Containing Microstructures via Multiphoton Lithography. *ACS Biomaterials Science & Engineering* **2017**, *3* (9), 2064-2075.
173. Cantaert, B.; Ding, D.; Rieu, C.; Petrone, L.; Hoon, S.; Kock, K. H.; Miserez, A., Stable Formation of Gold Nanoparticles onto Redox-Active Solid Biosubstrates Made of Squid Suckerin Proteins. *Macromolecular Rapid Communications* **2015**, *36* (21), 1877-1883.
174. Hershewe, J. M.; Wiseman, W. D.; Kath, J. E.; Buck, C. C.; Gupta, M. K.; Dennis, P. B.; Naik, R. R.; Jewett, M. C., Characterizing and Controlling Nanoscale Self-Assembly of Suckerin-12. *ACS Synthetic Biology* **2020**, *9* (12), 3388-3399.
175. Chou, C.-C.; Martin-Martinez, F. J.; Qin, Z.; Dennis, P. B.; Gupta, M. K.; Naik, R. R.; Buehler, M. J., Ion Effect and Metal-Coordinated Cross-Linking for Multiscale Design of Nereis Jaw Inspired Mechanomutable Materials. *ACS Nano* **2017**, *11* (2), 1858-1868.
176. Knudson, M. P.; Hryn, A. J.; Huntington, M. D.; Odom, T. W., Sequential Feature-Density Doubling for Ultraviolet Plasmonics. *ACS Applied Materials & Interfaces* **2017**, *9* (39), 33554-33558.
177. Partlow, B. P.; Hanna, C. W.; Rnjak-Kovacina, J.; Moreau, J. E.; Applegate, M. B.; Burke, K. A.; Marelli, B.; Mitropoulos, A. N.; Omenetto, F. G.; Kaplan, D. L., Highly tunable elastomeric silk biomaterials. *Advanced functional materials* **2014**, *24* (29), 4615-4624.

178. Duan, H.; Winston, D.; Yang, J. K. W.; Cord, B. M.; Manfrinato, V. R.; Berggren, K. K., Sub-10-nm half-pitch electron-beam lithography by using poly(methyl methacrylate) as a negative resist. *Journal of Vacuum Science & Technology B* **2010**, 28 (6), C6C58-C6C62.
179. Huntington, M. D.; Lauhon, L. J.; Odom, T. W., Subwavelength Lattice Optics by Evolutionary Design. *Nano Letters* **2014**, 14 (12), 7195-7200.

CURRICULUM VITAE

EDUCATION

Ph.D. in Materials Science & Engineering **September 2015 – March 2021**

McCormick School of Engineering, Northwestern University, Evanston, Illinois

Overall GPA: 3.59

Management Certificate for Scientists and Engineers **Summer 2020**

Kellogg School of Management, Northwestern University, Evanston, Illinois

B.S. in Nanoscale Science **May 2015**

College of Nanoscale Science and Engineering, State University of New York, Albany, New York

Summa Cum Laude, Overall GPA: 3.86

Honors Thesis: "Process Development and Electrical Characterization of SiCOH ReRAM Elements"

SKILLS

Software	MATLAB, Python, Adobe Illustrator, Photoshop, Final Cut Pro, Blender, iMovie, Microsoft Office
Techniques	Photo, nanoimprint and electron beam lithography, ion-beam milling, energy-dispersive x-ray spectroscopy, pump-probe femto-second laser measurements, thin film deposition
Instruments	Scanning electron and atomic force microscope, transient absorption spectrometer, UV-VIS spectrometer, reactive ion etchers

RESEARCH EXPERIENCE

Department of Materials Science and Engineering – Northwestern University

Research Assistant – Advised by Prof. Teri Odom *November 2015 – Present*

- Studied static and ultrafast dynamics of titanium nitride plasmonic nanostructures via nanofabrication, optical measurements, and computer simulations in collaboration with Air Force Research Lab (AFRL) and Argonne National Lab researchers
- Presented monthly updates, quarterly reports and annual summaries for AFRL Center of Excellence for Advanced Bioprogrammable Nanomaterials grant, resulting in four annual renewals
- Led team of 5 postdocs and graduate students from applied physics, materials science and chemistry to submit a grant proposal on nanofabrication of photonic moiré nanostructures, resulting in a \$400,000.00 project in the NSF Advanced Manufacturing directorate
- Maintained and repaired thermal evaporator, vacuum pumps, and connection to Northwestern supercomputer and trained over 20 researchers on the use of these tools and techniques
- Served as a visiting scholar to Wright-Patterson Air Force Base (seven weeks total) to collaborate with researchers at the AFRL in Biological Soft Matter, Nanoelectronics, Nanophotonics and Sensors divisions

- Collaborated with a Mechanical Engineering student as part of the Predictive Science and Engineering Design Fellowship to use a homebuilt genetic algorithm for high-throughput screening of stretchable metasurfaces and develop a process flow to fabricate optimized structures
- Developed process to fabricate multi-metallic nanostructures that support multi-wavelength lasing
- Initiated formation of modeling subgroup and led students and post-docs in weekly research discussions

College of Nanoscale Science and Engineering – University at Albany

Undergraduate Research Assistant – Advised by Prof. Nathaniel Cady *May 2014 – May 2015*

- Developed a process flow using ultra low-k dielectric (SiCOH) as the insulator in resistive memory devices
- Performed electrical testing on devices to determine forming voltage, set/reset voltages, ratio between high resistance state/low resistance state and endurance

Undergraduate Research Assistant – Advised by Prof. Richard Matyi *May – December 2013*

- Studied the change in microstructure and fractional occupancy of In and Ga in photovoltaic thin films across thermal deposition steps by using Rietveld refinement packages on collected XRD data

Research Assistant Intern – Diamon Fusion International *June – August 2010*

- Planned and executed a project using the photocatalytic antimicrobial characteristics of titanium dioxide

PUBLICATIONS

- **T. Reese**, A.N. Reed, A. Sample, F.F. Fernandez, R. Schaller, A.M. Urbas, T.W. Odom. *Submitted to ACS Photonics*. “Ultrafast Spectroscopy of Plasmonic Titanium Nitride Nanoparticle Lattices”
- **T. Reese**, D. Rhee, J. Gun, R. Li, T.W. Odom. *In Preparation*. “Multi-Color Lattice Plasmons from Multi-Material Arrays”
- **T. Reese**, K. Singh, C. Buck, P.A. Dennis, T.W. Odom. *In Preparation*. “Scalable Fabrication of Protein Hydrogel Nanostructures”
- J. Hu, T. Liu, P. Choo, S. Wang, **T. Reese**, A. Sample and T.W. Odom, *ACS Cent. Sci.* 6, 12, 2339-2346 (2020). “Single-Nanoparticle Orientation Sensing by Deep Learning”
- W-K. Lee, S. Yu, C.J. Engel, **T. Reese**, D. Rhee, W. Chen, and T.W. Odom, *Proc. Natl. Acad. Sci. U.S.A.* 114, 8734-8739 (2017). “Concurrent design of quasi-random photonic nanostructures”
- J. Hu, X. Ren, A.N. Reed, **T. Reese**, D. Rhee, B. Howe, L.J. Lauhon, A.M. Urbas, and T.W. Odom, *ACS Photonics* 4, 606-612 (2017). “Evolutionary Design and Prototyping of Single Crystalline Titanium Nitride Lattice Optics”
- **T. Reese**, S.B. Schujman and R.J. Matyi, *Proc. 40th IEEE Photovoltaic Specialist Conference*, 1691 (2014). “Structure Evolution in CIGS Deposition: An X-ray Diffraction Analysis with Rietveld Whole-Pattern Refinement”

PRESENTATIONS

- Air Force Research Lab Center of Excellence for Advanced Bioprogrammable Nanomaterials Annual Meeting 2020 – “Fabrication and Characterization of Metasurfaces Based on Unconventional Optical Materials”.

- Air Force Research Lab Center of Excellence for Advanced Bioprogrammable Nanomaterials Annual Meeting 2019 – “Evolutionary Design of Metasurfaces Based on Unconventional Optical Materials”.
- Air Force Research Lab, Wright-Patterson Air Force Base Site Visit – “CMOS Compatible Metasurfaces by Evolutionary Design”. January 8th, 2018
- Air Force Research Lab Center of Excellence for Advanced Bioprogrammable Nanomaterials Annual Meeting 2018 – “Evolutionary Design of Metasurfaces Based on Unconventional Optical Materials”.

AWARDS

<i>Predictive Science & Engineering Design Cluster Fellow</i>	September 2016 – June 2017
<i>Annual CNSE Scholarship</i>	September 2012 – May 2015
<i>Newport Corporation Rising Stars Scholarship</i>	September 2011 – May 2012

TEACHING EXPERIENCE

Graduate Teaching Assistant, MSE 201: Introduction to Materials **Spring 2019 & 2020**

- Led weekly recitations for 25 students, hosted weekly office hours, developed course homework questions, and worked with other TAs to standardize grading

Mentor to NSF Research Experience for Undergraduates **Summer 2016 & 2017**

- Planned projects and trained two undergraduate summer interns on plasmonic materials, nanofabrication and electromagnetic simulations
- Guided students in writing professional research updates and developing their final project presentations
- One of the students was selected to present her results at National Diversity in STEM conference in Fall 2016

COMMUNITY OUTREACH

Women Supporting Women in the Sciences (WS2) **Spring – Summer 2019**

- Developed presentation and workbook in collaboration with 5-person team for “Organizing to Support Women in STEM” workshop
- Communicated workshop content to graduate student partners in Tanzania

Letters to a Pre-Scientist Science Outreach Program **Fall 2016 – Spring 2017**

- Wrote monthly letters to encourage and mentor a 5th grade pen pal interested in science

Science Outreach Presentation to Local High School Students **Fall 2016**

- Prepared and presented a talk on nanotechnology research at Lane Tech High School in Chicago

LEADERSHIP

Modeling Subgroup Leader (Odom Research Group) **February 2018 – February 2020**

- Initiated formation of modeling subgroup and became inaugural leader
- Organized speakers and summarized discussions for research advisor

Instrument Manager (Odom Research Group)**February 2016 – Present**

- Maintained and repaired thermal evaporator, vacuum pumps, and connection to Northwestern supercomputer
- Trained more than 20 researchers on use of tools

Materials Science Student Association Board Member**July 2016 – July 2017**

- Initiated inaugural annual Materials Science & Engineering Department 5K, resulting in \$500 donation in its first year to the Pederson McCormick Boys and Girls Club and a total of \$4800 in subsequent years
 - Led committee of three students to organize and manage race of 90+ participants, including recruiting local sponsors, purchasing race materials, and mapping the course
 - Recruited and managed 10+ volunteers to coordinate race activities
 - Helped organize large-scale professional development events for materials science department, including recruitment weekends and orientation week
-